

THESIS FOR THE DEGREE OF DOCTOR OF PHILOSOPHY

Graphene plasmons in nanostructured environments

Tobias Wenger

Applied Quantum Physics Laboratory
Department of Microtechnology and Nanoscience
Chalmers University of Technology
Göteborg, Sweden, 2017

Graphene plasmons in nanostructured environments
Tobias Wenger
Göteborg, 2017
ISBN 978-91-7597-641-9

Copyright © Tobias Wenger, 2017

Doktorsavhandlingar vid Chalmers tekniska högskola
Ny serie Nr 4322
ISSN 0346-718X

ISSN 1652-0769 Technical Report MC2-370
Applied Quantum Physics Laboratory
Department of Microtechnology and Nanoscience - MC2
Chalmers University of Technology
SE-412 96 Göteborg, Sweden
Telephone: +46 (0)31-772 1000

Cover: A graphene sheet on top of a subwavelength dielectric grating with an artistic expression of graphene plasmon oscillations. The arrows represent electromagnetic radiation used to probe the plasmons.

Printed by Chalmers Reproservice
Göteborg, Sweden, 2017

Graphene plasmons in nanostructured environments

TOBIAS WENGER

Applied Quantum Physics Laboratory

Department of Microtechnology and Nanoscience

Chalmers University of Technology

Abstract

This thesis explores the combination of electromagnetism with electrons in graphene. Graphene is a one atom thick layer of carbon atoms which contains electrons that exhibit rather special properties in terms of their conduction abilities. The combination of electromagnetism with electrons gives rise to new solutions to the governing equations — solutions with characteristics not quite like normal electromagnetic radiation and not quite like electrons. These solutions, which also exist in normal conductors, are hybrids between electromagnetism and matter, and are usually referred to as plasmons. This thesis is a theoretical study of plasmons in graphene.

Graphene plasmons are investigated by calculating the conductivity of graphene, starting from a Hamiltonian describing the low-energy graphene electrons. The conductivity is calculated using linear response theory in terms of Green's functions. In order to probe graphene plasmons with electromagnetic radiation, we consider a subwavelength dielectric grating as a coupling structure. We develop the necessary theory to calculate electromagnetic scattering from the combined system of graphene and grating. The techniques considered are a scattering matrix method and a finite element method. Both are applied to compute the scattering coefficients, which contain information about the graphene plasmons and are also obtainable in experiments. We use these techniques to study various aspects of graphene plasmons, such as their nonlocal properties and the effects of impurities. In addition, we examine the response of graphene plasmons to changes in the surrounding environment and apply this for sensing purposes. Finally, we show that graphene plasmons can be controlled using a DC current in the graphene sample.

Keywords: Graphene plasmons, nonlocal response, linear response Green's functions, subwavelength electromagnetic scattering

List of publications

This thesis is based on the work contained in the following publications, appended in the end of the thesis:

- I. **Optical signatures of nonlocal plasmons in graphene**
Tobias Wenger, Giovanni Viola, Mikael Fogelström, Philippe Tassin, and Jari Kinaret
Physical Review B **94**, 205419 (2016)
- II. **High-sensitivity plasmonic refractive index sensing using graphene**
Tobias Wenger, Giovanni Viola, Jari Kinaret, Mikael Fogelström, and Philippe Tassin
2D Materials **4**, 025103 (2017)
- III. **Graphene plasmons in the presence of adatoms**
Giovanni Viola, Tobias Wenger, Jari Kinaret, and Mikael Fogelström
New Journal of Physics **19**, 073027 (2017)
- IV. **Graphene plasmons: impurities and nonlocal effects**
Giovanni Viola, Tobias Wenger, Jari Kinaret, and Mikael Fogelström
Manuscript to be submitted
- V. **Current-controlled light scattering and asymmetric plasmon propagation in graphene**
Tobias Wenger, Giovanni Viola, Jari Kinaret, Mikael Fogelström, and Philippe Tassin
arXiv:1710.00338 (2017)
Manuscript submitted to Physical Review B

Specification of my contributions to the appended publications

- I. The idea for this publication was developed during discussions among all authors. I performed the calculations and wrote the manuscript with comments from my co-authors.
- II. I developed the idea, did the calculations, and wrote the manuscript. Input from my co-authors was continuous during this process.
- III. I participated in the discussions and conception of the project as well as in the analysis of the results. I performed the calculations for the plasmon dispersions and co-authored the manuscript.
- IV. For this project, I helped formulate the project and how to investigate the plasmons. I also participated in the analysis of the results and helped in the writing of the manuscript.
- V. I developed the main idea and performed the calculations. I then analyzed the results together with my co-authors. I wrote the manuscript with comments from my co-authors.

Acknowledgments

First, I want to take this opportunity to thank Mikael Fogelström and Jari Kinaret for taking me in as a PhD student all those years ago. They managed to guide and tutor me over the years and I would like to think I know a great deal more than I used to. Thank you for this interesting time. I would also like to thank Philippe Tassin for his valuable supervision, guidance, and in-depth discussions.

My deepest gratitude to Giovanni Viola who always had time to discuss and share his vast knowledge of physics and related issues. The discussions we had were always engaging, interesting, and always took longer than we intended. Also, I thank Giovanni for his moral support in times when my spirit was low.

I feel also the need to thank the group in which this thesis work has been done, Applied Quantum Physics (AQP) at MC2, Chalmers. This naturally includes all members, past and present, that I have interacted with over the years. The coffee breaks and discussions about everything from physics to international tax law is perhaps the thing that I will miss the most.

I also wish to extend my thanks to all my friends for understanding me not being able to join so many activities lately. Also, thanks for all the times we have done something besides work that has allowed me to think about something else once in a while.

A special thanks to my family for being supportive of this whole endeavor and for understanding my less frequent calls and increased absent-mindedness these last months.

Sofia, thank you for your continuous support and encouragement.

Tobias Wenger
Göteborg, October, 2017

To all my teachers.

Contents

1	Introduction	1
1.1	Plasmonics	2
1.2	Graphene plasmonics	3
1.3	Scope of the thesis - limitations	5
1.4	Thesis outline	6
2	Graphene	7
2.1	Electron band structure of graphene	7
2.1.1	Electron distribution and gating	12
2.2	Graphene production methods — different types of graphene	14
2.3	Impurities and scattering in graphene	16
3	Green's Functions and Linear Response Theory	19
3.1	Green's functions	19
3.1.1	Mathematical definition	20
3.1.2	Equilibrium Green's function for graphene	21
3.1.3	Non-equilibrium Green's function formalism	22
3.2	Linear response in Keldysh formalism	27
3.3	Graphene conductivity in the clean limit	31
3.4	Mermin relaxation time approximation	33
3.5	Green's function self energy	35
3.5.1	Adatoms coupled to graphene	37
3.5.2	Dilute distribution of impurity sites — a self-consistent treatment	38
4	The Maxwell Equations	41

4.1	The Maxwell equations and light propagation	41
4.1.1	Nonlocal electromagnetic properties	43
4.1.2	Electromagnetic energy and propagation	45
4.2	Electromagnetic scattering from a conducting interface . .	47
4.3	Solution methods for complex light scattering problems . .	48
4.3.1	Scattering matrix method	50
4.3.2	Finite element method	53
5	Graphene Plasmons	61
5.1	Graphene plasmon dispersion relation	61
5.2	Graphene plasmon propagation and damping	64
5.3	Coupling electromagnetic radiation to graphene plasmons	68
5.4	Refractive index sensing using graphene plasmons	69
5.4.1	Figures of merit for refractive index sensing	69
5.5	Comparison between graphene plasmons and plasmons in metals	71
5.5.1	Metal-dielectric interface plasmons	71
5.5.2	Localized surface plasmons in metal nanoparticles .	74
5.5.3	Summary of graphene versus metals for plasmonics	76
6	Overview of Appended Publications	77
6.1	Paper I	77
6.2	Paper II	78
6.3	Paper III	78
6.4	Paper IV	79
6.5	Paper V	79
7	Summary	81
	Appendix A Graphene Hamiltonian and Electron Bands	85
	Appendix B Graphene Green's Function	87
	Appendix C S-matrix Method Calculation	89

Appendix D Rayleigh-Ritz Variational Method for the Poisson Equation	91
Appendix E Longitudinal (TM) Plasmon Dispersion Equation for Conducting Sheets	93
E.1 Longitudinal plasmon dispersion equation	93
E.2 Non-retarded limit and expansion in small plasmon losses	95

Chapter 1

Introduction

This is a thesis about plasmons in graphene. Plasmons are collective charge oscillations with an associated electromagnetic field that can occur in conductors [1]. Most of this thesis is focused on specific details of graphene plasmons, but to understand why graphene plasmons are of interest, it is interesting to first consider the larger perspective.

Electromagnetic radiation plays very important roles in all our lives; it provides energy from the sun, without which life on earth would be difficult at best, and it lets us see our surroundings. Visible light is nothing but a small part of the electromagnetic spectrum, with ultraviolet radiation and X rays being the same type of radiation but higher in frequency, and infrared radiation lower in frequency. Indeed, many more parts of the spectrum can be named but we refrain from listing them all. Suffice it to say that this plethora of different frequencies of electromagnetic radiation have numerous technological applications that affect our daily lives. The radio, X-ray imaging, lasers, screens of different kinds, and microwave ovens are all examples of technologies that rely on generating and receiving electromagnetic radiation. In particular, data transmission is one area where electromagnetic radiation has had a large impact. It allows us to send vast amounts of data in a wireless manner or over optical fibers to connect our computers. It also allows us to communicate with each other here on earth via radio and cell phones as well as to communicate with satellites, rovers, and astronauts far out in space.

Electromagnetic radiation is a good way to transmit information; it moves as fast as possible - with the speed of light. In addition, since electromagnetic radiation comes in different frequencies, it is possible to employ various clever data encoding schemes to transmit a lot of data in short amounts of time. Another important aspect of electromagnetic radiation is that we can use it to gather information about our environment, i.e., we can use electromagnetic radiation as a window into nature and

use it to study various phenomena. This ranges from the very large scale where we can detect radiation from distant quasars [2] to the very small scale where we can use visible light to image details down to 100 nm in size [3]. Thus we conclude that electromagnetic radiation is important, both scientifically and technologically, and new ways of controlling, generating, and detecting electromagnetic radiation is of significant interest for future applications.

When it comes to processing of information, electrons are favored over radiation. One of the most important inventions of the 20th century, the transistor, enables electronic computers to function the way they do. This has enabled electronic computers to completely permeate our civilization. Since plasmons are hybrid excitations, they have properties that are similar to both electromagnetic radiation and electrons. Perhaps it is possible to use this duality to extract the “best” properties from both worlds [4, 5].

1.1 Plasmonics

The study of electrons is called electronics; similarly, the field that studies plasmons is called plasmonics. The roots of the field of plasmonics can be traced back to the beginning of the 20th century. However, examples of the use of what is now known as plasmonic effects can actually be traced back much further than that. Well known examples are, for instance, the staining of church windows during medieval times and already the romans used plasmonic effects to color cups. However, these early uses of plasmonics were lacking in their understanding of the underlying physical effects. For such an understanding to be possible, a theory of electromagnetism was needed.

The unification of electricity and magnetism was made by Maxwell in 1865 [6], paving the road for investigation of electromagnetism in a wide range of settings. In 1902, Wood investigated the reflection properties of metallic gratings on a surface and observed unexplained features in their spectra [7], this is usually taken to be the first observation of plasmons in a scientific setting. Langmuir and Tonks experimented with gaseous plasmas in the 1920's and found waves in the plasma [8], these are now known as Langmuir waves. In 1956, Pines realized there was a connection between Langmuir waves and the electron energy losses in the materials he was investigating. He published his work on energy losses in materials due to excitation of collective oscillations which he called plasmons [9]. Ritchie was around the same time investigating electron energy losses in thin films and discovered that plasmons could exist on or near the material surface

and thus the notion of surface plasmons was born. In 1968, some 60 years after the experiment, Ritchie was able to explain the strange reflection behavior that Wood had found in terms of surface plasmons being excited at the gratings [10].

The fact that plasmons have a smaller wavelength than electromagnetic radiation at the same frequency, leads to localization of energy in the plasmon modes [11]. This causes large field enhancements which in turn leads to enhancement of interaction strengths, e.g., Raman enhancement [11, 12] and increased coupling to dipole emitters [13]. For instance, strong coupling to single molecules has been experimentally demonstrated at room temperature [14]. Furthermore, the ability to localize electromagnetic fields to scales that are subwavelength could enable miniaturized photonic circuits [5, 15], biosensors with high sensitivities [16, 17], as well as microscopy with subwavelength resolution [18].

However, the wave localization comes at a price. Large localization usually leads to large losses, meaning that plasmons become highly damped. A trade-off exists between large localization and long propagation lengths [1]. A common material with relatively small plasmon losses is silver; the surface plasmons can propagate up to 1 mm under the right conditions [15]. However, in this regime the plasmon wavelength is only a few percent smaller than the free-space wavelength [19].

1.2 Graphene plasmonics

Graphene plasmonics is a rather new field of research that merges the exciting properties of plasmons with those of graphene. The first theoretical investigations of graphene plasmons were performed in Refs. [20, 21], where the authors obtained the same $\omega \propto \sqrt{k}$ as normal 2DEG plasmons [22], but a scaling in density as $\omega \propto n^{1/4}$ instead of $\omega \propto \sqrt{n}$ as the 2DEG plasmons. The density dependence of the plasmon frequency in graphene (and 2DEG's) can be utilized to tune the plasmon frequency by changing the electron density. In graphene, the electron density can be tuned by using a back gate to which a voltage is applied, thus forcing charges in or out of the graphene sheet [23]. The tunability of the plasmon energy of graphene is one of the main advantages of using graphene as a plasmonic material instead of using a more conventional material such as silver. Another difference between graphene plasmons and plasmons in metals is the amount of wave localization provided.

The fact that plasmons exhibit wave localization means that the wave-

length at a specific frequency is smaller for the plasmon than for free-space light. This is a common feature for plasmons, not only graphene plasmons, but the mismatch is larger in graphene plasmons than for conventional plasmons due to the larger localization. On flat surfaces, this means that incident light does not couple to the plasmons [1]. There are several methods to overcome this mismatch and allow incident light to couple to the plasmons. Chapter 5 contains a more thorough treatment of this subject and here we simply note that this mismatch can be overcome and graphene plasmons, as well as metal plasmons, can be probed using electromagnetic radiation. However, this requires special coupling structures.

The early theory for graphene plasmons treated clean graphene at zero temperature [20, 21]. This is sufficient for some purposes, such as understanding the frequency-wavelength relationship at long wavelength. However, it is not sufficient for understanding the propagation distance of graphene plasmons. In the clean limit at zero temperature, the prediction is that graphene plasmons propagate infinitely far, something clearly not observed in experiments [24, 25]. These experiments show that the graphene plasmons experience a significant damping and to model this, extensions of the previously mentioned idealized case are necessary. Impurity scattering effects on graphene plasmons were investigated in Ref. [26] and they found that for the amount of scattering that was estimated from experiments, the graphene plasmons would still exhibit large localization but with substantial losses as a result. The losses are substantial, but when considering also that the localization factor is large, the amount of loss is small. A generalization to finite temperature response in graphene was calculated in Ref. [27] and was also treated in Ref. [28], where finite temperature effects on the plasmon dispersion and the plasmon damping were also considered.

In graphene, as it turns out, the wavelength of electrons at the Fermi energy, called the Fermi wavelength, can be rather large. It can be several tens of nanometers for realistically doped graphene samples. This is comparable to the plasmon wavelength for certain frequencies and, as a result, the wave nature of electrons can affect the wave nature of the plasmons. This is usually called nonlocal effects, see chapter 4 for more on this subject. Nonlocal effects can also be important in metals. However, the Fermi wavelength of metals is almost two orders of magnitude smaller than in graphene. In silver and gold for example, the Fermi wavelength is approximately 5 Å [29] and so, a very small plasmon wavelength - or nanopatterning of the metal - is needed to resolve this. Nonlocal effects have been shown to limit the field enhancement resulting from plasmonic effects in

various metallic structures that are patterned on length scales comparable to 5 Å. Examples are spherical nanoparticles [30], half-cylinder grooves [31], and conical nanotips [32]. Nonlocal effects can also cause blue-shifts of plasmon resonances [30, 31] when compared with the local theory (which neglects nonlocal effects). Nonlocality has also been discussed in the context of making strong coupling with small dipole emitters more difficult [33].

By now, graphene plasmons have emerged as a promising platform at terahertz to mid-infrared frequencies [34] for a wide range of applications [35]. For instance, graphene plasmons have been used to enhance photodetectors [36, 37], to perform label-free sensing of biomolecules [38, 39], and for modulation of infrared radiation [40]. Furthermore, in the near future, stacking of various 2D materials is expected to become an additional factor to consider in the context of optoelectronic devices [35].

1.3 Scope of the thesis - limitations

This is a thesis focused on theory and as such, we are interested in constructing models of reality that can be used to explain and understand phenomena around us. All models are imperfect, in that approximations are made and effects that are expected to be less important are not included in the model. This is neatly captured in a quote by the statistician George Box who wrote: *“Essentially, all models are wrong. But some are useful.”* [41] p. 424. The meaning being that all models contain imperfections, but that might well be sufficient to obtain substantial information and understanding of the system in question.

In this thesis we have neglected the effect of phonons. This is done in order to keep focus on nonlocal effects and other sources of plasmon damping. A more detailed discussion about this can be found in section 2.3. Furthermore, we have neglected electron-electron interactions which have been shown to renormalize the Fermi velocity for small doping levels [42]. We consider doping levels larger than where these effects are appreciable.

What is included in this thesis is a treatment of finite temperatures, nonlocal effects, as well as impurities in different approximations. We shall see that this allows us to obtain a model that captures essential features of graphene plasmons and lets us calculate observable properties that can be compared with experiments.

1.4 Thesis outline

The rest of the thesis is divided into four chapters as well as five appendices. Chapter 2 introduces graphene and treats a tight-binding Hamiltonian to describe electrons moving in the carbon lattice. The chapter also contains the approximation of low energies which gives rise to the concept of Dirac electrons. In chapter 3, Green's functions are introduced and utilized to formulate a linear response theory to calculate the graphene conductivity. This treatment is rather general and, in particular, the use of Keldysh Green's functions makes the formalism valid also for systems that are initially out of equilibrium. The chapter also contains a treatment of how to introduce additions to the bare graphene Hamiltonian and how this can be handled in the Green's function formalism by introducing the concept of self energies.

Chapter 4 treats Maxwell's equations, energy propagation, nonlocality in response functions, and electromagnetic scattering. Furthermore, this chapter deals with solution methods for electromagnetic scattering in nanostructured environments necessary to probe graphene plasmons. Chapter 5 is devoted to graphene plasmons and their dispersion relation, propagation, and damping as well as how to couple radiation to graphene plasmons. In addition, the chapter includes a section about refractive index sensing using graphene plasmons and ends with a comparison between typical properties of graphene plasmons and metal plasmons.

The appendices consist of calculations that were deemed to lengthy to be put in the main text, but at the same time valuable enough to include in the thesis. Appendix A contains a derivation of how to arrive to the momentum-space Hamiltonian from the real-space tight-binding Hamiltonian for graphene. Appendix B treats how to compute the bare graphene Green's function. Appendix C contains calculations for electromagnetic fields inside a grating region and D contains explicit calculations of a finite element method solution. Finally, appendix E is a derivation of the plasmon dispersion equation for thin conducting sheets.

Chapter 2

Graphene

In this chapter we calculate the band structure of graphene and, doing so, we explain the emergence of the so-called Dirac approximation that is used throughout the rest of the thesis. The Dirac approximation — as any approximation — has its limitations, but its greatest benefit is that it allows for analytic calculations to be carried out. The Dirac approximation is valid for low energies, which is the region of interest for graphene plasmonics, and thus it is sufficient for our purposes. In this chapter, we treat the basic electronic properties such as wave functions and electron dispersion, as well as electron distributions and doping level. We briefly discuss different graphene production methods and their benefits and drawbacks. The chapter ends with a treatment of impurities in graphene and the related concept of electron mobility — often used to quantify graphene sample quality.

2.1 Electron band structure of graphene

As mentioned in the introduction, graphene is a monolayer of carbon atoms arranged in what is usually called a honeycomb lattice or a hexagonal lattice, see Fig. 2.1. Carbon atoms have six electrons and two of these fill up the inner electronic orbital and stay inert, while four electrons reside in the outer orbital. Of these, three electrons hybridize and create bonds with the neighboring carbon atoms, called σ -bonds and the remaining electron occupies the so-called π -band. This band can hold two electrons per atom, and since there is only one electron per carbon atom, the result is a half filled π -band [43]. These π -electrons are the ones that are of importance for the electronic properties of graphene, but also the structure of the graphene lattice is important. There are two inequivalent atoms in the lattice structure of graphene, usually called the A and B atoms, and they build up the underlying triangular A and B lattices, see Fig. 2.1.

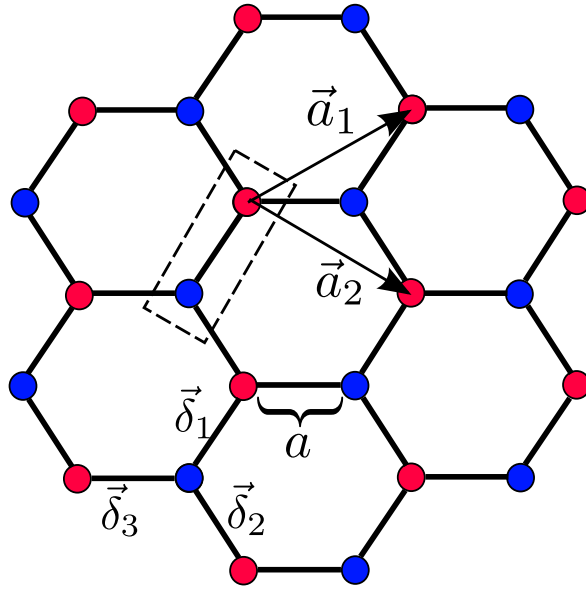


Figure 2.1: A small part of the honeycomb lattice of monolayer graphene showing an example of how to label the A (blue) and B (red) sublattice. The connections between neighboring atoms represent nearest neighbor electron hopping between the atoms. $a = 1.42 \text{ \AA}$ and the lattice vectors \vec{a}_1 and \vec{a}_2 are defined in Eqs. 2.1 and 2.2 while the vectors $\vec{\delta}_m$ connect nearest-neighbor atoms and are defined in Eqs. 2.3-2.5.

The lattice vectors, shown in Fig. 2.1, are

$$\vec{a}_1 = \frac{a\sqrt{3}}{2} (\sqrt{3}, 1), \quad (2.1)$$

$$\vec{a}_2 = \frac{a\sqrt{3}}{2} (\sqrt{3}, -1), \quad (2.2)$$

where $a = 1.42 \text{ \AA}$, and the length of \vec{a}_1 and \vec{a}_2 is $a\sqrt{3} \approx 2.46 \text{ \AA}$. The nearest-neighbor vectors, also shown in Fig. 2.1, are

$$\vec{\delta}_1 = \frac{a}{2} (1, \sqrt{3}), \quad (2.3)$$

$$\vec{\delta}_2 = \frac{a}{2} (1, -\sqrt{3}), \quad (2.4)$$

$$\vec{\delta}_3 = a(-1, 0). \quad (2.5)$$

A minimal model for the π -orbital electrons is given by the tight-binding Hamiltonian [43]

$$H = -t \sum_{\langle i,j \rangle, s} (a_{i,s}^\dagger b_{j,s} + h.c.), \quad (2.6)$$

where $\langle \dots \rangle$ denotes nearest-neighbor summation, $s = (\uparrow, \downarrow)$ is a sum over spins, and $t = 2.8 \text{ eV}$ is the nearest-neighbor hopping amplitude. In

Eq. (2.6), $a_{i,s}$ ($a_{i,s}^\dagger$) is the annihilation (creation) operator of electrons at site i and spin s on the A sublattice and $b_{i,s}$ and $b_{i,s}^\dagger$ are defined similarly for the B sublattice. We now write the operators as a Fourier transform

$$a_{i,s} = \frac{1}{\sqrt{N}} \sum_{\vec{k}} e^{-i\vec{k}\cdot\vec{R}_i} a_s(\vec{k}), \quad (2.7)$$

where N is the number of unit cells, \vec{R}_i is the position of site i , and the sum of \vec{k} is over the Brillouin zone. The Hamiltonian in Eq. 2.6 can then be written as

$$H = \sum_{\vec{k},s} = \begin{pmatrix} a_{\vec{k},s}^\dagger & b_{\vec{k},s}^\dagger \end{pmatrix} \begin{pmatrix} 0 & -t\phi_k \\ -t\phi_k^* & 0 \end{pmatrix} \begin{pmatrix} a_{\vec{k},s} \\ b_{\vec{k},s} \end{pmatrix}, \quad (2.8)$$

where

$$\phi_k = \left(e^{-i\vec{\delta}_1\cdot\vec{k}} + e^{-i\vec{\delta}_2\cdot\vec{k}} + e^{-i\vec{\delta}_3\cdot\vec{k}} \right), \quad (2.9)$$

see Appendix A for details of the calculation. The eigenvalues of the Hamiltonian (2.8), i.e. the electron bands, are

$$E_k = \pm t|\phi_k| \quad (2.10)$$

where - (+) corresponds to the valence (conduction) band. Due to the half filling discussed earlier, the valence band is completely filled and the conduction band is completely empty for charge-neutral graphene. By explicitly inserting the expression for the δ 's from Eqs. (2.3)-(2.5), the band structure given by Eq. (2.10) can be written in a somewhat more transparent way as [4, 43]

$$E_k = \pm t \sqrt{3 + 2 \cos(\sqrt{3}k_y a) + 4 \cos(\sqrt{3}k_y a/2) \cos(3k_x a/2)}. \quad (2.11)$$

This result was first obtained by Wallace [44] who studied single-layer graphite as early as 1947. The dispersion in Eq. (2.11) is shown in Fig. 2.2 where we clearly see the points where the two bands touch. These points are called the Dirac points and there are six of them in the first Brillouin zone. Out of these six, only two are independent (i.e., cannot be connected by the reciprocal lattice vectors) and linearizing the dispersion around these points, we obtain the dispersion [4, 43]

$$E_k = \pm \frac{3ta}{2} |\vec{k}| = \pm v_F |\vec{k}|, \quad (2.12)$$

where \vec{k} now is measured from the Dirac point we are linearizing around and we have defined the Fermi velocity $v_F = 3ta/2 \approx 10^6$ m/s.

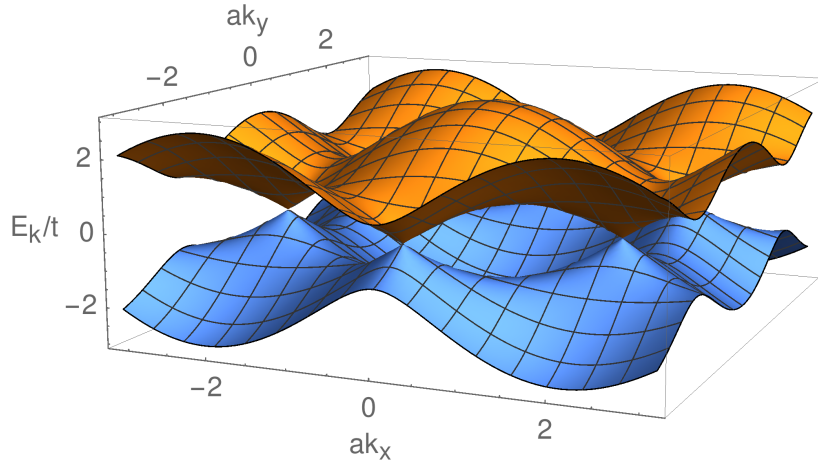


Figure 2.2: The tight-binding dispersion in equation (2.11). The blue surface is the valence band and the yellow surface is the conduction band.

Perhaps the most striking property that arises is that the low energy electrons behave as *massless* Dirac particles. The linear dispersion relation resembles the photon dispersion, but with the slope, i.e. the propagation speed, equal to v_F instead of c for photons. The speed of the Dirac electrons, v_F , is approximately $v_F \approx c/300$ (10^6 m/s).

Above, we simply linearized the dispersion relation to obtain the linear dispersion around the Dirac points. However, it is also possible to linearize the Hamiltonian and solve for the eigenenergies and eigenvectors. There are only two inequivalent points in the full dispersion to linearize around; we call these \vec{K} and \vec{K}' . From these two points it is possible to arrive at the other points by translating with the reciprocal lattice vectors, thus making the other points equivalent to K and K' . The linearized Hamiltonians that one obtains from the linearization procedure are [45]

$$\hat{H}_{\vec{K}}(\vec{k}) = v_F \begin{pmatrix} 0 & k_x - ik_y \\ k_x + ik_y & 0 \end{pmatrix} = v_F \vec{\sigma} \cdot \vec{k}, \quad (2.13)$$

$$\hat{H}_{\vec{K}'}(\vec{k}) = v_F \begin{pmatrix} 0 & k_x + ik_y \\ k_x - ik_y & 0 \end{pmatrix} = v_F (\vec{\sigma} \cdot \vec{k})^T, \quad (2.14)$$

where $\vec{\sigma} = (\sigma_x, \sigma_y)$, i.e., a vector of Pauli matrices. Now, the Hamiltonian $\hat{H}_{\vec{K}}$ acts on spinors for the \vec{K} valley and $\hat{H}_{\vec{K}'}$ on the spinors for the \vec{K}'

valley, i.e.,

$$\hat{H}_{\vec{K}} \begin{pmatrix} \psi_{KA}(\vec{k}) \\ \psi_{KB}(\vec{k}) \end{pmatrix} = E_k \begin{pmatrix} \psi_{KA}(\vec{k}) \\ \psi_{KB}(\vec{k}) \end{pmatrix}, \quad (2.15)$$

$$\hat{H}_{\vec{K}'} \begin{pmatrix} \psi_{K'A}(\vec{k}) \\ \psi_{K'B}(\vec{k}) \end{pmatrix} = E_k \begin{pmatrix} \psi_{K'A}(\vec{k}) \\ \psi_{K'B}(\vec{k}) \end{pmatrix}, \quad (2.16)$$

where the ψ subscripts denote the valley and A or B the sub-lattice that the wave function belongs to. It may sometimes be convenient to put all this together in one matrix equation construct and this can be done by putting the Hamiltonians in block-diagonal form

$$\begin{pmatrix} \hat{H}_{\vec{K}} & 0 \\ 0 & \hat{H}_{\vec{K}'} \end{pmatrix} \Psi(\vec{k}) = E_k \Psi(\vec{k}), \quad (2.17)$$

where

$$\Psi(\vec{k}) = \begin{pmatrix} \psi_{K,A}(\vec{k}) \\ \psi_{K,B}(\vec{k}) \\ \psi_{K',A}(\vec{k}) \\ \psi_{K',B}(\vec{k}) \end{pmatrix}. \quad (2.18)$$

In the interest of high degree of symmetry in the equations this is sometimes recast in a different form where one rearranges the K' spinor so that it has the same Hamiltonian as the K spinor:

$$\begin{pmatrix} \hat{H}_{\vec{K}} & 0 \\ 0 & \hat{H}_{\vec{K}} \end{pmatrix} \Psi_R(\vec{k}) = v_F \left(\tau_0 \otimes \vec{\sigma} \cdot \vec{k} \right) \Psi_R(\vec{k}) = E_k \Psi_R(\vec{k}), \quad (2.19)$$

where

$$\Psi_R(\vec{k}) = \begin{pmatrix} \psi_{K,A}(\vec{k}) \\ \psi_{K,B}(\vec{k}) \\ \psi_{K',B}(\vec{k}) \\ -\psi_{K',A}(\vec{k}) \end{pmatrix}, \quad (2.20)$$

denotes the rearranged 4-component vector and τ_0 is a unit matrix in valley indices.

Using the Hamiltonians (2.13) and (2.14), the momentum space eigen-spinors can be calculated [43]:

$$\psi_K(k) = \begin{pmatrix} \psi_{KA} \\ \psi_{KB} \end{pmatrix} = \frac{1}{\sqrt{2}} \begin{pmatrix} e^{-i\theta_k/2} \\ \pm e^{i\theta_k/2} \end{pmatrix}, \quad (2.21)$$

$$\psi_{K'}(k) = \begin{pmatrix} \psi_{K'A} \\ \psi_{K'B} \end{pmatrix} = \frac{1}{\sqrt{2}} \begin{pmatrix} e^{i\theta_k/2} \\ \pm e^{-i\theta_k/2} \end{pmatrix}, \quad (2.22)$$

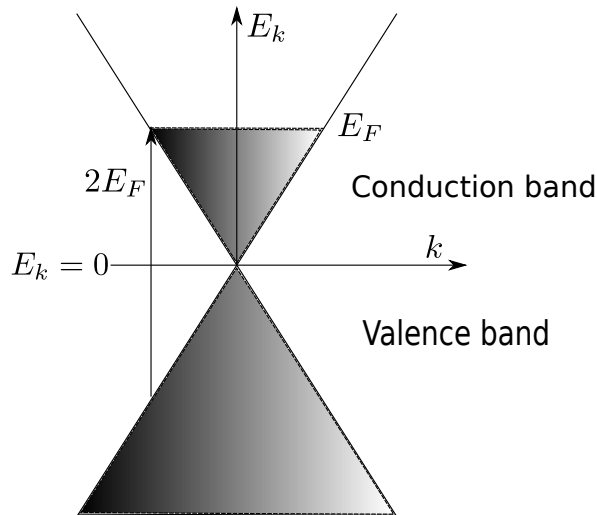


Figure 2.3: The low-energy dispersion for graphene electrons: the Dirac cone. The figure only shows a cross section of the cone. The positive energy band is the conduction band and the negative energy band is the valence band. When the Fermi energy is situated in the conduction band, the graphene is called electron doped and when the Fermi energy is in the valence band, it is called hole doped.

where $\theta_k = \arctan(k_x/k_y)$ and $+$ ($-$) means conduction (valence) band, and corresponds to the sign in Eq. (2.12). The eigenvalues of the Hamiltonians (2.13) and (2.14) reproduce the linear electron dispersion in Eq. (2.12).

The low-energy picture that has now emerged, described by the linear energy spectrum in Eq. (2.12) and the eigenspinors in Eqs. (2.21) and (2.22), can be visualized by the Dirac cone. This is depicted in Fig. 2.3 which shows the two linear energy bands, the conduction band (positive energy) and the valence band (negative energy), and the Fermi energy denotes the highest occupied state at zero temperature. As already mentioned, neutral graphene is filled to the Dirac point, i.e., to the vertex of the cone in Fig. 2.3. It can be noted that the A,B sublattices are now encoded in the vectorial structure of the eigenspinors. It is often convenient to work with only one of the eigenspinors when performing calculations of physical observables. Then the degeneracy of $g_s g_v = 4$ from spin and valley degeneracies need to be inserted in the final result.

2.1.1 Electron distribution and gating

As depicted in Fig. 2.3, the graphene band structure contains electrons that are distributed in energy. The charge carriers in graphene are fermions, and as such they obey the Fermi distribution

$$n_F(E_k) = \frac{1}{1 + e^{(E_k - \mu)/(k_B T)}}, \quad (2.23)$$

where μ is the chemical potential, and $E_k = \lambda v_F k$ is the energy of an electron at momentum k determined by Eq. 2.12. $\lambda = \pm$ signifies the band, with $+$ being the conduction band and $-$ being the valence band. The Fermi distribution describes the distribution of electrons in equilibrium, defined by two parameters μ and T . The zero-temperature chemical potential is usually called the Fermi energy and the chemical potential is fixed by enforcing particle conservation when the temperature is increased from zero.

The carrier density — or, equivalently, the chemical potential — can be tuned in graphene using a metal gate as was first shown in Ref. [23]. Pristine, undoped graphene is charge neutral and has a Fermi energy at the Dirac point, i.e. at zero energy in Fig. 2.3. The Fermi energy is related to the charge carrier density in graphene as [46]

$$E_F = v_F \sqrt{\pi n}, \quad (2.24)$$

or, equivalently,

$$n = \frac{E_F^2}{v_F^2 \pi}. \quad (2.25)$$

The Fermi energy can lie in the conduction band (electron doped) or in the valence band (hole doped). By changing the gate voltage between graphene and a metal gate, charges can be pushed into the graphene sample or extracted from it. Since these electrons (or holes) must occupy a state in the Fermi distribution, this raises or lowers the Fermi energy. The charge carrier density in graphene can be tuned significantly using a metal gate in close proximity to the graphene sheet. This effect is called the electric field effect and is present in more conventional conductors as well. However, the difference between these conductors and graphene is that the number of charge carriers in graphene is very small compared to other conductors, thus making small changes in the density more pronounced. Actually, pristine graphene has zero free charge carriers (at zero temperature) as the Fermi energy in this case lies at the Dirac point that separates the conduction and valence band. As an example of the large difference in number of charge carriers, we compare a μm^2 of graphene with a typical carrier density of 10^{12} cm^{-2} and a μm^3 of silver with a carrier density of $5.86 \times 10^{22} \text{ cm}^{-3}$ [29]. The resulting number of charge carriers are 10^4 for the patch of graphene, and 5.86×10^{10} for the silver cube. The difference of number of charge carriers is then more than a factor 10^6 , illustrating the point above.

There are also other ways, besides using electrostatic gating, of changing the carrier density of graphene. Examples are chemical doping with foreign

atoms and molecules [47] as well as photo-excitation of charge carriers [48]. Chemical doping can occur via surface transfer of electrons to/from dopants on the graphene surface or via substitution of carbon atoms in the graphene lattice with other elements [47].

So far we discussed electrons in equilibrium, which are fully described by the temperature and the chemical potential which sets the number of electrons. In general, systems can be in a complicated non-equilibrium state. A special non-equilibrium state can be achieved by letting a time independent force act on the system for a long time until the system no longer evolves in time. This is called a stationary state and it is a close non-equilibrium analogue of an equilibrium state, with the similarity being that neither system evolves in time. Under the action of an electric field bias across graphene and some electron scattering, needed to provide resistance for the electron movement, the stationary distribution will take the form [49]

$$f(E_k) = \frac{1}{1 + e^{(E_k - \vec{\beta} \cdot \vec{k} - \mu)/(k_B T)}}, \quad (2.26)$$

where E_k is the standard graphene electron dispersion, μ is the chemical potential, and $\vec{\beta}$ is the drift velocity. The difference between this stationary electron distribution and the equilibrium Fermi distribution is the appearance of the drift velocity. This shifts the electron distribution in a certain direction in k -space, so that more electrons move in a certain direction than in the opposite direction, i.e., a net DC current is flowing. This is only possible if a force is constantly forcing the electrons to move and the circuit is closed so that no charge build-up is occurring. This can be achieved by connecting two contacts and applying a DC bias across the graphene. How large the drift velocity is, i.e., how far from the equilibrium distribution the system evolves depends on the size of the voltage bias, the resistance of the sample, and subsequently on how large the current is. It can be noted that pushing a large DC current through graphene will tend to heat the graphene sample due to resistive heating. This can in principle be modeled since the temperature is already included in the distribution (2.26). In practice, however, the temperature is usually considered fixed and the heating effect is considered to be small, see e.g. Ref. [50]. This can be achieved with a good heat-sink attached to the system.

2.2 Graphene production methods — different types of graphene

Industrial use of graphene in large scale production requires low-cost production methods that are capable of producing good-quality graphene

samples [51]. There is also a need to develop laboratory-scale methods for good-quality graphene for use in prototype devices and fundamental studies. Graphene production presents a challenge and it was even believed for a long time that isolated graphene flakes were unstable due to thermal fluctuations [52] and, therefore, impossible to produce. From this standpoint, the successful isolation of graphene in Ref. [23] came as a surprise. Nowadays, graphene can be produced using a variety of methods [51] and a few select ones are mechanical exfoliation, chemical vapor deposition, epitaxial growth on silicon carbide, and liquid phase exfoliation. These methods have their benefits and drawbacks which we briefly discuss below.

A small note on graphene quality is in order before we treat graphene production methods. The quality of graphene is often quantified in terms of the electron mobility. High mobility means a high-quality sample. The mobility is limited by electron scattering which may come from different sources. We leave a more detailed treatment of the mobility and impurity scattering to section 2.3. Here, it is enough to know that one of the main difficulties in graphene production is to avoid introducing anything to the graphene that causes electron scattering, as this will reduce the mobility and hence the graphene quality.

Mechanical exfoliation — sometimes referred to as the scotch-tape method — is the original production method used by Novoselov *et al* in Ref. [23], which resulted in their Nobel prize in 2010. This method starts with a thin flake of graphite, which is exfoliated repeatedly using a sticky tape, yielding high quality samples of graphene. However, because of its labor intensive nature and small graphene sample sizes, this method is not suitable for large-scale production. Due to the high mobilities, it remains the method of choice for fundamental studies and prototype devices [51]. Using this method, room temperature mobilities of $140,000 \text{ cm}^2/(\text{Vs})$ [53] and low-temperature mobilities of $10^6 \text{ cm}^2/(\text{Vs})$ [42, 53] have been achieved.

Chemical Vapor Deposition (CVD) uses gaseous carbon to grow graphene on a substrate, usually copper although other substrates such as nickel or platinum are possible. This method is often seen as the most viable for large scale production as this can be performed over large areas of copper simultaneously. Using CVD, it is possible to produce graphene sheets as large as 30 inch (76 cm) across the diagonal [54]. The growth of graphene is a self-limiting process which stops the growth after the copper film is covered with graphene [51]. A drawback of the CVD method is that graphene ends up on top of copper, which is a conductor, something not very favorable for investigating the properties of graphene. To get graphene on

an insulator, many ways of either etching away the copper or transferring the graphene off the copper to some other substrate have been developed. However, this usually damages the graphene, especially when wet transfer methods are used. Using a dry transfer technique, mobilities up to 3×10^6 $\text{cm}^2/(\text{Vs})$ at low temperatures have recently been achieved when transferring onto hBN substrates [55], thus rivaling graphene produced using mechanical exfoliation.

Silicon carbide (SiC) is a layered material containing both silicon and carbon atoms. In a process called epitaxial growth, heating SiC to high temperatures facilitates evaporation of the Si atoms from the material and leaves graphene behind [51]. This is not a self-limiting process and the result may be that different number of graphene layers are mixed together in different areas. If graphene is grown on the Si(0001)-face, it creates a graphene layer with many of the carbon atoms creating a bond to the underlying SiC, this is usually referred to as the buffer layer [51]. By using hydrogen intercalation, this layer can be decoupled from the SiC to create a quasi-free-standing graphene layer on top of SiC. Using epitaxial growth on SiC, it is possible to produce cm-size graphene, but one of the main drawbacks of this method is the high price due to the high cost of the SiC wafers. Room-temperature mobilities ranging up to 10.000-30.000 $\text{cm}^2/(\text{Vs})$ have been achieved using epitaxial growth on SiC [51].

It is also possible to exfoliate graphite in a liquid environment, where ultrasound can be used to separate the graphene layers [51]. This is called liquid phase exfoliation and is scalable and cheap, as it has no need for potentially expensive substrates. The downside with the method is its small flake sizes and limited graphene quality, this may limit its usefulness for electronic and plasmonic purposes. However, this method can for instance be used to produce conducting inks containing graphene, which enables graphene-based printable electronics [56]. Furthermore, this method can be used to produce few-layer materials where one or several layers is a different material that has been intercalated into the graphite. This can be used to create materials with new exciting properties that can be different from those of graphene [51].

2.3 Impurities and scattering in graphene

In section 2.1, the graphene lattice was considered to be perfect and the equations were solved considering no edges and a completely translationally invariant system. However, we discussed in section 2.2 that depending on production method, there are various imperfections in the graphene lat-

tice as well as impurities attached to the surface of graphene. A complete in-depth investigation of different imperfections and impurities is beyond the scope of this thesis. We focus on general implications of imperfections for experiments and what information can be gathered from them.

Phonons exist both in graphene itself as well as in any substrate that may be used as a support for graphene. This has been shown to create a hybridization between the plasmons and the phonon modes, close to the bare phonon frequencies [57]. Considering that we often work below the intrinsic phonon mode at approximately 50 THz [57], we assume that we can neglect phonons in this thesis. The phonons can to some degree of approximation be thought of as being included in the electron relaxation time we include in our model. This approach was taken in Ref. [26], where the authors also constructed an energy dependent relaxation time to more accurately model the phonon effect.

Apart from phonons, the graphene lattice can contain charged impurities which seem to be a dominant source of electron scattering [58, 59], limiting the DC conductivity. The lattice can also contain vacancies which also affect the electron transport in graphene [46]. In addition, grain boundaries can exist where different domains are separated by extended lattice mismatches. It was found in Ref. [60] that midgap states may occur in vacancies and along grain boundaries, and this can have similar effects on the transport properties as charged impurity scattering. Furthermore, the presence of grain boundaries have theoretically been found to destroy the quantum hall effect in graphene, depending on the orientation of the grain boundaries [61]. In addition, the presence of imperfections has been shown to give rise to interesting behavior for electronic thermal transport in graphene. In particular, the Wiedemann-Franz law has been shown to be violated in the presence of randomly distributed impurities [62] as well as in the presence of midgap states [60].

A common way to quantify the quality of graphene samples is to measure the mobility. The mobility is related to the DC conductivity as [23]

$$\sigma = en\mu_m, \quad (2.27)$$

where e is the electron charge, n is the carrier density, and we denote the mobility with μ_m to avoid confusion with the chemical potential (commonly denoted with μ). Measuring the mobility effectively includes all scattering processes discussed above. The mobility is also related to the drift velocity as [29]

$$v_d = \mu_m E, \quad (2.28)$$

where v_d is the electron (or hole) drift velocity, i.e., the average velocity

of the charge carriers and E is the applied electric field. The mobility is usually given in units of $\text{cm}^2/(\text{Vs})$ and it varies between different graphene samples and production methods as we saw in section 2.2. Mobility is often inferred by measuring the DC resistivity (conductivity), and by also knowing the carrier density it is possible to extract the carrier mobility using Eq. (2.27). The mobility is limited by all the different scattering sources discussed above. To improve the quality of graphene samples, it is of interest to know what the impurities are in order to remove their effect. In the original graphene article by Novoselov *et al*, Ref. [23], mobilities up to $10^4 \text{ cm}^2/(\text{Vs})$ were found with essentially no temperature dependence, indicating that the mobility was impurity limited rather than phonon limited. Since the publication of this seminal article, much effort has been devoted to producing larger samples with higher mobilities, i.e., with less charged impurities. In more recent works, the mobility is increased by one order of magnitude, and at room temperature is found to be close to $10^5 \text{ cm}^2/(\text{Vs})$ [53, 63, 64]. This can be achieved by cleaning the graphene in-situ by sending a current through it which “burns” the impurities away and/or by encapsulating the graphene with hexagonal boron nitride (hBN) [65]. The latter is a recent development which simultaneously achieves several things; hBN is very flat which leads to the graphene laying flat on top [65], it has a lattice constant close to graphene so the graphene lattice is unstrained [65], and it can encapsulate the graphene to protect from particles in the environment [66]. It can be noted that the room-temperature mobility has been theoretically shown to be limited to roughly $10^5 \text{ cm}^2/(\text{Vs})$ due to phononic scattering [67].

By matching the conductivity in Eq. (2.27) with a simple Drude expression for the graphene conductivity, it is possible to relate the mobility and the DC relaxation time [26, 68]:

$$\tau = \frac{\mu_m E_F}{e v_F^2}. \quad (2.29)$$

This can be used to estimate relaxation times for the electrons from measurements of graphene mobility. Using data from experiments, these relaxation times range from 1 ps down to 20 fs [69], depending on the quality of graphene. As can be expected, the quality of graphene has implications for the plasmons in graphene. High-quality graphene, i.e., a long relaxation time, is advantageous for plasmonics; we will study this further in chapter 5.

Chapter 3

Green's Functions and Linear Response Theory

In this chapter we introduce Green's functions as a tool to calculate observable properties of graphene. We review basic concepts and then describe a linear response theory in terms of Green's functions. We apply this to calculate the nonlocal graphene conductivity — the conductivity is central for the optical as well as the plasmonic properties investigated later in this thesis. We evaluate the conductivity and investigate the differences between the nonlocal and the local conductivity.

Up to this point, graphene has been treated as a perfect lattice where all damping pathways — giving rise to the real part of the conductivity — arise from the excitation of electron-hole pairs. As discussed in chapter 2, graphene always contains a multitude of impurities and imperfections and a perfect-lattice model cannot capture all the physics of real graphene samples. To address this limitation, we discuss models for including impurities in graphene. First we consider a commonly used method due to Mermin, where electron relaxation is introduced in a phenomenological way. Next, we take advantage of the Green's function formalism and the ability to include impurities in a single-particle self energy term for the Green's function.

3.1 Green's functions

Green's functions are used in many branches of physics and one of their main advantages in quantum mechanics is the rather straightforward way in which observables can be calculated. Observable quantities are of course an important part of condensed matter physics as it allows us to test theories with experiments.

3.1.1 Mathematical definition

Although we will focus on Green's functions in quantum mechanics, it is instructive to first understand how the Green's function can express the solution to a differential equation. Consider the differential equation

$$\mathcal{L}\phi(x) = f(x), \quad (3.1)$$

where \mathcal{L} is a linear differential operator and f is some forcing function (source term). To solve this equation we must find a ϕ such that it is fulfilled. The Green's function allows us to do this for any function f . Consider the following equation:

$$\mathcal{L}G(x, x') = \delta(x - x'), \quad (3.2)$$

where G is the Green's function of \mathcal{L} . By now writing an ansatz of the solution to Eq. (3.1) as

$$\phi(x) = \int dx' G(x, x') f(x'), \quad (3.3)$$

we can insert this into the left hand side of Eq. (3.1) to obtain

$$\mathcal{L}\phi(x) = \mathcal{L} \int dx' G(x, x') f(x') = \int dx' \mathcal{L}G(x, x') f(x'). \quad (3.4)$$

Using the definition of the Green's function, Eq. (3.2), we find

$$\mathcal{L}\phi(x) = \int dx' \delta(x - x') f(x') = f(x), \quad (3.5)$$

which means that the ansatz $\phi(x)$ given by the Green's function construction in Eq. (3.3) satisfies the original equation, Eq. (3.1). Note that we made no assumption on the function $f(x)$, so the solution works for any function f . This shows the power and generality of the Green's function method. However, we did not actually find the Green's function that satisfies Eq. (3.2) and this can in general be quite difficult, but once it is found for some differential operator \mathcal{L} , the solution for any source term can be written down easily.

The step to Green's functions in quantum mechanics is to take Schrödinger's equation, i.e.,

$$\left(E - \hat{H}(x)\right) \psi(x) = 0, \quad (3.6)$$

as the operator \mathcal{L} . In Eq. (3.6), $\hat{H}(x)$ is the Hamiltonian operator. We can then define the Green's function as [70]

$$\left(E - \hat{H}(x)\right) G(x, x') = \delta(x - x'). \quad (3.7)$$

This can be written in a representation independent form as [70]

$$G^{r/a}(E) = \lim_{\eta \rightarrow 0} \left((E \pm i\eta)\mathbf{1} - \hat{H} \right)^{-1}, \quad (3.8)$$

where $+$ ($-$) gives the retarded (advanced) Green's function and $\mathbf{1}$ is an identity operator of appropriate size.

3.1.2 Equilibrium Green's function for graphene

By use of Eq. (3.8), the Dirac Hamiltonian in section 2.1 can be inverted and shown to have a Green's function on the form

$$G_0(\vec{k}, \varepsilon) = \frac{1}{2} \sum_{\lambda=\pm} \frac{1}{\varepsilon - \lambda E_k} \begin{pmatrix} 1 & \lambda e^{-i\phi_k} \\ \lambda e^{i\phi_k} & 1 \end{pmatrix}, \quad (3.9)$$

where $E_k = v_F k$, $k = |\vec{k}|$, and $\phi_k = \arg(k_x + ik_y)$, see Appendix B for details of the calculation. The energy should be interpreted as $\varepsilon \rightarrow \varepsilon + i\eta$ ($\varepsilon \rightarrow \varepsilon - i\eta$) where η is an infinitesimally small positive number for a correct definition of the retarded (advanced) Green's function. The matrix structure of the Green's function in Eq. (3.9) arises due to the underlying A,B sublattice in graphene.

For future reference we define

$$h^r(\vec{k}, \varepsilon) = \frac{1}{2} \sum_{\lambda=\pm} \frac{1}{\varepsilon - \lambda E_k - \Sigma^r(\varepsilon)}, \quad (3.10)$$

$$f^r(\vec{k}, \varepsilon) = \frac{1}{2} \sum_{\lambda=\pm} \frac{\lambda}{\varepsilon - \lambda E_k - \Sigma^r(\varepsilon)}, \quad (3.11)$$

and similarly for h^a and f^a . In writing Eqs. (3.10) and (3.11) we have also introduced the (retarded) self energy $\Sigma^r(\varepsilon)$. We will discuss this further in section 3.1.3. Here, we simply mention that we regain the bare Green's function in Eq. (3.9) by setting the retarded self energy $\Sigma^r(\varepsilon) = -i\eta$, and for the advanced self energy $\Sigma^a(\varepsilon) = i\eta$. This now lets us write the equilibrium Green's function as

$$G_0^x(\vec{k}, \varepsilon) = \begin{pmatrix} h^x(\vec{k}, \varepsilon) & f^x(\vec{k}, \varepsilon)e^{-i\phi_k} \\ f^x(\vec{k}, \varepsilon)e^{i\phi_k} & h^x(\vec{k}, \varepsilon) \end{pmatrix}, \quad (3.12)$$

where $x \in \{r, a\}$. The definitions in Eqs. (3.10) and (3.11) can also be used for any self energies and we will use this later in section 3.2.

The equilibrium Green's function in Eq. (3.9) can for instance be used

to compute the density of states for graphene electrons using the formula

$$\rho(\varepsilon) = -\frac{g_s g_v}{\pi} \text{Im} \left[\text{Tr} \int \frac{d^2 k}{(2\pi)^2} G_0(\vec{k}, \varepsilon) \right], \quad (3.13)$$

where Tr denotes trace and $g_s = g_v = 2$ are the spin and valley degeneracy factors. The off-diagonal Green's function components vanish when performing the angular integral and only the radial integral remains:

$$\rho(\varepsilon) = -\frac{g_s g_v}{2\pi^2} \text{Im} \left[\sum_{\lambda} \int_0^{k_c} dk \frac{k}{\varepsilon - \lambda v_F k} \right] \quad (3.14)$$

$$= \frac{g_s g_v \varepsilon}{2\pi^2 v_F^2} \text{Im} [\ln(\varepsilon - E_c) + \ln(\varepsilon + E_c) - 2\ln(\varepsilon)], \quad (3.15)$$

where k_c is a momentum cut-off and $E_c = v_F k_c$ is the energy cut-off. This energy cut-off is always much larger than ε and thus the first logarithm in Eq. (3.15) is always negative and contributes $i\pi$ to the expression. The second term has a real positive argument and can be dropped and the last term can be written as

$$\rho(\varepsilon) = \frac{g_s g_v \varepsilon}{2\pi^2 v_F^2} \left(\pi - \begin{cases} 2\text{Im}[\ln(\varepsilon)] & , \varepsilon > 0 \\ 2\text{Im}[i\pi + \ln(-\varepsilon)] & , \varepsilon < 0 \end{cases} \right) \quad (3.16)$$

where the \ln -terms are now real and can be dropped. The above expression can be written more compactly as

$$\rho(\varepsilon) = \frac{g_s g_v |\varepsilon|}{2\pi v_F^2}, \quad (3.17)$$

which is the final answer for the bare density of states. Graphene has, in addition to linear dispersion for the charge carriers, a linear density of states. This linear density of states is symmetric with respect to the Dirac point ($\varepsilon = 0$).

3.1.3 Non-equilibrium Green's function formalism

In this section we introduce a non-equilibrium Green's function formalism, originally due to Kadanoff and Baym [71] and Keldysh [72]. We shall refer to this as the Keldysh Green's function formalism or simply as the Keldysh formalism. We will only consider fermionic Green's functions and we introduce general concepts needed in the rest of the thesis, rather than focus on detailed derivations. Such details can be found in numerous publications [70, 71, 72, 73, 74].

Non-equilibrium Green's functions are far more general than equilibrium Green's function in that — as the name suggests — they also allow

us to describe systems out of equilibrium. Many situations of interest in condensed matter physics, and elsewhere, involve the description of transport of energy, charge or some other quantity. Such systems are not in equilibrium and as such they fall outside the descriptive range of equilibrium Green's functions. The standard way to handle this is to develop linear response theory in which the transport properties are described by using only the equilibrium properties of the system. Such descriptions can then be handled by linear response theory. The Keldysh formalism allows us to go beyond such response in powers of the perturbation. In this thesis, however, we develop a linear response theory, see section 3.2, in terms of the Keldysh formalism. Our reason for doing so is that the description of the linear response becomes rather general and many different physical aspects can be included in the modeling of the physical system. Much of the formalism can also be used to go beyond the linear response theory in a rather straightforward manner.

To define Green's functions it is sometimes useful to introduce field operators $\psi^\dagger(rt)$ ($\psi(rt)$), which are the creation (annihilation) operators for the field at point r and time t . We study fermionic field operators which obey the (equal time) anticommutation relations

$$\{\psi(rt), \psi^\dagger(r't)\} = \delta(r - r'), \quad (3.18)$$

where $\{ , \}$ denotes the anticommutator. The time-ordered (also called causal) Green's function can be written in terms of these field operators as [70]

$$G(rt, r't') = -i \frac{\langle \psi_0 | T [\psi(rt) \psi^\dagger(r't')] | \psi_0 \rangle}{\langle \psi_0 | \psi_0 \rangle}, \quad (3.19)$$

where T denotes the time-ordering operator. It explicitly puts the function with the largest time argument to the left in the expression. In the above definition of the Green's function we use the notation that rt denotes one argument which contains all spatial coordinates as well as the time coordinate. Thus, the Green's function has two arguments as in section 3.1.1.

The time-ordered Green's function turns out to allow for a well-defined perturbation expansion in equilibrium for perturbations to an unperturbed Hamiltonian. For non-equilibrium systems, this turns out to not be true in general and the insight of Kadanoff and Baym as well as Keldysh was that this problem can be handled by introducing more Green's functions defined along a non-trivial contour in complex time coordinates. Time-ordering along this contour gives rise to new Green's functions which expand the Green's function space.

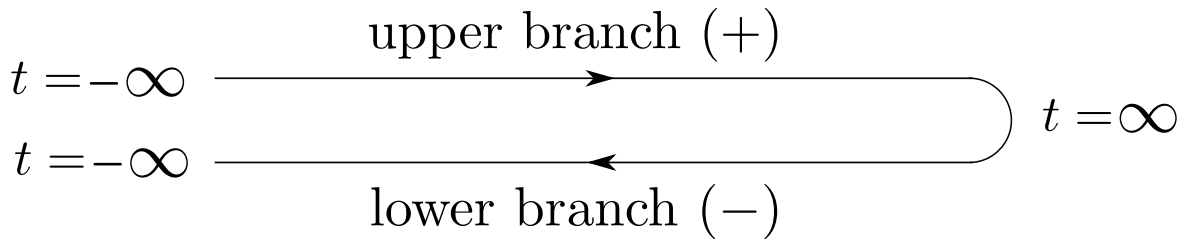


Figure 3.1: The Keldysh contour with the upper and lower branch of the contour. The matrix structure in Keldysh space arise from the possibility of the time arguments to lie on different contours. The contours themselves arise from the need to avoid any reference to the “final” state when working with systems out of equilibrium.

The Keldysh contour is depicted in Fig. 3.1 and it runs from minus infinity to infinity and back again. This ensures that we only make reference to the initial state ($t = -\infty$) and not the unknown final state ($t = \infty$) in the formalism. In equilibrium, the final state can safely be assumed to be the same as the initial state, but this is no longer true when the system is out of equilibrium. Ordering along this contour now means that on the upper (+) branch, time ordering is performed using T , and on the lower (−) branch, operators are anti-time ordered, i.e., the opposite of T . There are now four possibilities for where the two time arguments lie on this contour and we summarize the resulting Green's functions below:

1. $t \in +, t' \in +$: **time-ordered Green's function**

$$G^{++}(rt, r't') = -i\langle\psi_0|T[\psi(rt)\psi^\dagger(r't')]|\psi_0\rangle.$$

This is the same Green's function as we defined for equilibrium.

2. $t \in +, t' \in -$: **lesser Green's function**

$$G^{+-}(rt, r't') = i\langle\psi_0|\psi^\dagger(r't')\psi(rt)|\psi_0\rangle.$$

All times in the + branch are earlier on the contour than any time on the − branch. We can immediately put the operators in the correct order and no time ordering operator is needed.

3. $t \in -, t' \in +$: **greater Green's function**

$$G^{-+}(rt, r't') = -i\langle\psi_0|\psi(rt)\psi^\dagger(r't')|\psi_0\rangle.$$

Same argumentation as the for the lesser Green's function. The only difference is that we put the operators in the opposite order and pick up a minus sign due to the fermionic anticommutation of the field operators.

4. $t \in -, t' \in -$: **anti time-ordered Green's function**

$$G^{--}(rt, r't') = -i\langle\psi_0|\bar{T}[\psi(rt)\psi^\dagger(r't')]|\psi_0\rangle.$$

Here we have defined \bar{T} to do the opposite of T , i.e., it puts the largest time to the right in the expression. This ensures that the resulting Green's function has its operators ordered along the contour.

In what follow we will not explicitly write out the arguments of the Green's functions but it is to be understood that when nothing else is noted they are real space Green's functions with two arguments, rt and $r't'$, as above. The four Green's functions can be neatly put together in a 2-by-2 matrix form

$$\tilde{G} = \begin{pmatrix} G^{++} & G^{+-} \\ G^{-+} & G^{--} \end{pmatrix}, \quad (3.20)$$

where the tilde on \tilde{G} denotes Keldysh space. It is important to keep in mind that the Keldysh matrix structure is completely unrelated to the A-B sublattice matrix structure of the equilibrium Green's function in Eq. (3.9), although they appear similar in form.

From Eq. (3.20) it seems like there are four Green's functions to solve for but upon inspection of the definitions 1-4 above, one can show that the functions are not all independent. For instance

$$G^{++} + G^{--} = G^{+-} + G^{-+}, \quad (3.21)$$

and furthermore one can find the relationships

$$G^r = G^{++} - G^{+-} = G^{-+} - G^{--}, \quad (3.22)$$

$$G^a = G^{++} - G^{-+} = G^{+-} - G^{--}, \quad (3.23)$$

$$(3.24)$$

where r denotes retarded, a denotes advanced Green's function. By also defining the Keldysh Green's function as

$$G^K = G^{++} + G^{--} = G^{+-} + G^{-+}, \quad (3.25)$$

we may rewrite the Keldysh space expression in Eq. (3.20) from the contour $(+-)$ into retarded, advanced, and Keldysh functions, using the unitary transformation

$$\check{G} = U\tilde{G}U^{-1} = \begin{pmatrix} 0 & G^a \\ G^r & G^K \end{pmatrix}, \quad (3.26)$$

$$U = \frac{1}{\sqrt{2}} \begin{pmatrix} 1 & -1 \\ 1 & 1 \end{pmatrix}, \quad (3.27)$$

where the caron on \check{G} denotes the so-called triangular representation of Keldysh space. The functions G^r and G^a are almost always related to each other [70], meaning there are only two independent functions to be determined, G^r and G^K . In equilibrium, this reduces to one unknown function as expected, since the Keldysh Green's function is then determined by the retarded and advanced components as [70]

$$G_{\text{eq}}^K(p, \varepsilon) = f(\varepsilon) (G_{\text{eq}}^r(p, \varepsilon) - G_{\text{eq}}^a(p, \varepsilon)), \quad (3.28)$$

where $f(\varepsilon) = \tanh(\beta(\varepsilon - \mu)/2) = (1 - 2n_F(\varepsilon))$, $\beta = 1/(k_B T)$, and $n_F(\varepsilon)$ is the Fermi function, Eq. (2.23).

Using the triangular representation (or equivalently the contour representation), it can be shown that analogous to the equilibrium case, it is possible to formulate a well defined perturbation expansion of the Green's function and arrive at the Dyson equation [73]

$$\check{G} = \check{g} + \check{g} \circ \check{\Sigma} \circ \check{G}, \quad (3.29)$$

where \circ denotes summation/integration over common internal variables and $\check{g} = \begin{pmatrix} 0 & g^a \\ g^r & g^K \end{pmatrix}$ is the Green's function in absence of the perturbation which gives rise to the self energy term. It is important to note that in the triangular representation, $\check{\Sigma}$ is written

$$\check{\Sigma} = \begin{pmatrix} \Sigma^K & \Sigma^r \\ \Sigma^a & 0 \end{pmatrix}. \quad (3.30)$$

Eq. (3.29) can be inverted to obtain

$$(\check{\varepsilon} - \check{H}_0 - \check{\Sigma}) \circ \check{G} = \check{\delta}, \quad (3.31)$$

where $\check{\delta}$ is a delta function in the remaining variables. The real-space full Dyson equation, Eq. (3.29), can also be Fourier transformed and assuming translational invariance of the system, we arrive at an expression for the full Green's function in reciprocal space:

$$\check{G}(p, \varepsilon) = (\check{G}_0(p, \varepsilon)^{-1} - \check{\Sigma}(p, \varepsilon))^{-1} = (\check{\varepsilon} - \check{H}_0 - \check{\Sigma}(p, \varepsilon))^{-1}. \quad (3.32)$$

Writing out the equations in Eq. (3.29) explicitly yields

$$G^{r/a} = g^{r/a} + g^{r/a} \circ \Sigma^{r/a} \circ G^{r/a}, \quad (3.33)$$

$$G^K = g^K + g^K \circ \Sigma^a \circ G^a + g^r \circ \Sigma^r \circ G^K + g^r \circ \Sigma^K \circ G^a, \quad (3.34)$$

where it can be seen that the non-equilibrium Keldysh Green's function depends explicitly on the retarded/advanced Green's function. The equation for the retarded/advanced component is identical to the equilibrium equation and its solution is needed in order to determine the Keldysh Green's function which contains the non-equilibrium information. In Keldysh formalism, expectation values of observables are computed as

$$\langle \hat{\mathcal{O}}(xt) \rangle = \lim_{x't' \rightarrow xt^+} \frac{i}{2} \text{Tr} \left[\hat{\mathcal{O}}(xt) G^K(xt, x't') \right]. \quad (3.35)$$

This makes it clear that the Keldysh Green's function provides a convenient way to obtain knowledge of a system since $\hat{\mathcal{O}}(xt)$ can be any observable. Examples of relevance in this thesis are the current and the density operators. Eq. (3.35) is valid for systems in equilibrium as well as for non-equilibrium systems.

3.2 Linear response in Keldysh formalism

Linear response theory is an important technique with which we may investigate non-equilibrium properties of quantum mechanical systems by considering them to be infinitesimally close to equilibrium. The main simplification arises from the fact that non-equilibrium properties in linear response actually only depend on the equilibrium or unperturbed quantities. For example, we will see that the electrical conductivity depends on the unperturbed Green's function, albeit in a non-trivial way.

We will treat linear response within the Keldysh formalism, which is strictly speaking not necessary as was discussed in section 3.1.3. Many linear response treatments, see e.g., [75, 76, 77], are performed with equilibrium Green's functions exactly due to the fact that the linear response depends on the unperturbed Green's function which is taken to be in equilibrium. The general formalism presented here is valid also for systems where the unperturbed state is taken to be a non-equilibrium state. The explicit results we present in the end are, however, valid for systems in equilibrium only. We will make it clear during the derivation when we depart from the general case. We will see that the algebra involved in using Keldysh Green's functions for the linear response is not very complicated due to the 2-by-2 matrix structure.

The starting point for a linear response calculation is to consider a total Hamiltonian on the form

$$\check{H} = \check{H}_0 + \delta\check{H}, \quad (3.36)$$

where \check{H}_0 has a known (Keldysh) Green's function \check{G}_0 and $\delta\check{H}$ is a small perturbation written in Keldysh space. We write an ansatz for the Green's function of the total Hamiltonian as $\check{G} = \check{G}_0 + \delta\check{G}$, i.e., the full Green's function is only perturbed slightly from the unperturbed one. Inserting this ansatz into the Dyson equation, Eq. (3.31), we obtain

$$(\check{\varepsilon} - \check{H}_0 - \delta\check{H}) \circ (\check{G}_0 + \delta\check{G}) = \check{\delta} \quad (3.37)$$

and by using that by definition $(\check{\varepsilon} - \check{H}_0) \circ \check{G}_0 = \check{\delta}$, we obtain

$$(\check{\varepsilon} - \check{H}_0 - \delta\check{H}) \circ \delta\check{G} = \delta\check{H} \circ \check{G}_0. \quad (3.38)$$

We now observe that the term $\delta\check{H} \circ \delta\check{G}$ is second order in the perturbation and we drop it since we seek the linear response. For sufficiently small perturbations we expect this approximation to be good, indeed most materials exhibit a linear response to electromagnetic fields [78]. Dropping the second order term allows us to rewrite Eq. (3.38) into an equation

determining the perturbation to the Green's function as

$$\delta\check{G} = \check{G}_0 \circ \delta\check{H} \circ \check{G}_0. \quad (3.39)$$

As alluded to above, we see that the perturbation to the Green's function, $\delta\check{G}$, indeed depends only on the unperturbed Green's function together with the perturbation itself. We may now insert this into the formula for the expectation value, Eq. (3.35), and we obtain

$$\langle \hat{\mathcal{O}}(xt) \rangle = \lim_{x't' \rightarrow xt^+} \frac{i}{2} \text{Tr} \left[\hat{\mathcal{O}}(xt) (G_0^K(xt, x't') + \delta G^K(xt, x't')) \right] \quad (3.40)$$

and from this we define the unperturbed expectation value

$$\langle \hat{\mathcal{O}}(xt) \rangle_0 = \lim_{x't' \rightarrow xt^+} \frac{i}{2} \text{Tr} \left[\hat{\mathcal{O}}(xt) G_0^K(xt, x't') \right]. \quad (3.41)$$

We may then write the deviation of the expectation value from its unperturbed value as

$$\delta \mathcal{O}(xt) = \langle \hat{\mathcal{O}}(xt) \rangle - \langle \hat{\mathcal{O}}(xt) \rangle_0 = \lim_{x't' \rightarrow xt^+} \frac{i}{2} \text{Tr} \left[\hat{\mathcal{O}}(xt) \delta G^K(xt, x't') \right]. \quad (3.42)$$

Eqs. (3.39) and (3.42) express the linear response of any observable due to a perturbation in terms of Keldysh Green's functions. To proceed, we must specify the perturbation $\delta\check{H}$ and also the observable $\hat{\mathcal{O}}$ we are interested in calculating. We must of course also specify the unperturbed Hamiltonian but in our case this is naturally the graphene Hamiltonian and the unperturbed Green's function is given by Eq. (3.9).

We will derive an expression for the polarizability (charge-charge correlation function) which is defined as the charge density response to a scalar potential response [75]. This determines all quantities needed to apply the expression for the expectation value in Eq. (3.42). The observable we consider is the density that is written in A-B sublattice space as $\hat{\rho} = \begin{pmatrix} 1 & 0 \\ 0 & 1 \end{pmatrix}$ and the perturbation to the Hamiltonian written on the Keldysh path is given by $\delta\check{H} = \begin{pmatrix} \delta V & 0 \\ 0 & -\delta V \end{pmatrix}$. We remember that we used a rotation given by Eq. (3.27), and by transforming the perturbation using $X \rightarrow UXU^{-1}$ we find that the perturbation in the triangular representation is written like

$$\delta\check{H} = \begin{pmatrix} 0 & \delta V \\ \delta V & 0 \end{pmatrix}. \quad (3.43)$$

The perturbation has the form

$$\delta V = \begin{pmatrix} \delta V_0 & 0 \\ 0 & \delta V_0 \end{pmatrix} e^{i(q \cdot x - \omega t)}, \quad (3.44)$$

where δV_0 is the (scalar) amplitude of the perturbation and the matrix structure is in A-B sublattice space (so this matrix should not be rotated in Keldysh space). It should be noted that by using the \circ operator we implicitly mean all real space functions to be functions of two real space arguments. The local perturbation in Eq. (3.44) has only one spatial argument, but we can easily remedy this by adding a $\delta(x - y)$ which makes the local nature of the perturbation explicit.

The perturbation given by Eqs. (3.43) and (3.44) is inserted into Eq. (3.39) to find the explicit expression for the Green's function perturbation:

$$\delta\check{G} = \begin{pmatrix} 0 & G_0^a \\ G_0^r & G_0^K \end{pmatrix} \circ \begin{pmatrix} 0 & \delta V \\ \delta V & 0 \end{pmatrix} \circ \begin{pmatrix} 0 & G_0^a \\ G_0^r & G_0^K \end{pmatrix} \quad (3.45)$$

$$= \begin{pmatrix} 0 & G_0^a \circ \delta V \circ G_0^a \\ G_0^r \circ \delta V \circ G_0^r & G_0^K \circ \delta V \circ G_0^a + G_0^r \circ \delta V \circ G_0^K \end{pmatrix}. \quad (3.46)$$

We conclude that the Keldysh part of the perturbation to the Green's function is

$$\delta G^K = G_0^K \circ \delta V \circ G_0^a + G_0^r \circ \delta V \circ G_0^K. \quad (3.47)$$

We are interested in this Green's function since this allows us to calculate the average of the observable using Eq. (3.42). We must remember that \circ means summation over all internal variables, meaning that there are implicit integrations in the above expression for the Green's function perturbation. To see this, we explicitly write out the first term with all its arguments and integrations explicitly

$$\begin{aligned} G_0^K \circ \delta V \circ G_0^a &= \int dy dy' G_0^K(x, y) \delta V(y) \delta(y - y') G_0^a(y', x') \\ &= \int dy G_0^K(x, y) \delta V(y) G_0^a(y, x'), \end{aligned} \quad (3.48)$$

where the coordinates represent both spatial coordinate and time, and the delta function dependence comes from the local nature of the perturbation. Now, we are interested in the Fourier transform of the expectation value and we take the Fourier transform of Eq. (3.42). By assuming that the Green's functions exhibit translational invariance, we can arrive at an expression for the Fourier transform of the expectation value of the density perturbation as

$$\begin{aligned} \delta n(q, \omega) &= \frac{ig_s g_v}{2} \int \frac{d^2 p}{(2\pi)^2} \frac{d\varepsilon}{2\pi} \text{Tr} \left[\begin{pmatrix} 1 & 0 \\ 0 & 1 \end{pmatrix} (G_0^K(p, \varepsilon) G_0^a(p_-, \varepsilon_-) \right. \\ &\quad \left. + G_0^r(p, \varepsilon) G_0^K(p_-, \varepsilon_-)) \delta V_0 \right], \end{aligned} \quad (3.49)$$

where we have introduced the degeneracy factor $g_s g_v$, the unit matrix is the density operator in A-B sublattice space, $p_- = p - q$, $\varepsilon_- = \varepsilon - \omega$, and δn denotes the expectation value of the deviation from the equilibrium density. From Eq. (3.49), we can extract a very general expression for the polarizability

$$\begin{aligned} \Pi(q, \omega) = \frac{ig_s g_v}{2} \int \frac{d^2 p}{(2\pi)^2} \frac{d\varepsilon}{2\pi} \text{Tr} \left[(G_0^K(p, \varepsilon) G_0^a(p_-, \varepsilon_-) \right. \\ \left. + G_0^r(p, \varepsilon) G_0^K(p_-, \varepsilon_-)) \right], \end{aligned} \quad (3.50)$$

which follows from the definition $\delta n(q, \omega) = \Pi(q, \omega) \delta V_0$ [75].

To proceed, we now make explicit that the unperturbed Green's function, G_0 , is in equilibrium and we make use of the rewriting of the Green's function defined in Eqs. (3.10)-(3.12). This can be inserted into Eq. (3.50), and performing the matrix multiplications we obtain

$$\begin{aligned} \Pi(q, \omega) = ig_s g_v \int \frac{d^2 p}{(2\pi)^2} \frac{d\varepsilon}{2\pi} \left(h^r h_-^K + h^K h_-^a \right. \\ \left. + \cos(\phi_p - \phi_{p_-}) (f^r f_-^K + f^K f_-^a) \right), \end{aligned} \quad (3.51)$$

where we used the notation that subscript “-” means that the function is evaluated at the argument (p_-, ε_-) and no subscript means the function is evaluated at (p, ε) . Eq. (3.51) is valid for graphene Green's functions with arbitrary self energies.

We now take the clean limit, i.e., we use the self energy $\Sigma^r(\varepsilon) = -i\eta^+$, ($\Sigma^a(\varepsilon) = i\eta^+$) and we find that

$$\int d\varepsilon (\tanh(\varepsilon_{\pm}\beta/2) h^r h_{\pm}^r - \tanh(\varepsilon\beta/2) h^a h_{\pm}^a) = 0, \quad (3.52)$$

$$\int d\varepsilon (\tanh(\varepsilon_{\pm}\beta/2) f^r f_{\pm}^r - \tanh(\varepsilon\beta/2) f^a f_{\pm}^a) = 0, \quad (3.53)$$

which allows us to obtain

$$\begin{aligned} \Pi(q, \omega) = ig_s g_v \int \frac{d^2 p}{(2\pi)^2} \frac{d\varepsilon}{2\pi} \left[(h^r h_-^a + \cos(\phi_p - \phi_{p_-}) f^r f_-^a) \right. \\ \left. \times (\tanh(\varepsilon\beta/2) - \tanh(\varepsilon_- \beta/2)) \right], \end{aligned} \quad (3.54)$$

where we have used Eq. (3.28) to eliminate the Keldysh component. Performing the energy integral by the method of residues, we obtain contributions from the poles of h and f , and the contributions from the poles of

the tanh terms cancel. By rewriting tanh in terms of the Fermi function and inserting the definitions of h and f , we obtain the final expression

$$\Pi(q, \omega) = g_s g_v \lim_{\eta^+ \rightarrow 0^+} \int \frac{d^2 p}{(2\pi)^2} \sum_{\lambda, \lambda'} \frac{n_F(\lambda' E_{p-}) - n_F(\lambda E_p)}{\omega + \lambda' E_{p-} - \lambda E_p + i\eta^+} F_{\lambda\lambda'}(p), \quad (3.55)$$

$$F_{\lambda\lambda'}(p) = \frac{1 + \lambda\lambda' \cos(\phi_p - \phi_{p-})}{2}. \quad (3.56)$$

Eq. (3.55) is a well-known expression for the clean-case polarizability and serves as the starting point for many linear response calculations. The graphene polarizability at zero temperature was first calculated by Wunsch *et al* [21] and by Hwang and Das Sarma [20]. This was later generalized to finite temperatures by Ramezanali *et al* [27]. In all these calculations, Eq. (3.55) was taken as a starting point and the calculations are valid in the clean limit.

It might seem that in our derivation here we took a complicated detour to re-derive a known expression, but in fact we accomplished a lot more. For the clean limit, it is indeed the case that starting from Eq. (3.55) would suffice, but during our derivation we arrived at general expressions for the polarizability that have a wider range of applicability. First of all, Eq. (3.50) is valid for non-equilibrium systems, and by taking this as the starting point we can compute the polarizability for any system with a known Hamiltonian. Furthermore, Eq. (3.51) is valid for graphene with impurities that can be captured by a Green's function self energy. Thus, by taking this equation as our starting point we can calculate the linear response coefficient for graphene under rather general conditions. We only need to be able to compute an expression for the self energy of the problem. We leave such considerations for section 3.5 and in the following two sections we deal with the expression arrived at in the clean limit, i.e., Eq. (3.55).

3.3 Graphene conductivity in the clean limit

The longitudinal conductivity of graphene can be expressed in terms of the polarizability (charge-charge correlation function) [79] that was obtained in the previous section, or the current susceptibility (current-current correlation function) [75, 79]. Due to gauge invariance, these two are equivalent and the longitudinal conductivity is uniquely defined [77], and one may use the expression one finds most convenient. It should be noted that the transverse response is more general as it can handle both longitudinal

and transverse perturbations. Since we are interested in the longitudinal response, we use the polarizability to obtain the conductivity. This circumvents the complication of the anomalous commutator term needed to properly handle the current-current response in graphene [80, 81].

By definition, the polarizability $\Pi(q, \omega)$ is related to the density response as [75]

$$n(q, \omega) = \Pi(q, \omega)V(q, \omega), \quad (3.57)$$

where $V(q, \omega)$ is the perturbing potential. Now, the potential is related to the electric field by $E = -\nabla V$, which in reciprocal space becomes $E(q, \omega) = -iqV(q, \omega)$. Substituting this into Eq. (3.57), we obtain

$$n(q, \omega) = \frac{i}{q}\Pi(q, \omega)E(q, \omega). \quad (3.58)$$

The continuity equation in reciprocal space

$$\omega n(q, \omega) = qj(q, \omega), \quad (3.59)$$

can now be used to write Eq. (3.58) in terms of the current response as

$$j(q, \omega) = \frac{i\omega}{q^2}\Pi(q, \omega)E(q, \omega). \quad (3.60)$$

In Eq. (3.59), we have assumed that $\vec{q} \parallel \vec{j}$, which is only valid in the longitudinal case. Thus, Eq. (3.60) is only valid for longitudinal perturbations. We recognize that the quantity relating the electric field with the current is nothing but the conductivity. From Eq. (3.60), we identify the longitudinal conductivity to be

$$\sigma(q, \omega) = \frac{i\omega}{q^2}\Pi(q, \omega), \quad (3.61)$$

which is valid for a general $\Pi(q, \omega)$.

Now, the clean graphene conductivity is obtained by taking Eq. (3.61) with $\Pi(q, \omega)$ given by Eq. (3.55). The full answer for the nonlocal conductivity is rather lengthy and we refrain from writing it down in full detail and refer to Refs. [20, 21, 27] for the full expressions. For zero temperature, the result can be written down in a closed form involving only known functions, while in the finite temperature result there remains an integral to be performed numerically. The local conductivity ($q \rightarrow 0$) at finite

temperature is [82, 83]

$$\begin{aligned}
\sigma(\omega) &= \sigma_1(\omega) + i\sigma_2(\omega), \\
\sigma_1(\omega) &= \frac{e^2}{4}G(\omega/2), \\
\sigma_2(\omega) &= \frac{e^2}{4} \left(\frac{8T}{\omega\pi} \ln \left[2 \cosh \left(\frac{\mu}{2T} \right) \right] \right. \\
&\quad \left. + \frac{4\omega}{\pi} \int_0^\infty \frac{G(x) - G(\omega/2)}{\omega^2 - 4x^2} dx \right), \\
G(x) &= \frac{\sinh(x/T)}{\cosh(\mu/T) + \cosh(x/T)}, \tag{3.62}
\end{aligned}$$

where μ is the chemical potential and T is the temperature.

Figures showing the conductivity are provided in the next section, where we also compare the clean conductivity considered in the present section with the conductivity obtained when adding a relaxation time.

3.4 Mermin relaxation time approximation

The graphene conductivity obtained by using the polarizability in Eq. (3.55) was arrived at by assuming pristine graphene and includes thermal and nonlocal effects. One of the main drawbacks of the pristine conductivity is that it fails to reproduce a finite real DC conductivity and the well known real Drude peak for low frequencies. This peak at low frequencies is well known from metals and is experimentally found to exist also for graphene [84]. This means that graphene contains phonons or impurities of some kind, which are so far not included in our model for graphene electrons. The impurities could be carbon-atom dislocations or substitutions, grain boundaries in the graphene sheet, or particles that are stuck on the graphene surface. Quite possibly a combination of these effects is what creates the electron scattering which gives rise to the finite DC conductivity, see section 2.3 for a discussion.

One way to model electron relaxation is provided by including a phenomenological electron relaxation time. One such model, due to Mermin [85], dates back to 1970 and is widely used in graphene plasmonics to include plasmon losses, see e.g. Refs. [26, 68, 86, 87]. The Mermin relaxation time approximation uses the pristine response function which is calculated in the absence of the electron relaxation and provides a prescription for how to insert the relaxation time without changing the number of particles in the system. This would happen by using the naive substitution

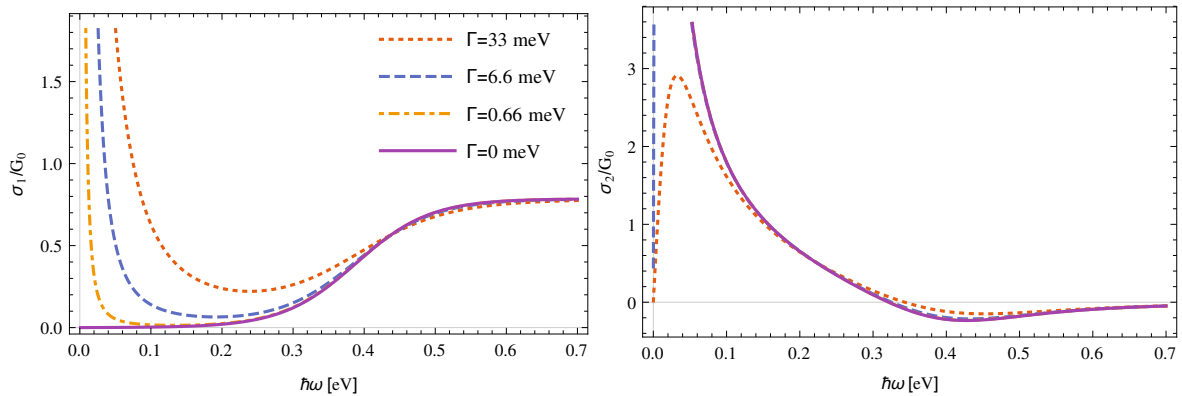


Figure 3.2: Local conductivity versus frequency for various values of the inverse scattering time Γ . The expressions used are Eqs. (3.62) and (3.63), with real part (left panel) and imaginary part (right panel) shown. The additional parameters used in the plot are $E_F = 0.2$ eV and $T = 300$ K ($k_B T = 0.026$ eV). The relaxation times in the figure are $\tau = \infty$ ps ($\Gamma = 0$ meV), $\tau = 1$ ps ($\Gamma = 0.66$ meV), $\tau = 100$ fs ($\Gamma = 6.6$ meV), and $\tau = 20$ fs ($\Gamma = 33$ meV).

$\omega \rightarrow \omega + i\Gamma$, where Γ is the inverse scattering time.

The key realization in Mermin's method is that the electrons, which are subject to the external electric field as well as relaxation by some scattering, are relaxing not to the global Fermi distribution but to a local equilibrium. This local equilibrium can have a spatial dependence as an effect of a spatially varying perturbation. For a detailed treatment of the Mermin relaxation time approximation, we refer to Refs. [85, 88]. In what follows we only give the final result and consider its implications.

The result from Mermin's method is a polarizability of the form [85, 88]

$$\Pi(q, \omega) = \frac{\left(1 + \frac{i\Gamma}{\omega}\right) \Pi^0(q, \omega + i\Gamma)}{1 + \frac{i\Gamma}{\omega} \frac{\Pi^0(q, \omega + i\Gamma)}{\Pi^0(q, 0)}}, \quad (3.63)$$

where Π^0 refers to the clean-limit polarizability in Eq. (3.55). The Mermin polarizability can then be used in Eq. (3.61) to obtain the conductivity in the presence of the electron relaxation. It should be emphasized that the main benefit with Mermin's method is its simplicity; it uses only the clean-limit result evaluated at complex energies in order to find the result which includes relaxation. However, the Mermin relaxation time approximation is phenomenological and the relaxation time is added by hand without any microscopic mechanism for the relaxation.

Fig. 3.2 shows the local conductivity, $q \rightarrow 0$, for various values of the inverse relaxation time Γ . The local conductivity for $\Gamma = 0$, i.e., the clean case, is given by the expression in Eq. (3.62). It can be seen that increasing Γ substantially changes the conductivity and we note especially the appearance of the Drude peak for low frequencies.

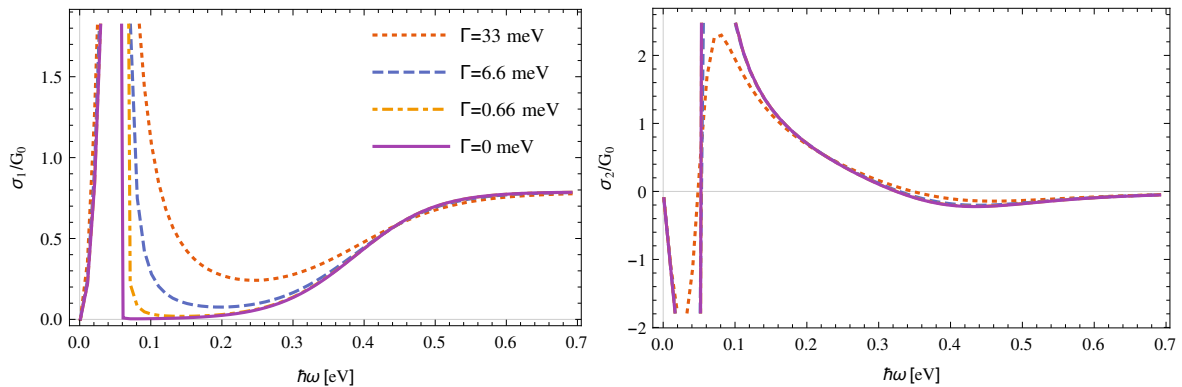


Figure 3.3: Nonlocal conductivity vs frequency at $q/k_F = 0.3$ for various values of the inverse scattering time Γ . The additional parameters used in the plot are $E_F = 0.2$ eV and $T = 300$ K ($k_B T = 0.026$ eV). The relaxation times in the figure are $\tau = \infty$ ps ($\Gamma = 0$ meV), $\tau = 1$ ps ($\Gamma = 0.66$ meV), $\tau = 100$ fs ($\Gamma = 6.6$ meV), and $\tau = 20$ fs ($\Gamma = 33$ meV).

Fig. 3.3 shows the nonlocal conductivity for $q/k_F = 0.3$ and otherwise identical parameters as the local conductivity in Fig. 3.2. A comparison of Figs. 3.2 and 3.3 is provided in Fig. 3.4 and shows that the conductivity changes rather substantially as a function of q . For this reason, it could be important to consider the nonlocality when dealing with perturbations of sufficiently small wavelengths. We will return to this in chapter 5.

3.5 Green's function self energy

In the previous section we discussed an approach to include electron relaxation in a phenomenological way. In this section, we discuss a microscopic approach to add losses to the graphene electrons by including a scattering term in the Hamiltonian. Such a scattering term can be modeled using t-matrix formalism, see e.g., Refs. [73, 75, 89]. The t-matrix formalism is a method that treats impurity scattering with a random distribution of impurity sites. An average on impurity positions can be taken and this allows for evaluation of a self-energy term resulting from the impurities. We treat the case of a dilute density of impurity sites, dilute in the sense that the fraction of lattice sites containing impurities $n_{\text{imp}} \ll 1$. This simplifies the problem of finding the self energy since interference terms between different impurity sites can be neglected.

Using the t-matrix approach, we may set up a perturbation theory for the scattering term addition to the bare graphene Hamiltonian along the lines of Eq. (3.32). The scattering term contributes to the self energy that is to be included in the pristine graphene Green's function in Eq. (3.9). Calculating the conductivity from the Green's function with a self energy can be done using Eq. (3.51) and performing the integrals. Some care

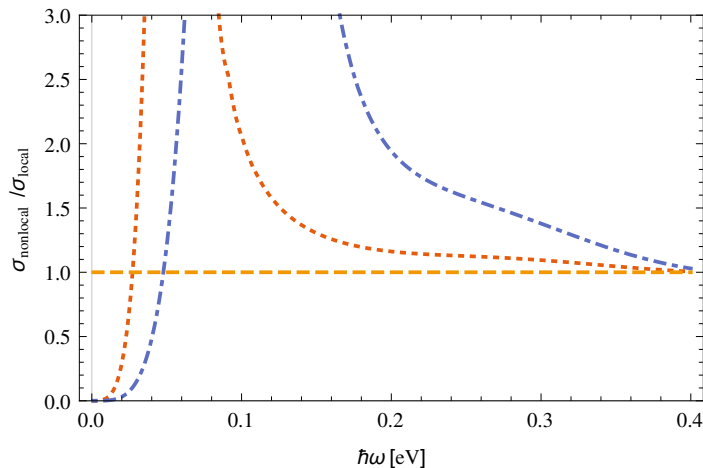


Figure 3.4: Real part of the nonlocal conductivity divided with the real part of the local conductivity from Figs. 3.2 and 3.3. Both conductivities are for the case $\Gamma = 6.6$ meV and $T = 300$ K. The nonlocal conductivity is several times larger for some frequencies. The position of this peak depends on the momentum, in this figure the nonlocal conductivity is evaluated at $q/k_F = 0.3$ (red dotted curve) and $q/k_F = 0.6$ (blue dot-dashed curve). The yellow dashed line shows unity, or $\sigma_{\text{local}}/\sigma_{\text{local}}$ to highlight that the nonlocal conductivity approaches the local conductivity for frequencies around $2E_F$ (0.4 eV) in this figure.

must be taken when evaluating the poles of this Green's function and we refer to Papers III and IV for a detailed treatment.

Using the t-matrix approach, the retarded component of the momentum-space Dyson equation, Eq. (3.32), in the case of graphene with pointlike S-wave scatterers, becomes

$$G^r(p, \varepsilon) = \frac{1}{2} \sum_{\lambda=\pm} \frac{1}{\varepsilon - \lambda E_p - \Sigma^r(\varepsilon)} \begin{pmatrix} 1 & \lambda e^{-i\phi_p} \\ \lambda e^{i\phi_p} & 1 \end{pmatrix}. \quad (3.64)$$

This is nothing but the bare graphene Green's function together with a correction given by the self energy. The self energy — which in general depends also on p — depends only on ε due to the pointlike and S-wave nature of the scatterers. The addition of the scattering term to the bare graphene Hamiltonian is included in the self energy, and the task is to evaluate or calculate the self energy for any particular model of electron scattering. Below we consider two such models — one model for interaction with a distribution of adatoms coupled to the graphene lattice by tunneling, and one self-consistent model for evaluating the Green's function together with the self energy for a dilute density of randomly distributed impurity sites.

In principle, the presence of a self energy can alter the linear response formulation that we considered in section 3.2. The perturbation applied to the system, can alter not only the Green's function as we considered, but with a self energy there can also be an induced perturbation to lin-

ear order of the self energy. This is called vertex corrections and this is typically a small correction since it is proportional to the perturbation as well as the self energy itself. The self energy is already a correction to the bare Hamiltonian and is typically small, making the vertex correction suppressed. For the cases we consider below, i.e., within a t-matrix formulation of pointlike S-wave scatterers, it turns out that the vertex correction are identically zero.

3.5.1 Adatoms coupled to graphene

Atoms in close proximity to the graphene lattice — we will refer to them as adatoms — can cause the graphene electrons to tunnel into the adatoms, provided there is an empty electron state for the graphene electron to tunnel into. The electron can then tunnel back into the lattice and, in the limit of a dilute density, there are no direct tunneling events between the adatoms themselves. The Hamiltonian we consider for this reads

$$\hat{H} = \sum_l \varepsilon_0 \hat{d}_l^\dagger \hat{d}_l + \sum_{p,\lambda} \left(\lambda E_p \hat{c}_{p\lambda}^\dagger \hat{c}_{p\lambda} + \sum_l (t_{l,p,\lambda} \hat{d}_l^\dagger \hat{c}_{p,\lambda} + \text{h.c.}) \right), \quad (3.65)$$

where \hat{d}_l (\hat{d}_l^\dagger) annihilates (creates) an electron on the adatom at position x_l and $\hat{c}_{p,\lambda}$ ($\hat{c}_{p,\lambda}^\dagger$) annihilates (creates) an electron in the graphene lattice with momentum p in band λ . Furthermore, p is the momentum, $t_{l,p,\lambda} = \lambda \tilde{t} e^{ip \cdot x_l}$, \tilde{t} is the bare adatom-carbon atom coupling, ε_0 is the energy level of the adatom, $\lambda = \pm$ is the graphene band index and x_l is the position of the l -th impurity.

In the dilute limit with no interference effect, the individual adatoms can then be treated as an average density and the impurity-averaged self energy can be shown to take the form

$$\Sigma^r(\varepsilon) = \frac{|t|^2}{\varepsilon + i\delta - \varepsilon_0}, \quad (3.66)$$

$$|t|^2 = n_{\text{imp}} |\tilde{t}|^2, \quad (3.67)$$

where n_{imp} is the fraction of impurities per lattice site, and δ is the bare inverse lifetime of the adatom electron states. The values of ε_0 , δ , and \tilde{t} are phenomenological parameters and external input from either first-principle calculations or experiments are needed to fix them. The adatom density n_{imp} is a free parameter that may vary between different graphene samples and this can be seen to affect the effective tunneling amplitude t .

The appearance of the self energy term changes the poles of the Green's function, which is apparent from Eq. (3.64). The self energy in Eq. (3.66)

inserted in the Green's function, Eq. (3.64), yields the poles

$$\varepsilon_\lambda^\pm = \frac{\lambda E_p + \varepsilon_0 - i\delta \pm \sqrt{(\lambda E_p - \varepsilon_0 + i\delta)^2 + 4|t|^2}}{2}. \quad (3.68)$$

Remember that we used the pole structure of the Green's functions to arrive at the expression in Eq. (3.55) for $\Pi(q, \omega)$, which gave us the conductivity. Thus, with the changed pole structure in the case of the adatom self energy, this equation is no longer valid and the starting point needs to be Eq. (3.51). We leave out this calculation here and refer to Paper III for the details.

3.5.2 Dilute distribution of impurity sites — a self-consistent treatment

To treat impurity scattering, we consider a distribution of random scattering sites with identical strength V_{imp} . We consider a low density n_{imp} of such sites, meaning that only a small fraction of lattice sites contain a scatterer. Furthermore, we consider only s-wave scattering, i.e., the scattering is non-directional. These approximations are standard in t-matrix formulations of impurity scattering [73, 89].

The Hamiltonian for the scattering can be written as

$$\hat{H} = \hat{H}_0 + \sum_m \hat{V}_m, \quad (3.69)$$

where \hat{V}_m are the scattering potentials at some (random) sites. Using an averaging procedure over the random sites, it is possible to arrive at equations for the Green's function (Dyson's equation) as well as an equation for the self energy. The self energy depends on the impurity scattering as well as the full Green's function itself, thus giving two self-consistent equations to solve. In the calculation, we neglect interference terms between the different impurity sites with the argument that they are far apart and should not influence each other. Thus the assumption of a dilute density of scatterers is important. We also note that the impurities are treated as fixed and "rigid" objects that do not absorb any energy or momentum in the scattering process.

Following the steps in the preceding discussion gives the Dyson equation together with an equation for the impurity averaged self energy:

$$G^r(p, \varepsilon) = \frac{1}{2} \sum_{\lambda=\pm} \frac{1}{\varepsilon - \lambda E_p - \Sigma^r(\varepsilon)} \begin{pmatrix} 1 & \lambda e^{-i\phi_p} \\ \lambda e^{i\phi_p} & 1 \end{pmatrix}, \quad (3.70)$$

$$\Sigma^r(\varepsilon) = \frac{n_{\text{imp}} V_{\text{imp}}}{1 - V_{\text{imp}} \sum_p G(p, \varepsilon)}, \quad (3.71)$$

and these need to be solved self-consistently. The polarizability, and hence the conductivity, can again be calculated using Eq. (3.51). The Green's function obtained by numerically solving Eqs. (3.70) and (3.71) has poles that must also be found numerically. To this end, the numerical self energy obtained from the solution can be fitted to the form of the analytic self energy in Eq. (3.66), and the approximate poles can be found analytically. With these poles as initial guesses, a numerical root finder routine can be employed to find the exact poles of the numerical Green's function. With the knowledge of the poles, it is possible to evaluate the conductivity, using Eq. (3.51), and proceed to investigate the plasmon properties. For details, we refer to Paper IV.

Chapter 4

The Maxwell Equations

We discuss the Maxwell equations and some of their most important properties and related quantities. We pay special attention to the coupling between the electromagnetic field and matter, as described by the dielectric function and the conductivity. These quantities will play important roles later in the thesis when describing the plasmonic properties of materials. The work presented in this thesis is focused around the ability of graphene plasmons to affect electromagnetic radiation scattered from interfaces supporting plasmons. Before studying this directly, we here investigate electromagnetic propagation and scattering from a single sheet of graphene, and also scattering in more complex dielectric environments. Such environments are necessary for coupling electromagnetic radiation to the plasmons, but they also provide added difficulties in solving the scattering problem. At the end of the chapter, we treat in some detail two different methods for solving the scattering problem in such environments: an analytical model and a numerical model. Both methods have been used throughout the work leading to this thesis.

4.1 The Maxwell equations and light propagation

The basic equations that govern the interaction between electromagnetism and matter are the Maxwell equations. These equations describe classical electromagnetic fields of any frequency and wavelength under most imaginable conditions. Thus, they govern the behavior of visible light, radio waves, ultraviolet (UV) radiation, as well as infrared light and X rays. It is clear from this list that the study of Maxwell's equations encompasses many different fields of technological as well as scientific relevance.

The macroscopic Maxwell equations [78]

$$\nabla \cdot \vec{D} = \rho, \quad (4.1)$$

$$\nabla \times \vec{H} - \frac{\partial \vec{D}}{\partial t} = \vec{j}, \quad (4.2)$$

$$\nabla \times \vec{E} + \frac{\partial \vec{B}}{\partial t} = 0, \quad (4.3)$$

$$\nabla \cdot \vec{B} = 0, \quad (4.4)$$

contain four fields $(\vec{E}, \vec{D}, \vec{H}, \vec{B})$. These are called the electric field, displacement field, magnetic field strength and magnetic induction field respectively. In vacuum, we have the well known relationships $\vec{D} = \epsilon_0 \vec{E}$ and $\vec{B} = \mu_0 \vec{H}$, where ϵ_0 and μ_0 are the vacuum values of the permittivity and permeability, respectively, with $\sqrt{\frac{1}{\epsilon_0 \mu_0}} = c$. In addition, ρ is the charge density and \vec{j} is the current density.

In a more general situation, there might be a medium present that behaves differently from vacuum. With “medium” we mean a material with charges that respond to external electric fields. Basically any material fits this description, but here we consider solid materials such as metals or semiconductors. The charges in the medium respond when an external field is applied and this can alter the relationships between the electromagnetic fields. In general [78],

$$\vec{D} = \epsilon_0 \vec{E} + \vec{P}, \quad (4.5)$$

$$\vec{B} = \mu_0 \vec{H} + \vec{M}, \quad (4.6)$$

where \vec{P} and \vec{M} are the polarization field and magnetization field respectively. This means that we add the polarization field to the vacuum value of the displacement field and likewise the magnetization to the vacuum value of the magnetic induction. The naming convention for the \vec{B} and \vec{H} fields changes between different sources in the literature, we will refer to both fields as the magnetic field.

In what follows, we will mainly be interested in the \vec{D} and \vec{E} fields since they are governing the ability of the medium to respond to electric fields. Furthermore, many materials exhibit a very weak magnetization and from now on we assume that the magnetization \vec{M} is zero and thus $\vec{B} = \mu_0 \vec{H}$, i.e., the same as for vacuum. We will also make a very important simplification in the treatment of electric fields surrounding materials. We will only consider the linear response of the material, meaning that the response, i.e., \vec{P} , is proportional to the external field \vec{E} . There are different

ways to justify this, but the simplest justification is that this behavior is what most systems exhibit for accessible field strengths. At very high electric fields this assumption may break down, but we will not consider such cases. Consequently, we may now write the polarization as $\vec{P} = \epsilon_0 \chi \vec{E}$, i.e.,

$$\vec{D} = \epsilon_0 \vec{E} + \vec{P} = \epsilon_0 \vec{E} (1 + \chi), \quad (4.7)$$

where χ is the (electric) *susceptibility* of the medium. We may now define a new electric permittivity (compare with the vacuum electric permittivity) as $\tilde{\epsilon} = \epsilon_0 (1 + \chi)$ and the *dielectric function* (relative permittivity) as

$$\epsilon = \frac{\tilde{\epsilon}}{\epsilon_0} = 1 + \chi, \quad (4.8)$$

giving us

$$\vec{D} = \tilde{\epsilon} \vec{E}. \quad (4.9)$$

The vacuum permittivity has been altered by the susceptible medium, thus giving rise to a different displacement field. From Eqs. (4.8) and (4.9), it is clear that a susceptibility of zero reproduces the vacuum value for the \vec{D} field.

4.1.1 Nonlocal electromagnetic properties

It is important to point out that the displacement field and the electric current can be nonlocal in space and time [1, 78]:

$$\vec{D}(\vec{x}, t) = \int d\vec{x}' dt' \epsilon(\vec{x} - \vec{x}', t - t') \vec{E}(\vec{x}', t'), \quad (4.10)$$

$$\vec{j}(\vec{x}, t) = \int d\vec{x}' dt' \sigma(\vec{x} - \vec{x}', t - t') \vec{E}(\vec{x}', t'). \quad (4.11)$$

By considering the system to have been under continuous illumination for a very long time, the electric field, the dielectric function (ϵ), and the conductivity (σ) can be written as Fourier transforms. By also applying a Fourier transform on the displacement field and the current we obtain

$$\vec{D}(\vec{k}, \omega) = \epsilon(\vec{k}, \omega) \vec{E}(\vec{k}, \omega), \quad (4.12)$$

$$\vec{j}(\vec{k}, \omega) = \sigma(\vec{k}, \omega) \vec{E}(\vec{k}, \omega), \quad (4.13)$$

since the Fourier transform has the property that it turns a convolution into a product. This shows that the equations linking different quantities are simpler in reciprocal space and that the response (i.e., the current and the displacement field) to an electric field with frequency ω and modulation \vec{k} , follows the same frequency and modulation. The quantities ϵ and σ are

material parameters that are either calculated or measured and can then be included in the electromagnetic modeling. In general, σ and ϵ can be second-order tensors, the fact that we only consider scalars reflects that we consider an isotropic medium.

From the Maxwell equations, it is possible to relate the bulk conductivity and permittivity as [1]

$$\epsilon(\vec{k}, \omega) = 1 + \frac{i\sigma(\vec{k}, \omega)}{\epsilon_0\omega}. \quad (4.14)$$

To properly model these material properties it is thus important to consider the frequency and momentum behavior. Modeling the ω -dependence poses no significant problem as the values of material parameters can be measured rather easily and simple models for the frequency behavior of material parameters exist [78]. Such models are usually based on Drude-type behavior for the conductivity [90], and an oscillator-type model for the dielectric function [78]. The importance of the \vec{k} dependence of the dielectric constant and the conductivity is determined by the magnitude $|\vec{k}|$ of the incident field, compared with the inverse of a typical length of the system. In metals such as gold and silver, both the lattice constant and the Fermi wavelength are on the order of a few Å [91], so for wavelengths much larger than this there is usually no need to include nonlocal effects in calculations. The exception is if the patterning of the material is on the order of a few nanometers, making it comparable to the Fermi wavelength. Nonlocal effects may then be of importance since the system is probing length scales where the quantum effects of electrons become noticeable.

Progress in nanofabrication has enabled the investigation of small metal nanoparticles — with dimensions close to the Fermi wavelength — and their electromagnetic response. It has been shown experimentally that such nanoparticles exhibit features not readily explained by a local response theory [92, 93, 94, 95]. This has created activity in modeling these nonlocal properties stretching back several decades in time. Early works focused on describing these size dependent effects by introducing a phenomenological size-dependent damping term [96, 97, 98]. More recently, semiclassical hydrodynamic models have been proposed, which include pressure effects [99] as well as charge diffusion effects [100]. In addition, electron tunneling between metallic structures in very close proximity can affect the optical response [101].

Effects of nonlocality have also been demonstrated for graphene structures [102]. To model graphene, we are aided by the fact that a rather

simple model of electrons can explain the observed low-energy band structure and this allows us to compute analytically the nonlocal conductivity from a microscopic picture, see chapter 3. This enables us to investigate the nonlocal properties of graphene and in particular the implications for graphene plasmons in rather straightforward terms.

4.1.2 Electromagnetic energy and propagation

An important concept in Maxwell's equations is the energy carried by the electromagnetic field. The nature of its propagation is important for understanding and interpreting electromagnetic scattering from various objects. In this thesis we treat the electromagnetic field as a classical field and one question that arises is; how does the electromagnetic field propagate? The well-known answer is that it propagates as waves, which can be seen by forming a wave equation by combining Eqs. (4.2) and (4.3). It is then possible to arrive at wave equations for the electric and the magnetic fields.

For linear and non-dispersive media, the energy density contained in the electromagnetic field is [78]

$$u = \frac{1}{2} \left(\vec{E} \cdot \vec{D} + \vec{H} \cdot \vec{B} \right) \quad (4.15)$$

and can be written as

$$u = \frac{1}{2} \left(\epsilon \vec{E}^2 + \mu \vec{H}^2 \right). \quad (4.16)$$

The rate of change of the energy density is then

$$\frac{\partial u}{\partial t} = \vec{E} \cdot \frac{\partial \vec{D}}{\partial t} + \vec{H} \cdot \frac{\partial \vec{B}}{\partial t}, \quad (4.17)$$

and using Eqs. (4.2) and (4.3) as well as the vector identity

$$\nabla \cdot \left(\vec{E} \times \vec{H} \right) = \vec{H} \cdot \left(\nabla \times \vec{E} \right) - \vec{E} \cdot \left(\nabla \times \vec{H} \right), \quad (4.18)$$

Eq. (4.17) can be written as

$$\frac{\partial u}{\partial t} + \nabla \cdot \left(\vec{E} \times \vec{H} \right) = -\vec{j} \cdot \vec{E}. \quad (4.19)$$

This can be rewritten into

$$\frac{\partial u}{\partial t} + \nabla \cdot \vec{S} = -\vec{j} \cdot \vec{E}, \quad (4.20)$$

where we have defined the (instantaneous) Poynting vector

$$\vec{S} = \vec{E} \times \vec{H}. \quad (4.21)$$

From the structure of the Poynting vector, we can see that the energy propagation is always perpendicular to the electric and magnetic field. Eq. (4.21) is usually referred to as Poynting's theorem and expresses energy conservation. To better illustrate this, we integrate Eq. (4.20) over some arbitrary volume V , and use Gauss' theorem (the divergence theorem) to obtain

$$\int_V \frac{\partial u}{\partial t} dx^3 = - \int_V \vec{j} \cdot \vec{E} dx^3 - \int_{\partial V} \hat{n} \cdot \vec{S} dx^2, \quad (4.22)$$

where ∂V denotes the boundary of V , and \hat{n} is a unit vector perpendicular to the surface ∂V pointing outwards. This tells us that the rate of change of the energy inside the volume V , is equal to the total rate of work performed inside the volume and the amount of energy flow through the boundary ∂V of the volume.

We are often interested in the energy flow of monochromatic plane waves

$$\vec{E} = \vec{E}_0 e^{i(\vec{k} \cdot \vec{x} - \omega t)}, \quad (4.23)$$

$$\vec{B} = \frac{1}{\omega} \vec{k} \times \vec{E}_0 e^{i(\vec{k} \cdot \vec{x} - \omega t)}, \quad (4.24)$$

where Eq. (4.3) has been used to relate the electric and magnetic fields. Note that we are now working with complex-valued notation for the fields, so we can calculate the time-averaged Poynting vector as [78]

$$\langle \vec{S} \rangle = \frac{1}{2} \text{Re} \left[\vec{E} \times \vec{H}^* \right], \quad (4.25)$$

which expresses energy conservation. Using Eq. (4.25) together with the plane wave fields in Eqs. (4.23) and (4.24) we obtain

$$\langle \vec{S} \rangle = \hat{k} \frac{1}{2\eta} \left| \vec{E}_0 \right|^2, \quad (4.26)$$

where \hat{k} is a unit vector pointing in the direction of the momentum \vec{k} and $\eta = \sqrt{\frac{\mu}{\epsilon}}$ is the wave impedance (in vacuum this has the value $\eta_0 \approx 376.7 \Omega$).

Eq. (4.26) can be utilized to compute the energy flow across boundaries between different media. The energy flow depends on the square of the electric field amplitude as well as the permittivity and permeability of the medium in question. One way to investigate the amount of reflected and transmitted energy is thus to match plane waves across the boundary of

the media and solve for the electric field coefficients. Together with the material parameters, the field amplitudes can be inserted in Eq. (4.26) to give the amount of energy transmitted or reflected from the boundary. When this is divided by the incident power, this is usually called the reflectance and transmittance.

4.2 Electromagnetic scattering from a conducting interface

To study electromagnetic scattering from a conducting interface, such as a graphene sheet, we need the boundary conditions for electromagnetic fields at the interface. The boundary conditions for the electromagnetic fields are [78]

$$(\vec{D}_2 - \vec{D}_1) \cdot \vec{n} = \rho_s, \quad (4.27)$$

$$(\vec{B}_2 - \vec{B}_1) \cdot \vec{n} = 0, \quad (4.28)$$

$$\vec{n} \times (\vec{E}_2 - \vec{E}_1) = 0, \quad (4.29)$$

$$\vec{n} \times (\vec{H}_2 - \vec{H}_1) = \vec{j}_s, \quad (4.30)$$

where subscript 1 (2) means the field evaluated above (below) the interface, \vec{n} is a vector with unit length perpendicular to the interface pointing from 1 to 2, and ρ_s and \vec{j}_s is the surface charge and surface current, respectively. The charge and the current are understood to only exist on the boundary between the two media.

To study electromagnetic scattering from a conducting interface, the energy flow can be analyzed as described in the previous section. The normal-incidence results for reflectance and transmittance are [103]

$$\text{reflected energy, } R = \left| \frac{\epsilon_2 + \sigma(\omega) - \sqrt{\epsilon_1 \epsilon_2}}{\epsilon_2 + \sigma(\omega) + \sqrt{\epsilon_1 \epsilon_2}} \right|^2 \quad (4.31)$$

$$\text{transmitted energy, } T = \frac{4\epsilon_2 \sqrt{\epsilon_1 \epsilon_2}}{|\epsilon_2 + \sigma(\omega) + \sqrt{\epsilon_1 \epsilon_2}|^2} \quad (4.32)$$

from which we can obtain the absorbance from energy conservation as

$$\text{absorbed energy, } A = 1 - R - T = \frac{4\sqrt{\epsilon_1 \epsilon_2} \sigma_1(\omega)}{|\epsilon_2 + \sigma(\omega) + \sqrt{\epsilon_1 \epsilon_2}|^2}, \quad (4.33)$$

where $\sigma(\omega) = \sigma_1(\omega) + i\sigma_2(\omega)$. The fact that the scattering coefficients depend on the conductivity of the sheet makes the scattering coefficients frequency dependent. Normal-incidence light scattering from a planar

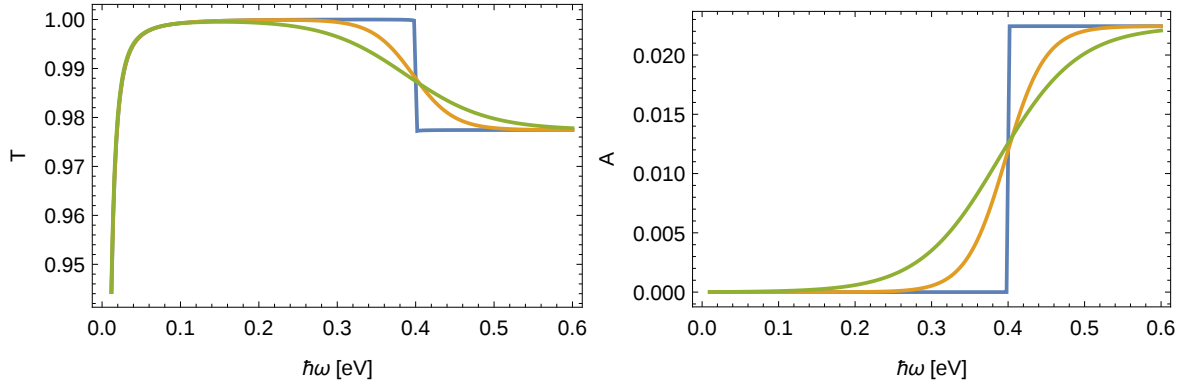


Figure 4.1: Transmission and absorption through a graphene sheet in vacuum, calculated from Eqs. (4.31) and (4.33) with $E_F = 0.2$. The different colors represent different temperatures with blue curves 0 K, yellow curves 150 K, and green curves 300 K. The local conductivity is calculated using Eq. (3.62). For high frequencies the absorption approaches the graphene characteristic 2.3%.

interface with no spatial variations only depends on the local conductivity, i.e., the results do not depend on momentum k .

Fig. 4.1 shows the scattering coefficients, Eqs. (4.31)-(4.33) for a graphene sheet in vacuum using the local conductivity from Eq. (3.62), with $E_F = 0.2$ eV for different temperatures. There is a transition in all scattering coefficients at $\hbar\omega = 2E_F$ which represents the onset of interband transitions. For zero temperature this is a sharp transition which is smeared out due to thermal broadening of the Fermi distribution for non-zero temperatures. For high frequencies compared with the Fermi energy, the absorption approaches the value 2.3% which is characteristic for graphene [104].

It is worth noticing that the scattering results in Fig. 4.1, although containing information about the graphene sample, contains no signature of graphene plasmons. The reason for this is that electromagnetic radiation does not couple to plasmons unless the environment contains a coupling structure. In the next section, we treat solution methods for the scattering problem in such structures, but we postpone the treatment of graphene plasmons and their properties to chapter 5.

4.3 Solution methods for complex light scattering problems

In the previous section we discussed the rather simple solution to the electromagnetic scattering problem for a planar and homogeneous sheet. In this case, the conductivity included in the scattering coefficients depended only on the frequency and not the momentum, making the local conductivity sufficient for this problem. As alluded to above, it is impossible to probe plasmons in such a configuration [1]. The key issue is to bridge the

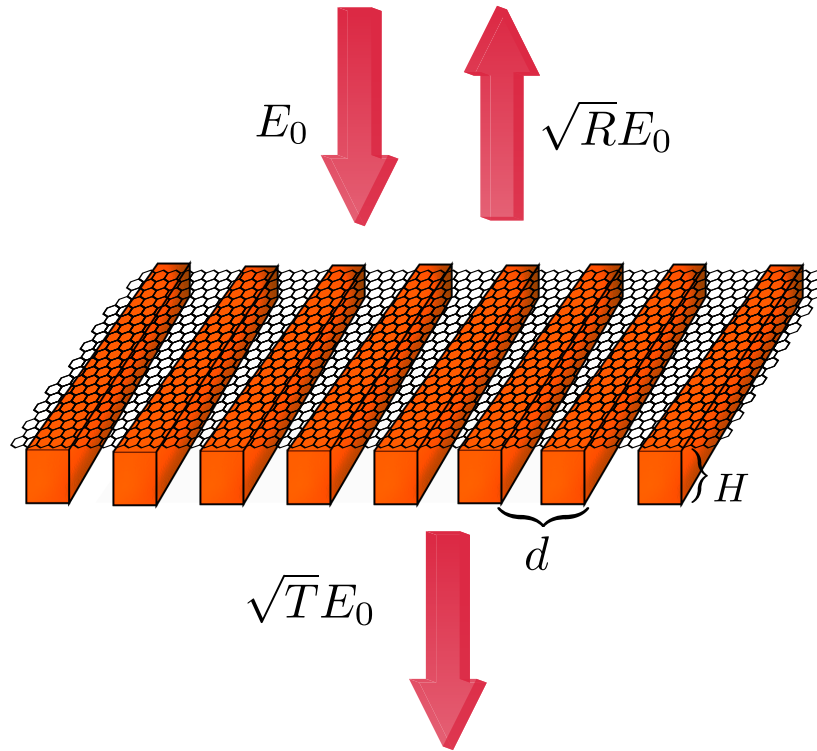


Figure 4.2: A graphene sheet with a grating. The red arrows represent electromagnetic radiation used to probe the plasmons.

wavelength mismatch between plasmons and the incident electromagnetic radiation. This will be discussed in more detail in chapter 5; here we only note that this is a problem that needs to be overcome in order to study plasmons. One way to achieve this is to introduce periodicity in either graphene or the surrounding environment. In such environments it can be important to consider the nonlocal behavior of the conductivity.

The route taken in this thesis is to pattern the dielectric environment surrounding the graphene. The environment is patterned into an array that is periodic in one dimension and translationally invariant in the other, see Fig. 4.2. This is usually called a dielectric grating and the periodicity is used to facilitate the coupling. Simply put, the inverse of the grating periodicity, $k = \frac{2\pi}{d}$, is supplied to the momentum of the incoming light and when this matches the plasmon momentum, coupling between the incident radiation and the graphene plasmon is possible.

The solution procedure for such infinitely periodic structures is more complicated than for the scattering problem of the homogeneous sheet that was treated in section 4.2. The solution procedure needs to treat the periodic structure as well as the conducting sheet and include the possibility of evanescent modes inside the periodic structure. In the following, we discuss two different methods to solve this scattering problem.

In section 4.3.1 we discuss the scattering matrix (S-matrix) method, which is a very general method to treat scattering problems in different branches of physics. One advantage with this method is the possibility to carry out much of the calculation using matrix algebra with comparatively small matrices, thus reducing computation times. Another advantage is the flexibility in dividing the problem domain into different regions with separate scattering matrices and the possibility to combine them into one scattering matrix in the end.

Section 4.3.2 contains a treatment of the Finite Element Method (FEM) with focus on the basic concepts, since there exists numerous commercial softwares that automatically perform these steps. The main difference between FEM and the S-matrix approach is that while FEM is a real space solver, the S-matrix is a momentum space solver that works in reciprocal space. One implication of this is that FEM often requires heavy numerical calculations while the S-matrix method in principle only needs final evaluation of matrix multiplications to yield the final answer. A benefit of using FEM in general, is its ability to handle arbitrary geometries without much added difficulty. The treatment of FEM in section 4.3.2 includes a discussion of the Floquet boundary condition, an important concept for periodic structures when the incident radiation contains a phase shift between the periodic boundaries.

4.3.1 Scattering matrix method

In this section, we cover the basic concepts of the S-matrix method, for a more detailed treatment we refer to Appendix B in Paper I and the article from which the method is adapted, Ref. [105]. Note that in our treatment here, we restrict the discussion to normal incidence.

The periodic scattering problem is depicted in Fig. 4.3 which shows the unit cell and the division of the problem into separate regions. The starting point of the S-matrix method is to use the periodicity and write the electric and magnetic fields as Fourier series of the form

$$A(x) = \sum_n A_n e^{ik_n x}, \quad (4.34)$$

where $k_n = 2\pi n/d$, d is the length of the unit cell, and n is an integer. The dielectric function and the sheet conductivity are also written as Fourier

ω^2 . This means that if the in-plane momentum k_j of a particular mode j is larger than ω , by necessity β_j is imaginary and the mode is evanescent (decaying) in the z direction (perpendicular to the graphene sheet). Note that the field configuration in Eqs. (4.37) and (4.38) is valid for the electric field in the x direction, the magnetic field in the y direction and normal incidence only. The S-matrix method itself is more general and could be adapted to a more general case, but we here consider only this simplified configuration. From the Maxwell equations, it follows that there is a relationship between the field amplitudes of the electric field Ω_j and the magnetic field Λ_j of the form

$$\Lambda_j^\pm = \pm \frac{1}{\sqrt{1 - k_j^2/\omega^2}} \Omega_j^\pm, \quad (4.39)$$

which allows us to write the fields in free space in terms of only the electric field amplitudes Ω_j^\pm . We can now write the electric and magnetic field amplitudes in a matrix structure as

$$\begin{pmatrix} \vec{E}_m(x, z) \\ \vec{H}_m(x, z) \end{pmatrix} = \begin{pmatrix} S_0 & S_0 \\ T_0 & -T_0 \end{pmatrix} \begin{pmatrix} \vec{\Omega}_m^+(x, z) \\ \vec{\Omega}_m^-(x, z) \end{pmatrix}, \quad (4.40)$$

where S_0 is a unit matrix, T_0 is a matrix with $\frac{1}{\sqrt{1 - k_j^2/\omega^2}}$ on the diagonal, and we have introduced the notation

$$\vec{\Omega}_m^\pm(x, z) = (\dots \Omega_{-m}^\pm e^{i(k_{-m}x \pm \beta_{-m}z)}, \dots, \Omega_0^\pm e^{\pm i\omega z}, \dots, \Omega_m^\pm e^{i(k_mx \pm \beta_m z)} \dots)^T, \quad (4.41)$$

and $\vec{E}_m(x, z)$ ($\vec{H}_m(x, z)$) contains all the space dependent field amplitudes of the electric (magnetic) field. The full electromagnetic fields in free space can be obtained by summing all the components of these vectors.

The above discussion gives a flavor of the calculation at hand. These fields can be used to match field amplitudes around the graphene sheet to find the graphene S matrix. A more complicated calculation is necessary to write down the fields inside the grating region and to find the S matrix for the grating. More details about these S-matrices can be found in appendix C. The two S-matrices are given in Eqs. (C.9) and (C.13), and they can be combined to give a final S-matrix from region 1 to region 3. This can be accomplished by rewriting the matrices in terms of transfer matrices, reshuffling the terms and multiplying the T-matrices, and finally reshuffling the answer to S-matrix form again. Following this approach, the final S-matrix from region 1 to region 3 is

$$S_{\text{tot}} = \begin{pmatrix} t_2 q_1 t_1 & r_2 + t_2 r_1 q_2 t_2 \\ r_1 + t_1 r_2 q_1 t_1 & t_1 q_2 t_2 \end{pmatrix}, \quad (4.42)$$

where we have defined $r_{1/2}$ and $t_{1/2}$ as the components of the S-matrices that can be found in Eqs. (C.9) and (C.13) of appendix C:

$$S_{\text{grating}} = \begin{pmatrix} t_1 & r_1 \\ r_1 & t_1 \end{pmatrix}, \quad (4.43)$$

$$S_{\text{graphene}} = \begin{pmatrix} t_2 & r_2 \\ r_2 & t_2 \end{pmatrix}, \quad (4.44)$$

and

$$q_1 = (S_0 - r_1 r_2)^{-1}, \quad (4.45)$$

$$q_2 = (S_0 - r_2 r_1)^{-1}. \quad (4.46)$$

Eq. (4.42) contains the final result of the S-matrix method and is a 2-by-2 block matrix where every block is an $N \times N$ matrix, with N being the number of amplitudes in the Fourier expansions. The number of modes used in the expansion sets an effective cut-off in momentum that cannot be too large, or the matrices involved become too large to handle. In practice, N is found by checking for convergence of the returned solutions as N is increased. The reflection and transmission amplitudes can be read from the final S-matrix by identifying the propagating mode. It should be noted that in general a periodic structure such as the one we consider may have many propagating modes. However, this is only the case if the wavelength of the incident light is shorter than the period of the structure and this is never the case in the structures we consider. We can thus safely ignore the possibility of grating diffraction in our subwavelength structures and only the zero mode is propagating. It is important to note that the evanescent modes inside the grating play an important role in determining the amplitude of the propagating mode.

4.3.2 Finite element method

The Finite Element Method (FEM) is a widely used method for solving partial differential equations and the fields of application include structural mechanics, fluid dynamics, and electromagnetics. The method is usually attributed to Courant [106] who used it in 1943 to study vibrations. The main idea in FEM is to subdivide the problem domain into subdomains (elements) over which basis functions are defined over single elements. These basis functions may be simple and they contain coefficients that are determined by solving a system of equations that is constructed for the particular problem being solved. The solution obtained is in general not exact, and the quality of the solution depends on how well the basis

functions can represent the exact solution as well as the amount of elements used in the subdivision of the original domain. In FEM, the original partial differential equation is transformed into a system of equations for finding the basis function coefficients. For time-independent problems, the resulting system of equations are coupled algebraic equations and time dependent problems result in a system of coupled ordinary differential equations. The main accomplishment of FEM is the reformulation of the original partial differential equation into a system of equations which has a more straightforward solution method.

In this thesis, we deal with Maxwell's equations in the frequency domain, where time is explicitly Fourier transformed, leaving us with a problem which is effectively time-independent. We thus focus on the time-independent case, which yields a system of coupled algebraic equations to solve. Depending on the problem, the equations can be linear and such a system of coupled linear equations can be represented by a matrix containing the linear coefficients and a vector containing the unknowns. Many efficient ways of solving such matrix-represented equations exist and can be employed to obtain an approximate solution to the original problem. Many different FEM softwares exist, the FEM analysis presented in this thesis has been performed with COMSOL [107].

The typical problem to be solved by FEM is the boundary value problem formulated on some domain Ω which has a boundary Γ , i.e., $\Gamma = \partial\Omega$. This can be written as a differential equation on Ω as

$$\mathcal{L}\phi = f, \quad (4.47)$$

where \mathcal{L} is a differential operator. For Eq.(4.47) to have a unique solution it has to be complemented with some boundary condition on Γ . A FEM solver contains the following basic steps:

1. Discretize the domain into elements;
2. Choose basis functions defined on the elements;
3. Create the system of equations using *either*
 - (a) the Rayleigh-Ritz variational method *or*
 - (b) the Galerkin method;
4. Solve the system of equations.

These steps can best be illustrated by an explicit example and even though the simulations performed in the rest of the thesis are on two-dimensional domains, we will here consider the one-dimensional case. We do so for

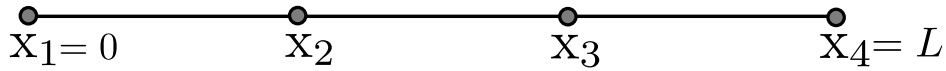


Figure 4.4: The subdivision of the original domain into three smaller elements. For simplicity we work with only a small number of elements in this example.

simplicity as higher-dimensional cases become increasingly cluttered due to the complicated node numbering schemes which tends to hide the basic structure of the method.

We consider two infinite parallel plates which are kept at different potentials, separated by a distance L in the x direction. The medium between the plates is assumed to have a constant charge distribution and the voltage in the system can be described the Poisson equation with a source:

$$-\frac{\partial^2}{\partial x^2}V(x) = \rho(x)/\epsilon, \quad (4.48)$$

$$\rho(x) = \rho_0, \quad (4.49)$$

on the domain $\Omega : x \in [0, L]$, subject to the boundary condition $V(0) = 0$ V, $V(L) = 1$ V (Dirichlet boundary conditions). For simplicity we set $L = 1$ m, $\epsilon = 1$ F/m, and $\rho_0 = 1$ C/m³ and the exact solution is

$$V(x) = \frac{(3x - x^2)}{2} [V], \quad (4.50)$$

which can be found by direct integration and use of the boundary conditions to determine the integration constants. Of course, since we can find the exact solution to this problem there is no need to use FEM to find an approximate solution. However, the strength of FEM is its ability to find approximate solutions to essentially any problem and the present problem serves as a demonstrational example where we can compare the approximate solution with the exact solution. We will now see how to find the approximate FEM solution to this problem by going step by step through the list above. In the first step, we divide the domain into three elements (subdomains), thereby creating four nodes, see Fig. 4.4. In the second step we choose the basis functions to be linear functions within the subdomains of the form

$$\tilde{V}(x) = V_i \frac{x_{i+1} - x}{x_{i+1} - x_i} + V_{i+1} \frac{x - x_i}{x_{i+1} - x_i}, \quad (4.51)$$

for $x_i < x < x_{i+1}$, $i = 1, 2, 3$, and V_i are four unknown coefficients to be found. The boundary condition immediately gives that $V_1 = 0$ and $V_4 = 1$ and the two remaining coefficients remain to be calculated. This is accomplished in the remaining two steps where we first construct a system

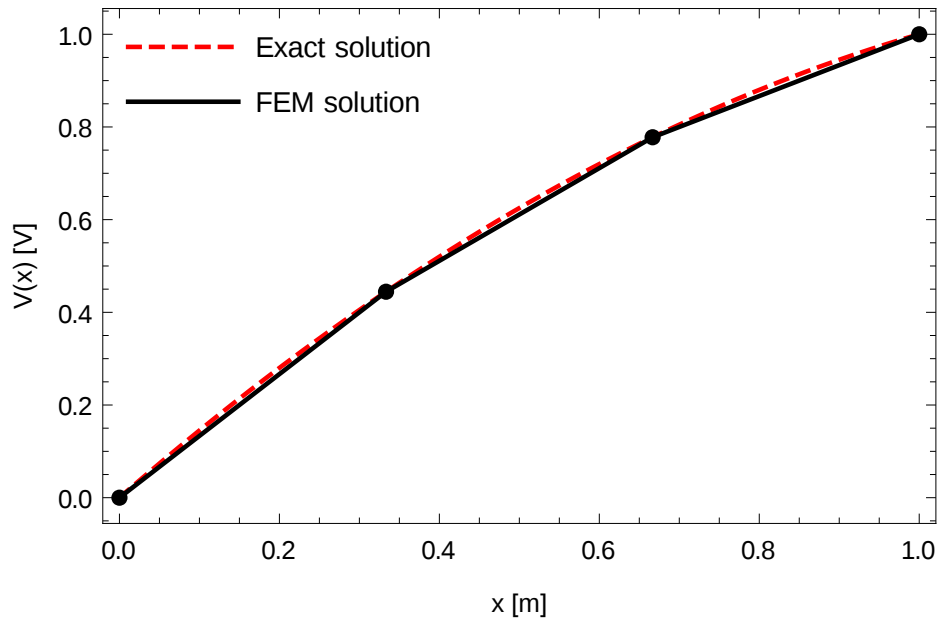


Figure 4.5: Exact solution, Eq. (4.50), (red dashed line) and approximate FEM solution (black line) to the Poisson equation in Eq. (4.48). The black dots show the points where the solution crosses between the different elements shown in Fig. 4.4.

of equations and then solve them. As seen in the list above, there is a choice to be made between the Rayleigh-Ritz method and the Galerkin method. We choose the Rayleigh-Ritz method, which is a variational method and might seem more familiar to physicists. Appendix D describes this method briefly and applies it to determine the coefficients in Eq. 4.51. The solution obtained is

$$V_1 = 0, \quad V_2 = \frac{4}{9}, \quad V_3 = \frac{7}{9}, \quad V_4 = 1, \quad (4.52)$$

where V_1 and V_4 were known already from the boundary conditions.

The solution obtained in appendix D is shown in Fig. 4.5 together with the exact solution and the two can be seen to be in good agreement. By increasing the number of elements, the FEM solution becomes closer to the the exact solution at the expense of a larger system of equations to solve. At some point it becomes cumbersome to perform the algebra explicitly like we did above and the resulting system of equations can be conveniently recast into matrix form for which effective solution methods can be used to obtain the unknown coefficients. In the present example it is obviously not necessary to use the FEM solver since we know the exact solution. However, for many problems it may be hard or impossible to find the exact solution, especially in higher dimensions and complicated domain geometries. This is where FEM shows its true strength: it can give approximate solutions for general problems in general geometries.

Floquet boundary condition for periodic structures

We now turn to a special type of boundary condition needed for simulations of non-normal incidence on periodic grating structures. The simulation domains that have been treated in this thesis are periodic grating structures which, although infinite in extension, can be simulated on a single unit cell by taking advantage of the discrete translational symmetry. This is in contrast to the simplified example above where we terminated the domain using Dirichlet boundary conditions. The problem we are interested in is electromagnetic scattering on a periodic structure, i.e., the reflection and transmission from the structure.

Fig. 4.6 shows a schematic view of the system under consideration. The middle unit cell is repeated indefinitely to the left and right, making the system extension infinite. The key to simulating this system is realizing that the solution is also periodic with the same periodicity as the underlying physical system, as well as a possible phase due to misalignment between the periodicity and the source. Mathematically this can be expressed as [108]

$$u(x + mL) = u(x)e^{-im\phi}, \quad (4.53)$$

where L is the width of the unit cell, m is an integer, and ϕ is the phase shift between two adjacent unit cells. Eq. (4.53) implies that the total function $u(x)$ is a product of a periodic function $u_p(x)$ and a phase factor as

$$u(x) = u_p(x)e^{-i\phi x/L}, \quad (4.54)$$

and can be used as a boundary condition of the form

$$u(0) = u(L)e^{-i\phi}, \quad (4.55)$$

which can be used in simulations to investigate periodic structures. This is known as a Floquet boundary condition and it is a generalization of a periodic boundary condition. Setting $\phi = 0$ in Eq. (4.55) reduces to the periodic condition.

We will now investigate some of the implications of using the Floquet boundary condition. Since the function $u_p(x)$ is periodic, it has a Fourier series expansion of the form

$$u_p(x) = \sum_{m=-\infty}^{\infty} A_m e^{ik_m x}, \quad (4.56)$$

where A_m are Fourier expansion coefficients, $k_m = 2\pi m/L$, and L is the width of the unit cell, see Fig. 4.6. Combining Eqs. (4.54) and (4.56) we

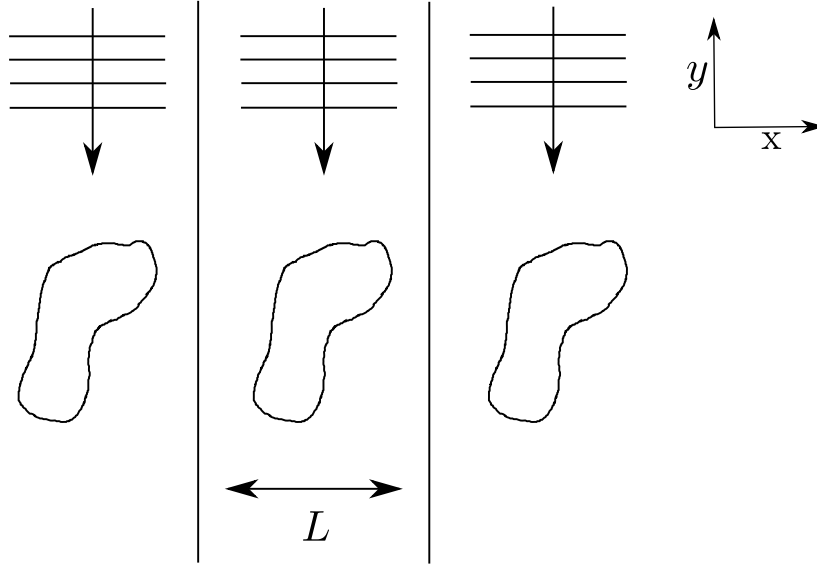


Figure 4.6: A system that is infinitely periodic in the x -direction with radiation incident from the top. The width of the unit cell is L in the x -direction. The periodicity can be generalized to two and three dimensions.

obtain

$$u(x) = \sum_{-\infty}^{\infty} A_m e^{i(k_m - \phi/L)x}, \quad (4.57)$$

which is known as Floquet's theorem. In condensed matter physics, this is known as Bloch's theorem and is used to treat band structures in crystals that exhibit periodicity [29], much like the situation we are considering here. To illustrate the use of Floquet's theorem, we consider the electromagnetic scattering depicted in Fig. 4.6, where radiation is incident from above on the infinitely periodic structure. The radiation may be incident with an angle and can be written as

$$u^0(x, y) = A e^{i(k_x^0 x + k_y^0 y)}, \quad (4.58)$$

where $k_0 = \sqrt{(k_x^0)^2 + (k_y^0)^2}$ is the propagation constant and A is a constant amplitude. The incident radiation is periodic in space with a phase shift between adjacent unit cells in the x -direction of $k_x^0 L$. The solution for the field above the structure can be written as a superposition of the incident field and the scattered field which, according to Floquet's theorem, can be written as the product of a periodic function and a phase factor as

$$u(x, y) = u^0(x, y) + u_p^{sc}(x, y) e^{ik_x^0 x}. \quad (4.59)$$

By Fourier expanding the periodic part of the scattered field this can be

written as [108]

$$u(x, y) = u^0(x, y) + \sum_{m=-\infty}^{\infty} u_{p,m}^{sc} e^{i\kappa_m x + ik_{y,m} y} e^{ik_x^0 x}, \quad (4.60)$$

where $\kappa_m = 2\pi m/L$ defines the Fourier modes. The total wave vector in the x -direction is now

$$k_{x,m} = \kappa_m + k_x^0, \quad (4.61)$$

and the wave vector in the y -direction can be determined to be

$$k_{y,m} = \begin{cases} \sqrt{(k_0)^2 - (k_{x,m})^2}, & \text{for } k_0^2 \geq k_{x,m}^2, \\ i\sqrt{(k_{x,m})^2 - (k_0)^2}, & \text{for } k_0^2 \leq k_{x,m}^2. \end{cases} \quad (4.62)$$

From Eq. (4.61), it is clear that the periodic structure can add momentum in the periodic direction and from Eq. (4.62) we see that not all of the modes can be propagating. This depends on the incidence angle, the wavelength of the incident light, and the periodicity of the grating.

The directions of the reflected propagating waves are $\varphi_m = \cos^{-1}(-k_{x,m}/k_0)$, which using Eq. (4.61) can be rewritten into

$$\varphi_m = \cos^{-1}\left(-\frac{k_x^0 + \kappa_m}{k_0}\right) = \pi - \cos^{-1}\left(\cos(\varphi_0) + \frac{m\lambda_0}{L}\right). \quad (4.63)$$

The angles in the above equations are defined from the x axis, so normal incidence as depicted in Fig. 4.6 is incident with an angle $\varphi_0 = \pi/2$.

The main insight we get from Eq. (4.63) is that the scattered field from the periodic structure consists of at least one propagating mode ($m = 0$) and several evanescent modes that decay away from the structure. For normal incidence, we can also see that in order for the grating to induce scattered propagating modes beyond the fundamental mode, the incident wavelength λ_0 has to be smaller than L . Gratings where multiple propagating modes are created are called diffraction gratings and can for instance be used to separate colors from wide spectrum light. The gratings studied in this thesis are deep-subwavelength, and thus $\lambda_0 > L$ and no propagating modes beyond the fundamental mode are created. This means that the transmitted field will propagate in the same direction as the the incident field and the reflected mode will be specularly reflected, i.e., at an angle $\pi - \varphi_0$.

This concludes our discussion of the Floquet boundary condition that was used in COMSOL to perform simulations for non-normal angles of incidence. In the S-matrix method, we only studied normal incidence and thus we only considered periodic boundary conditions. However, the

method itself is general enough to be able to handle also non-normal incidence by using the Floquet boundary condition described above.

Chapter 5

Graphene Plasmons

In this chapter, we introduce graphene plasmons and investigate their electromagnetic field configuration and propagation properties. We also discuss their subwavelength nature and the implications of this for probing graphene plasmons with electromagnetic radiation. In addition, the chapter contains a discussion of an application for graphene plasmons in sensing and discusses sensing figures of merit and electromagnetic field localization provided by the graphene plasmons. This chapter uses results and theory from the preceding chapters and refers to the relevant chapters where possible.

We end this chapter with a discussion and comparison between graphene and metals as plasmonic materials. Due to the rather different geometry of graphene and bulk metals, the resulting plasmons are rather different in nature and the governing equations are quite different. Of course, metals can be patterned and much attention has been paid in the literature to metal nanoparticles, where electromagnetic energy can be confined to very small regions. We list some advantages and disadvantages of plasmons in the different paradigms.

5.1 Graphene plasmon dispersion relation

Plasmons are collective oscillations in the electron density of metals, which have an associated electromagnetic field [1]. Since graphene contains free charge carriers, it also supports plasmons. One way to investigate graphene plasmons is to consider a graphene sheet embedded between two dielectrics. Graphene is described by its conductivity and is included in the electromagnetic problem as a boundary condition. This explains why we paid so much attention to the conductivity in chapter 3. Electromagnetic boundary conditions were also treated in chapter 4. An investiga-

tion of solutions for bound modes at the graphene interface described by the graphene conductivity gives the determining equation for longitudinal plasmons [26]:

$$1 + \frac{iq \sigma(q, \omega)}{\omega(\varepsilon_1 + \varepsilon_2)} = 0, \quad (5.1)$$

where we have assumed that $q \gg \omega$, see appendix E for details of the derivation. In the derivation, we have assumed a decaying mode profile in the z direction (perpendicular to the graphene plane), an electric field in the x - z directions and a magnetic field in the y direction. The momentum q is taken to be in the x direction, this direction is transverse to the magnetic field, so this mode is sometimes called a Transverse-Magnetic (TM) mode. It is also called a longitudinal mode where longitudinal means that the corresponding oscillation occurs in the direction of propagation. Sound waves are another example of longitudinal waves.

Graphene also supports another type of confined mode; a Transverse Electric (TE) mode [109]. Such bound modes cannot exist at metal interfaces [1] and the fact that they can exist in graphene is due to the unusual behavior of the charge carriers in graphene [109]. In this thesis we focus on the TM plasmons, as they exhibit a larger confinement than the TE modes which are only weakly confined [4].

The longitudinal (TM) plasmon dispersion can be obtained analytically in the zero-temperature and long-wavelength limit, i.e., $q \rightarrow 0$. By considering the (clean) local conductivity, Eq. (3.62), in the low energy limit, $\omega \ll E_F$, we obtain $\sigma(\omega) = ie^2 E_F / (\pi\omega)$. Inserting this in the nonretarded dispersion equation, Eq. (5.1), we obtain the long-wavelength plasmon dispersion

$$\hbar\omega = \sqrt{\frac{4\alpha\hbar c E_F q}{(\varepsilon_1 + \varepsilon_2)}}, \quad (5.2)$$

where $\alpha = e^2 / (4\pi c \varepsilon_0 \hbar) \approx 1/137$ and we have briefly reinserted \hbar and c for clarity. The plasmon energy depends on the square root of the wave vector, which is in stark contrast to the linear dispersion of photons and, as a consequence, plasmons with different energies propagate with different velocities. It also means that the plasmon group velocity and the phase velocity never coincide, but are related by $v_g = v_{ph}/2$.

The fact that the plasmon energy depends on the Fermi energy makes it clear that it is possible to affect graphene plasmons by changing the doping. As discussed in chapter 2, the doping level in graphene can be controlled electrostatically and through this the plasmon energy can be controlled. Typically, graphene plasmons are in the terahertz to mid-

infrared regime [4]. From the dispersion relation it is also evident that the plasmon energy depends on the dielectric environment surrounding the graphene sheet. From this we may conclude that there is a possibility to utilize graphene plasmons to sense the local environment. We investigate this further in section 5.4.

The \sqrt{q} -behavior obtained in Eq. (5.2) is also obtained for plasmons in 2DEGs, in fact it is a consequence of the two-dimensionality [4]. By using that $E_F = \sqrt{\pi n}$ we can see that the graphene plasmon energy depends on $n^{1/4}$, in contrast to the 2DEG dependence of $n^{1/2}$. As a side note, it is amusing to note that water waves obey the same dispersion relation as long-wavelength graphene plasmons. Deep-water waves obey the dispersion relation $\omega = \sqrt{gq}$ [110], where $g \approx 10 \text{ m/s}^2$ is the gravitational constant on earth (the corresponding ‘‘acceleration’’ for graphene plasmons is on the order of 10^{21} m/s^2).

We will now use the plasmon dispersion and show that graphene plasmons indeed facilitate a strong electromagnetic field localization. By comparing the wavelength of free-space electromagnetic radiation with the plasmon wavelength, we can get an expression for the wavelength of both modes. From the dispersion relations we obtain the wavelength ($\lambda = 2\pi/q$) for a given frequency as

$$\lambda_0 = \frac{2\pi c}{\omega}, \quad (5.3)$$

$$\lambda_{\text{pl}} = \frac{4\pi\alpha c E_F}{\hbar\omega^2}, \quad (5.4)$$

where λ_0 is the free-space wavelength of electromagnetic radiation, λ_{pl} is the plasmon wavelength, and we have taken the dielectric environment to be vacuum, i.e., $\varepsilon_1 = \varepsilon_2 = 1$. From this we can easily compute the ratio between the free-space wavelength and the plasmon wavelength as

$$\frac{\lambda_0}{\lambda_{\text{pl}}} = \frac{\hbar\omega}{2\alpha E_F}, \quad (5.5)$$

which is plotted as the red dashed line in the right panel of Fig. 5.1. The ratio expressed in Eq. (5.5) is valid in the small-frequency ($\hbar\omega \ll E_F$) limit and should strictly speaking not be extended beyond $\hbar\omega = E_F$. However, solving the dispersion relation using the nonlocal conductivity numerically, we can obtain the same ratio but valid for all frequencies. This is shown as the blue solid line in Fig. 5.1 and for small frequencies it agrees with the low-energy expansion expression obtained above. Both the local and nonlocal ratio in the right panel of Fig. 5.1 tend to zero as $\omega \rightarrow 0$, which signals that plasmon wavelength becomes much larger

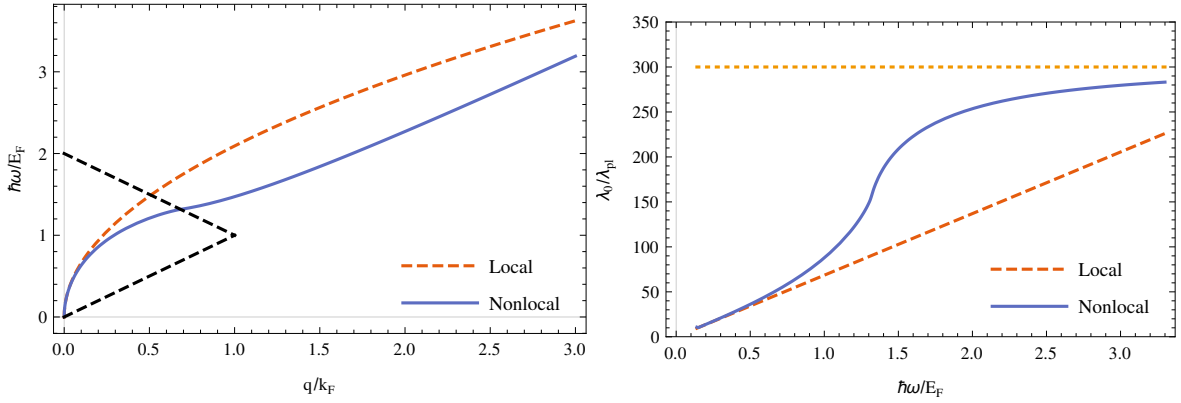


Figure 5.1: Left: The local dispersion relation in Eq. (5.2) (red dashed line) and full nonlocal dispersion obtained by solving the dispersion relation, Eq. (5.1), with the zero-temperature nonlocal conductivity (blue solid line). Right: The ratio between the (free) electromagnetic wavelength λ_0 and the plasmon wavelength at the same frequency. The ratio is shown using the local approximation (red dashed line) in Eq. (5.5) and using the numerical result for the nonlocal conductivity and numerically solving Eq. (5.1) (blue solid line). The yellow dotted line shows the maximum localization of 300 which the nonlocal solution tends to in the large frequency limit. This value is set by the difference between the electromagnetic velocity and the Fermi velocity of the linear-dispersion charge carriers in graphene, i.e. $c/v_F = 300$.

than the wavelength of electromagnetic radiation in this limit. This is an artifact of the non-retarded approximation ($q \gg \omega$) which was made to arrive at Eq. (5.1) and it is only relevant in the very small frequency limit. Should the fully retarded equation be used, the ratio would tend to unity in the small frequency limit. For energies larger than $0.1E_F$, i.e., the energies relevant for graphene plasmonics, this correction has no effect on the results and can safely be neglected.

From Fig. 5.1, one might conclude that graphene plasmons facilitate a localization up to a factor of 300 of the incident radiation. However, this is arrived at by assuming no losses (clean graphene at $T = 0$ K) and it turns out that under more realistic conditions, plasmons with large confinement are associated with larger losses. We turn to an investigation of plasmon losses in graphene in the next section.

5.2 Graphene plasmon propagation and damping

The results for the dispersion in the previous section are only valid in the clean graphene case and at zero temperature. For nonzero temperatures and/or damping mechanisms added, the graphene conductivity acquires a real part in addition to its imaginary part. The plasmon dispersion equation, Eq. (5.1), then becomes two equations, the real part and the imaginary part, and cannot be solved in general with only one variable. To accommodate this, we let $q = q_1 + iq_2$ be a complex variable and we

obtain q_1 and q_2 by solving both the real and imaginary parts of the dispersion equation. Since the conductivity is a rather complicated function of q , finding the solution could in general be quite hard for the coupled equations. To simplify the solution procedure we realize that we are mostly interested in weakly damped plasmons, i.e., $q_2/q_1 \ll 1$, and we may expand the dispersion equation in this small parameter and keeping only the lowest-order term we obtain

$$1 = \frac{q_1 \sigma_2(q_1, \omega)}{\omega(\varepsilon_1 + \varepsilon_2)}, \quad (5.6)$$

$$\frac{q_2}{q_1} = \frac{\sigma_1(q_1, \omega)}{\partial_{q_1}(q_1 \sigma_2(q_1, \omega))}. \quad (5.7)$$

We note that Eq. (5.6) is the same equation as we would obtain by taking Eq. (5.1) directly and assuming no losses, i.e., neglecting $\sigma_1(q, \omega)$. By solving Eq. (5.6), we may use the solution to evaluate the expression in Eq. (5.7) to obtain the value of q_2 , i.e., the losses. The value of q_2 can be seen to be proportional to σ_1 , i.e., the real part of the conductivity. In effect, a completely imaginary conductivity yields zero plasmon losses.

An investigation of the real part of the clean graphene-conductivity shows that there are no losses at zero temperature in a certain region in q - ω space. This is shown in the top left panel of Fig. 5.2, where the real part conductivity is shown in a large region of q - ω space. There is a triangle where $\sigma_1(q, \omega) = 0$ and the graphene plasmons experience no losses in this region. The regions where the conductivity becomes non-zero are associated with interband and intraband excitation of electron-hole pairs. This is the only loss channel that exists in clean graphene. Inside the triangle, these transitions cannot take place due to Pauli blocking.

The top right panel of Fig. 5.2 shows the real conductivity for graphene at $T = 300$ K for $\Gamma = 0.012$ eV ($\tau = 50$ fs). The Γ is added using the Mermin relaxation time approximation, see section 3.4. The previously lossless triangle now has a non-zero conductivity due to the electron relaxation as well as non-zero temperature. The temperature effect arises due to thermal smearing of the electron distribution which makes the Pauli blocking not perfect close to the triangle edges. The electron relaxation time affects the entire region inside the triangle.

The plasmon wavelength is given by $\lambda_{\text{pl}} = 2\pi/q_1$ and the propagation distance is given by $L_p = 1/(2q_2)$ [4]. This definition takes the rather strict view that the plasmon is considered decayed when the intensity of the plasmon has dropped to $e^{-1} \approx 0.37$ of its initial value.

A convenient way to quantify the propagation of plasmons is to calculate

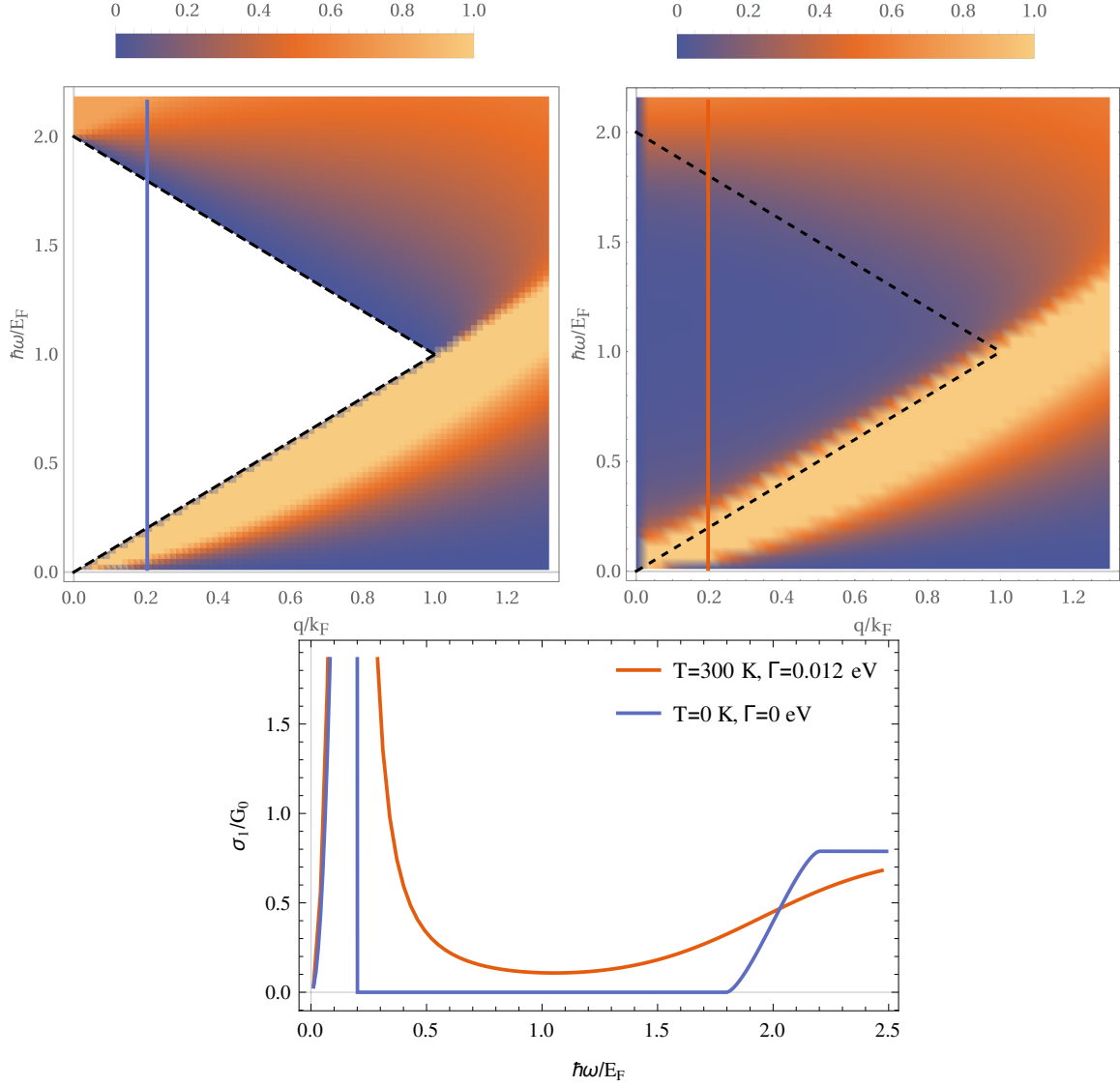


Figure 5.2: Real part of the graphene conductivity, $\sigma_1(q, \omega)$ at $T = 0$ and $\Gamma = 0$ (top left panel) and at $T = 300$ K $\Gamma = 0.012$ eV (top right panel). The relaxation time is included using the Mermin relaxation time approximation. The bottom panel shows a cut of the real part at $q/k_F = 0.2$ of the top panels (shown as vertical lines in the top panels). All results are shown for $E_F = 0.2$ eV. The white triangle in the top left panel shows the region where the real conductivity is identically zero for clean graphene at $T = 0$ K. This triangle is highlighted with black dashed lines that are also superposed on the top right panel where the real part is no longer zero. The non-zero real part will translate into non-zero plasmon losses, see Eq. (5.7).

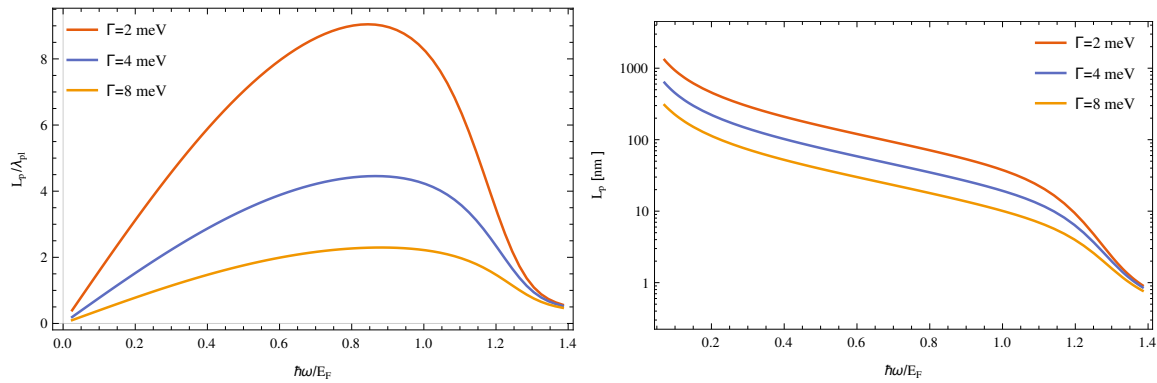


Figure 5.3: The propagation length for graphene plasmons in units of the plasmon wavelength (left) and in log-scale of nanometers (right). The different lines correspond to the different inverse relaxation times shown in the legend of the figures. For both figures, $E_F = 0.4$ eV and $T = 300$ K. Low-energy plasmons propagate rather far in terms of nanometers but very few wavelengths, meaning that the enhancement in propagation is an effect of the plasmon wavelength becoming larger.

the propagation distance in units of the plasmon wavelength, i.e. L_p/λ_p . By studying the definitions of q_1 and q_2 above, this ratio can be expressed as

$$\frac{L_p}{\lambda_p} = \frac{q_1}{4\pi q_2}, \quad (5.8)$$

i.e., the inverse of the small expansion parameter q_2/q_1 used above. From the ratio in Eq. (5.8), we see that (as expected) undamped plasmons have an infinite propagation length. Below, we investigate the propagation distances, as quantified by the ratio in Eq. (5.8), for realistic relaxation times. It should be noted that this is done here using the Mermin relaxation time approximation.

Fig. 5.3 shows the propagation length for different relaxation times and at room temperature. The left panel shows the propagation length in units of the plasmon wavelength and the right panel shows the propagation length units of nanometers (log-scale). The typical number of oscillations obtained using the Mermin relaxation time approximation agrees qualitatively with the number of plasmon oscillations found in experiments [24, 66]. However, this is only indicative since the relaxation time approximation is a phenomenological model.

The left panel of Fig. 5.3 shows that q_1/q_2 has a maximum around $\hbar\omega = E_F$ and experiences a sharp drop for larger frequencies. This drop is due to interband transitions that rapidly damps out the plasmon mode. We conclude that the maximum frequency of plasmons under realistic conditions are only slightly larger than E_F , larger frequencies are completely damped. From Fig. 5.1 we see that this limits the field localization to around $\alpha^{-1} \approx 137$ [4]. This is still a large localization factor, but not as

large as 300 that was achieved when losses were neglected in section 5.1.

5.3 Coupling electromagnetic radiation to graphene plasmons

It was shown in Fig. 5.1 that the plasmon wavelength can be much smaller than the electromagnetic free-space wavelength at the same frequency. As a consequence, there is a large wavelength mismatch between electromagnetic radiation and plasmons of the same frequency, making excitation of plasmons with radiation impossible on flat surfaces [1]. This is true also for plasmons in metals and several ways to overcome this problem have been developed over the years [1]. Examples are prism coupling [111, 112], grating coupling [10], and near-field coupling [113]. Plasmons can also be probed using other methods, such as electron energy loss spectroscopy [114, 115]. From now on we focus only on electromagnetic coupling to plasmons.

For graphene plasmons, patterning the graphene into microribbon arrays [57, 116] was an early method used for coupling. The microribbon array acts as a grating and supplies the coupling between incident radiation and graphene plasmons. The plasmons can then be probed by illuminating the array with electromagnetic radiation and monitoring the transmission or reflection. Using microribbon arrays, the authors in Ref. [116] were able to demonstrate the gate-tunability of graphene plasmons.

Another route to couple to graphene plasmons is by using nanotip illumination [24, 25, 117]. This creates an evanescent field surrounding the nanotip, placed in close proximity to the graphene sample, through which electromagnetic radiation couples to the plasmons. By now, this method has been used in many works to study various aspects of graphene plasmons. Examples are coupling to localized states [118], studies of graphene edge plasmons [119, 120], nonlocal effects [102], and plasmon-induced photocurrent [121]. In addition, illumination of metal nanoantennas, deposited on top of graphene, with a laser can be used to excite plasmons [122].

Subwavelength patterning of the environment surrounding the graphene sample has also been used to couple electromagnetic radiation to graphene plasmons. Periodic arrays of metal patterning [40, 123] as well as dielectric gratings [124, 125] have been investigated. In this thesis, we focus on dielectric gratings in proximity to a graphene sheet in order to facilitate the necessary coupling between the incident radiation and the graphene plasmons. A grating together with a graphene sheet is depicted in Fig. 4.2

and methods for solving the electromagnetic scattering problem in such geometries were treated in section 4.3.

5.4 Refractive index sensing using graphene plasmons

One application of plasmons is for label-free sensing of the local environment [17], which can be used for drug discovery, food safety, and environmental monitoring [16]. Many biomolecules are active in the mid-infrared which makes graphene plasmons ideal for sensing such molecules. Graphene plasmons are found to be in this part of the spectrum and as we have also seen, they are tunable by means of external gating. This can be used for taking spectroscopic fingerprints of biomolecules, something already demonstrated by Rodrigo *et al* [38]. Recently, also double layer graphene has been used to further enhance the sensing capabilities of graphene plasmons [126].

Plasmonic sensors work by probing some aspect of plasmons in the sensor, such as the plasmon resonance frequency, and monitor this as the environment changes [16, 17]. The change in the environment can then be inferred by reading out the change in the plasmonic signal. The benefit of using plasmons for this is that they can dramatically increase the electromagnetic field strength in the region surrounding the sensor, which increases the response to small changes in the environment [1]. However, there are limitations that arise from plasmon losses, which degrade the sensitivity and need to be considered. In the next section, we address the question: “how good is sensing using graphene plasmons and how to quantify this?”

5.4.1 Figures of merit for refractive index sensing

To investigate sensing performance, it is convenient to introduce a Figure of Merit (FOM) that captures aspect(s) of the sensing scheme. We will consider the response of graphene plasmons to changes in the dielectric environment. The sensor setup we consider consists of a graphene sheet together with a dielectric grating to provide coupling between electromagnetic radiation and the plasmons. This setup can be probed by incident radiation and the transmission and reflection can be measured. The transmission has a dip as the frequency sweeps across the sensor and the position of this resonance constitutes the sensing signal. Now, this dip has a finite width due to the fact that the plasmon experiences losses as well as being coupled to radiation. The width of the peak can mask small

shifts in the plasmon frequency and in practice limits the ability to detect small variations in the dielectric environment, i.e., it limits the sensitivity of the proposed sensing scheme.

For the sensing scheme described above, a commonly used FOM is the frequency shift of the plasmon resonance due to a small refractive index change, divided by the resonance width [127]:

$$\text{FOM}_{\text{bulk}} = \frac{m}{\Gamma_p}, \quad (5.9)$$

$$m = \frac{\partial\omega_p}{\partial n} \quad (5.10)$$

where ω_p is the plasmon frequency, Γ_p is the width of the plasmon resonance, and n denotes refractive index. The quantity m expresses the change in resonance frequency per refractive index unit. We refer to the FOM in Eq. (5.9) as the bulk FOM for reasons that will become clear below.

The bulk FOM lacks any notion of thickness of the medium experiencing the refractive index change. This is expected to be a good measure if the entire field localized by the plasmon is covered with the medium to be sensed. However, this might not be the case when thin layers of biomolecules are investigated. To address this, a thickness dependent FOM can be introduced [128, 129]

$$\text{FOM} = \frac{m}{\Gamma_p}, \quad (5.11)$$

$$\frac{\partial\omega_p}{\partial n} = m \left(1 - e^{-2t/L_d}\right), \quad (5.12)$$

which is nothing but a redefinition of the quantity m . The quantity L_d is the decay length of the plasmons and quantifies how far from the graphene sheet the fields of the plasmon extend. In the case where the thickness $t \gg L_d$, this reduces to the bulk FOM defined above. By introducing the thickness in the FOM, it is possible to study the difference between having the sensor completely and partially immersed in the dielectric medium to be sensed. The sensing is more effective the more the plasmon's electromagnetic field is covered, but since graphene plasmons are confined close to the graphene sheet, already thin layers of sensing medium completely cover the graphene plasmon. With the thickness added to the modeling of the plasmon frequency shift, it becomes possible to also use graphene plasmons to monitor thicknesses of thin layers of biomolecules with a known refractive index.

For an investigation of refractive index sensing using graphene plasmons

quantified by the above FOMs, we refer to Paper II.

5.5 Comparison between graphene plasmons and plasmons in metals

This section is devoted to a comparison between graphene plasmons and plasmons in metals. Metal plasmonics is a vast subject and this section does not give an overview of the entire field. Rather, focus is on aspects of the physical differences — and similarities — of plasmons in the two cases. In metal plasmonics, there are several possible geometries to be compared with. The two cases that are treated here are metal-dielectric interface plasmons and plasmons in small metal nanoparticles.

The similarity between plasmons in metals and plasmons in graphene, is that they both arise as solutions to Maxwell's equations around the conductor in question. The presence of conduction electrons modifies the electromagnetic field solutions, giving rise to the hybrid nature of plasmons. A flat metal surface is the metal geometry that most resembles the graphene plasmons that have been considered in this thesis. These plasmon modes can propagate along the interface between the metal and the dielectric and we treat this case below in section 5.5.1.

It turns out that interface plasmons in metal-dielectric interfaces are quite different from graphene plasmons. Perhaps the most striking difference is that metal interface plasmons exhibit much less localization, i.e., the wavelength of the interface plasmons is close to the electromagnetic wavelength for the same frequency. This is in large contrast to graphene plasmons where the localization can be on the order of 100. To study plasmons with more comparable localization properties, section 5.5.2 treats spherical nanoparticles which support localized (non-propagating) plasmon modes which exhibit large field localization comparable with graphene plasmons. Section 5.5.3 contains a summary of the metal plasmon properties and a comparison with graphene plasmons.

5.5.1 Metal-dielectric interface plasmons

By performing a similar calculation as was done for the graphene plasmon dispersion relation in appendix E, it is possible to arrive at the corresponding plasmon dispersion equation for the metal-dielectric interface TM plasmons [1]:

$$q = \frac{\omega}{c} \sqrt{\frac{\varepsilon_1 \varepsilon_2}{\varepsilon_1 + \varepsilon_2}}. \quad (5.13)$$

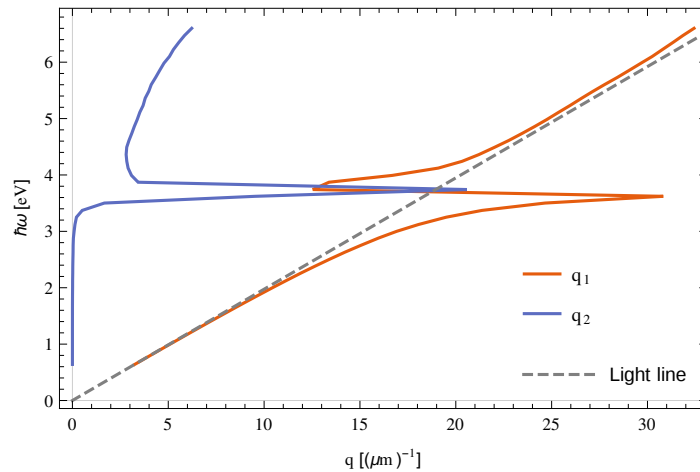


Figure 5.4: Dispersion relation for metal-dielectric interface plasmons. The figure corresponds to a silver-air interface with experimental data for the dielectric function of silver from Ref. [130]. The red curve corresponds to the real part of the wave-vector and the blue curve is the imaginary part, i.e., $q = q_1 + iq_2$. The onset of interband transitions slightly below 4 eV can be seen to heavily reduce the propagation length of the metal interface plasmons.

The material parameters of importance are the dielectric constants of the two materials above and below the interface. Setting the dielectric to be air ($\epsilon_1 = 1$) and taking the metal to be silver we get the results shown in Fig. 5.4. The experimental data for the dielectric function of silver is from Ref. [130], obtained at [131]. It turns out that TE plasmons cannot exist at metal interfaces [1], in contrast with their existence at a graphene interface [109].

From the solution to Eq. (5.13), it is easy to compute some derived properties such as the propagation length in units of the plasmon wavelength, defined in Eq. (5.8), as well as the wave localization provided by the plasmons in silver. These quantities are shown in Fig. 5.5; these modes have properties that are quite distinct from graphene plasmons. At low energies, the metal interface plasmons propagate very far, on the order of 10^4 plasmon wavelengths as shown in the top panel. In actual distances this can be up to millimeters, this is indeed found in experiments on low-energy plasmons in silver [15]. Such a long propagation length is possible due to the poor confinement at these frequencies. The bottom panel shows the localization factor and at low frequencies, the plasmon wavelength approaches the free space electromagnetic wavelength. At these frequencies the plasmon acquires a more light-like nature and is essentially a grazing incidence light beam [1].

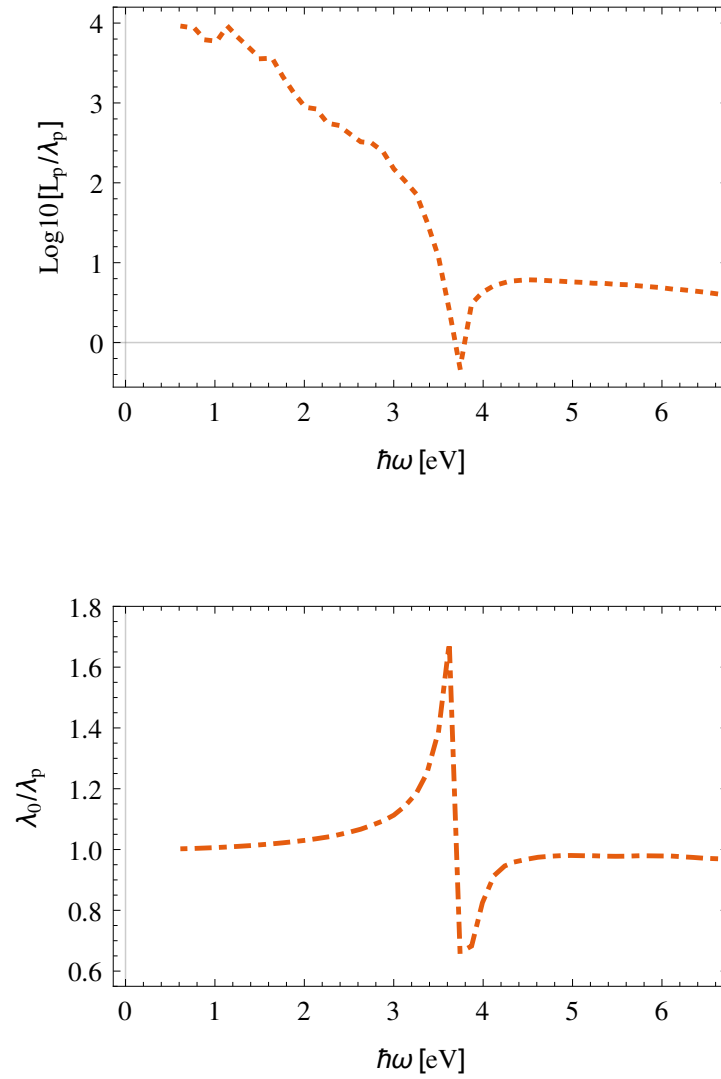


Figure 5.5: Calculated properties for plasmon in a silver-air interface obtained from the solution shown in Fig. 5.4. Top: Propagation length for surface plasmons in silver. The propagation length (in units of the plasmon wavelength) for low-energy surface plasmons can be seen to approach 10^4 . Bottom: Localization factor for silver plasmons. The most confined surface plasmons in silver are localized by a factor 1.8 at the expense of becoming essentially completely damped (see top panel for the same frequency). This damping occurs due to the onset of interband transitions which is also visible in Fig. 5.4.

5.5.2 Localized surface plasmons in metal nanoparticles

The study of localized resonances in metal nanoparticles was studied a long time ago by Mie [132], who essentially solved the electromagnetic scattering problem for metal particles. The problem with this solution is that it is expressed as infinite sums which are difficult to gain insight from. So even though Mie theory has a vast predictive power in the sense that any scattering can be calculated on a computer that evaluates the sum to arbitrary precision, it is of interest to develop simpler models of perhaps limited validity that can allow for more insight due to its simpler structure.

One such simplification arises in the limit of a small sphere of radius a , where $a \ll \lambda$, i.e., the radius of the sphere is much smaller than the incident wavelength; this limit is often referred to as Rayleigh scattering. The problem can then be treated electrostatically and the solution for the electric field is [1]

$$\vec{E} = \begin{cases} \frac{3\varepsilon_2}{\varepsilon(\omega) + 2\varepsilon_2} \vec{E}_0, & r < a, \\ \vec{E}_0 + \frac{3\vec{n}(\vec{n} \cdot \vec{p}) - \vec{p}}{4\pi\varepsilon_0\varepsilon_2} \frac{1}{r^3}, & r > a, \end{cases} \quad (5.14)$$

$$\vec{p} = 4\pi\varepsilon_0\varepsilon_2 a^3 \frac{\varepsilon(\omega) - \varepsilon_2}{\varepsilon(\omega) + 2\varepsilon_2} \vec{E}_0, \quad (5.15)$$

where $\varepsilon(\omega)$ is the dielectric function for the metal in the sphere, ε_2 is the dielectric constant of the surrounding medium, \vec{E}_0 is the incident electric field, and \vec{p} is the dipole moment of the sphere. Note the appearance of the factor $(\varepsilon(\omega) + 2\varepsilon_2)^{-1}$ which gives rise to an enhancement of the fields when $\text{Re}[\varepsilon(\omega)] = -2\varepsilon_2$. This is called the Frölich condition and the mode associated with this is called the dipole surface plasmon [1]. A general term for resonances in metal nanoparticles is Localized Surface Plasmon Resonances (LSPRs). For a small silver sphere in air ($\varepsilon_2 = 1$), the dipole resonance condition occurs at $\hbar\omega = 3.5$ eV ($\lambda = 354$ nm), using data from [130].

Fig. 5.6 shows the electric field strength, Eq. (5.14), in units of the incident field strength (in the static approximation) for a small silver sphere on resonance at $\lambda = 354$ nm. The incident field is polarized in the z direction and the field is enhanced by the presence of the small metal sphere and reaches an enhancement of 15 on the top and bottom of the sphere. The magnitude of the field enhancement is set by the imaginary part of the dielectric function, which provides the limiting value for $(\varepsilon(\omega) + 2\varepsilon_2)^{-1}$ when the resonance condition is met. A (hypothetical) lossless dielectric material would give an infinite field enhancement exactly on resonance.

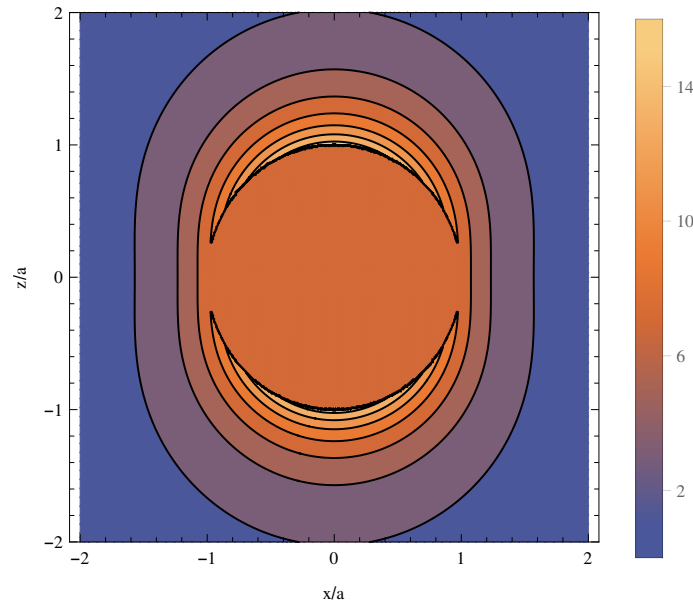


Figure 5.6: Electromagnetic field enhancement $|E|/|E_0|$ from Eq. (5.14) for a small silver sphere. The polarization of the initial electric field is along the z axis and the figure shows a cut at the $y = 0$ plane which cuts through the center of the sphere. The material properties for silver, obtained from Ref. [130], play an important role in determining the resonance frequency as well as the field enhancement. This is set by the ratio between the real and imaginary parts of the dielectric function. The figure shows the field configuration on resonance at 3.5 eV ($\lambda = 354$ nm). As long as the sphere is substantially smaller than this wavelength, the Rayleigh approximation used to obtain this figure is valid.

The conclusion is that also metal nanoparticles have the ability to confine light, similar to graphene plasmons.

The above treatment was the simplest case of scattering on a nanoparticle. In the more general case where the size of the sphere approaches the incident wavelength there are more modes appearing than just the dipole mode. A treatment of such modes requires more sophisticated approximations or use of full Mie theory.

Finally, we mention that in terms of enhancement of the electromagnetic field there is another method that can be used and that is the so called lightning-rod effect [12]. This is the enhancement of electromagnetic fields around sharp tips and edges of metal structures. This can be used to further enhance the field around a metal sphere by placing it close to a sharp corner of another metal object. One such implementation is called a bow-tie nanonantenna where gold bow ties can enhance the field more than 30-fold [133].

	Propagation	Confinement	Tunable	Frequency
Graphene plasmons	short	strong	yes	mid-infrared
Interface plasmons	long	weak	no	near infrared - visible
LSPR	-	medium	no	visible - UV

Table 5.1: Comparison between properties of graphene plasmons, metal interface plasmons, and localized surface plasmon resonances (LSPRs).

5.5.3 Summary of graphene versus metals for plasmonics

Table 5.1 provides a summary of the plasmon properties that were treated earlier in this section. This summary highlights the fact that graphene plasmons are different from plasmons in metals in that they exhibit a very strong confinement and as a result, they do not propagate very far. In addition, the frequency range for graphene plasmons is in the mid-infrared, whereas metal plasmonics is usually done at larger frequencies.

Metal plasmons can provide either very long propagation length (interface plasmons) or a rather large field enhancement (LSPR), but not both at once. Perhaps one of the most important advantages of graphene plasmons is that they are tunable. This opens up possibilities for tunable photonic devices, in the mid-infrared, that can be very compact since the graphene plasmon is very small in wavelength.

Chapter 6

Overview of Appended Publications

This thesis is based on the work presented in Papers I-V, appended at the end of the thesis. This chapter provides a brief description of the papers as well as a summary of the main results.

6.1 Paper I

In this publication, we investigated the nonlocal properties of graphene plasmons and compared and contrasted them with graphene plasmons in the local approximation. To this end, we calculated the graphene conductivity, using linear response theory, for both the nonlocal and local cases and solved the plasmon dispersion equation for them both. Doing so, we computed the plasmon dispersion relations and we found, as expected, that the local approximation is rather accurate for small q/k_F , while for larger q/k_F the more accurate full nonlocal dispersion starts showing significant deviations from the local one. We showed that this difference occurs over a large range of temperatures, from zero temperature up to $T/T_F = 1$, and that larger temperatures tend to make the local approximation agree slightly better with the nonlocal dispersion.

In addition, we studied the optical response of graphene plasmons in a nanostructured dielectric environment (subwavelength grating). The focus was on comparing the optical responses for graphene plasmons in the local and nonlocal models. The main finding was that below $T/T_F = 0.15$, the reflection, transmission, and absorption as well as the width of the resonance features differed significantly between the two cases. Above $T/T_F = 0.15$, the two cases gave rather similar results and the main difference was then in the frequency shift from the difference in the plasmon dispersion. It should be noted that $T/T_F = 0.15$ can easily extend several hundred kelvin above room temperature for realistic doping levels. This

means that nonlocal effects can be of importance to correctly capture the optical properties of graphene plasmons at room temperature.

6.2 Paper II

In this paper, we applied graphene plasmons for sensing purposes as well as quantified the sensing ability of the graphene plasmons using standard figures of merit (FOMs). In our calculations we included the effects of temperature, nonlocality, and also a scattering time that affects the electrons as they propagate in the lattice. The scattering time was included phenomenologically in a number conserving Mermin relaxation time.

Our calculations showed that for thick layers of sensing material close to the sensor, the FOM was 11. This is a rather good number although larger FoMs have been achieved in the literature. However, the main strength of our sensor comes from the extreme confinement of the graphene plasmons, which creates a high sensitivity very close — on the order of 10 nm — to the graphene surface. Together with the tunability of the graphene plasmons, this constitutes an attractive platform for taking spectroscopic fingerprints of vibrational modes in biomolecules. Thus allowing for selective sensing of very thin layers of biomolecules using our proposed sensor setup.

6.3 Paper III

Here, we studied a low density of adatoms coupled to the graphene lattice by tunneling. The tunnel coupling as well as the energy level of the adatoms were chosen to match those of hydrogen atoms and we extracted these parameters from DFT studies. Using this model, we calculated the conductivity within linear response and observed that the conductivity could change significantly depending on the adatom density as well as the position of the adatom energy level with respect to the Fermi energy.

Furthermore, we used the conductivity to solve the plasmon dispersion equation and investigated the graphene plasmon properties. In particular we studied the plasmon dispersion, the plasmon propagation length, and the plasmon damping induced by the adatoms. We found that the plasmon dispersion could be changed significantly even for a small density of adatoms and we observed a level splitting between the plasmons and the adatom energy level. The level splitting produced two distinct plasmon branches, one high energy branch and one low energy branch. The high

energy branch was damped by the presence of the adatoms and obtained a smaller propagation distance while the low energy branch was much less affected.

The adatom influence on the graphene plasmons occur for rather small densities of adatoms and this effect can therefore be used for sensing purposes. We showed in the paper how the plasmon width and frequency is affected by the impurities. For sensing, a grating setup similar to the ones in Papers I and II could be used in order to couple to the plasmons and read out these properties.

6.4 Paper IV

In Paper IV, we investigated impurities in graphene in a self-consistent model which fully included nonlocal effects. The calculations showed that an impurity band emerges in the density of states and the energy position of this band depends on the impurity density and strength of the impurities. These are free parameters in our model and we investigated the results for different parameter values, finding that the impurity band always exists and can result in a substantial real part in the conductivity below $2E_F$. We also found that the plasmons are very sensitive to the presence of the impurity band, especially when the impurity band has the same energy as the plasmons. Since the position of the impurity band depends on the strength of the impurities as well as the density of impurities, this implies that the damping of graphene plasmons can depend strongly on the type of impurities in graphene.

Furthermore, we compared our nonlocal self-consistent impurity model with the commonly used Mermin relaxation time model, finding rather large differences. This highlights that there may be a need for more complex models of impurities, such as the one considered in this paper, than what is normally used in the literature. However, further studies, both experimental and theoretical, are needed to further quantify the impurities normally occurring in graphene in order to deduce the proper model and parameters for impurity-induced plasmon damping.

6.5 Paper V

This publication contains an investigation of graphene plasmons in non-equilibrium graphene. We considered graphene to be biased with a DC voltage to produce an in-plane current in the graphene sample. We studied

the resulting effects on the graphene plasmons by calculating the graphene conductivity in the non-equilibrium graphene. We found asymmetries in the plasmon dispersion and plasmons propagating parallel (anti-parallel) with the current obtained an enhanced (decreased) propagation length. We also discussed how this effect can be measured in electromagnetic scattering experiments in a dielectric grating environment. The ability to control the plasmon propagation using a DC current could potentially be used to create miniaturized photonic devices such as optical modulators.

Moreover, we showed how the increased propagation length leads to narrower linewidths in the electromagnetic scattering signals. This can potentially lead to enhanced sensitivity for graphene plasmon-based sensors like the one considered in Paper II, since narrow linewidths increase the sensing figure of merit.

Chapter 7

Summary

In this thesis we treated plasmons in graphene starting from a microscopic Hamiltonian for the low-energy electrons in graphene. This Hamiltonian has been used pervasively in the literature and provides a solid foundation in which calculations are manageable and are not completely performed in large computer simulations. From the microscopic Hamiltonian, we derived a macroscopic property, the graphene conductivity, which can be used as input to Maxwell's equations to investigate electromagnetic modes. To perform the linear response calculation, we used a general Keldysh Green's function formalism which in addition to being useful in equilibrium, is also able to handle perturbations of non-equilibrium states. The price to pay is the addition of new Green's functions that need to be handled and this is done using a 2-by-2 matrix structure in Keldysh space.

When the linear response in terms of Keldysh Green's functions was done, we had arrived at general expressions for the polarizability of graphene in terms of Green's functions and self energies. The self energies are one of the strengths of the Green's functions method; it is possible to include additions to the bare graphene Hamiltonian and formulate a perturbation series in terms of a self energy. The self energy can be calculated for various additions to the bare graphene Hamiltonian (impurities etc.) and can then simply be included in the calculation of the graphene conductivity. It can be noted that in the clean-graphene case, we arrived — as we must — to the same expression for the polarizability as previous authors.

Armed with the conductivity, we were in a position to investigate the plasmon mode surrounding graphene sheets. These modes turn out to be deeply subwavelength and special care must be taken to interact with plasmons using electromagnetic radiation. In anticipation of the required nanopatterning, we spent some time treating Maxwell's equation in sub-wavelength patterned environments and, in particular, we studied two different solution methods to the electromagnetic scattering problem in

such cases; the S-matrix method and FEM analysis.

Finally, we arrived at a treatment of graphene plasmons and started out by studying the graphene dispersion equation and a treatment of losses in graphene plasmons. Losses turn out to have a considerable effect on the graphene plasmons and limits the field localization to values around $\alpha^{-1} \approx 137$ for realistic values of damping in graphene. In this thesis, we have studied graphene plasmons with nonlocal effects included and for frequencies comparable with E_F , we saw that the dispersion relation in the less accurate local approximation deviates considerably from the nonlocal dispersion relation. Also, we observed that the presence of the interband continuum limits the frequency at which plasmons can propagate and introduces a considerable damping. This is not present in the local approximation, which breaks down at frequencies close to E_F .

Plasmon losses are traditionally introduced using the Mermin relaxation time approximation (RTA), which is practical due to its simplicity. Its limitation, however, is that it introduces a phenomenological relaxation time without any microscopic mechanism. The results we display in this thesis are obtained using the RTA, but the methods we have developed, i.e., Green's functions with self energies can be used to also investigate microscopic scattering mechanisms. This was studied in Papers III and IV where adatoms and random scattering sites are investigated in terms of their effect on the graphene plasmons. The conclusion from these papers is that the microscopic details of the scattering that occurs matters for the losses induced in the plasmons. Further studies are needed, both theoretical and experimental, in order to find the best model for damping of graphene plasmons. This may well turn out to be different for different graphene samples due to differences in production method, environment etc.

In the appended publications we have also investigated nonlocal effects on graphene plasmons and their signature in light scattering experiments. Nonlocal effects can be important to consider when the plasmon wavelength is comparable with the Fermi wavelength. We also studied plasmon losses and their effects on the light scattering signals and applied this for sensing purposes. In addition, we studied the possibility of controlling graphene plasmons using DC currents in the graphene sheet.

Appendices

Appendix A

Graphene Hamiltonian and Electron Bands

In this appendix we derive the momentum space Hamiltonian in Eq. (2.8) starting from the real space tight-binding Hamiltonian in Eq. (2.6).

For convenience, we reprint the real-space tight-binding Hamiltonian in Eq. (2.6), which is the starting point of the calculation. The Hamiltonian reads

$$H = -t \sum_{\langle i,j \rangle, s} \left(a_{i,s}^\dagger b_{j,s} + h.c. \right) \quad (\text{A.1})$$

and $\langle .. \rangle$ denotes nearest-neighbor summation, $s = (\uparrow, \downarrow)$ is a sum over spins, and $t = 2.8$ eV is the nearest-neighbor hopping amplitude. We also reprint Eqs. (2.3)-(2.5), the nearest-neighbor vectors that connect an atom in the graphene lattice with its nearest neighbors:

$$\vec{\delta}_1 = \frac{a}{2} \left(1, \sqrt{3} \right), \quad (\text{A.2})$$

$$\vec{\delta}_2 = \frac{a}{2} \left(1, -\sqrt{3} \right), \quad (\text{A.3})$$

$$\vec{\delta}_3 = a \left(-1, 0 \right). \quad (\text{A.4})$$

We now insert a Fourier transform of the real-space operators, i.e., $a_{i,s} = \frac{1}{\sqrt{N}} \sum_{\vec{k}} e^{-i\vec{k} \cdot \vec{R}_i} a_s(\vec{k})$ (and similarly for $b_{i,s}$) into Eq. (A.1) and obtain

$$H = -\frac{t}{N} \sum_{\langle i,j \rangle, s} \sum_{\vec{k}} \sum_{\vec{k}'} \left(e^{i(\vec{k} \cdot \vec{R}_i - \vec{k}' \cdot \vec{R}_j)} a_s^\dagger(\vec{k}) b_s(\vec{k}') + h.c. \right). \quad (\text{A.5})$$

Considering the lattice site i , for site j to be a nearest neighbor they necessarily obey the relationship $\vec{R}_j = \vec{R}_i + \vec{\delta}_m$ where $m = (1, 2, 3)$, so we

can replace the nearest-neighbor sum with a sum over all unit cells, i , and all three nearest neighbors m . Making these replacement to the sums in the Hamiltonian, we get

$$H = -\frac{t}{N} \sum_{i,m,s} \sum_{\vec{k}} \sum_{\vec{k}'} \left(e^{i\vec{R}_i \cdot (\vec{k} - \vec{k}')} e^{-i\vec{\delta}_m \cdot \vec{k}'} a_s^\dagger(k) b_s(k') + H.c. \right). \quad (\text{A.6})$$

Now, we use the fact that the sum on i becomes $N\delta_{k,k'}$ and then use this Kronecker delta to remove the sum on k' to obtain

$$H = -t \sum_{\vec{k},s} \left[\left(e^{-i\vec{\delta}_1 \cdot \vec{k}} + e^{-i\vec{\delta}_2 \cdot \vec{k}} + e^{-i\vec{\delta}_3 \cdot \vec{k}} \right) a_s^\dagger(k) b_s(k) + h.c. \right], \quad (\text{A.7})$$

where we have written out the sum on m explicitly. This can be written in matrix form as

$$H = (a_s^\dagger(k), b_s^\dagger(k)) \begin{pmatrix} 0 & -t\phi_k \\ -t\phi_k^* & 0 \end{pmatrix} \begin{pmatrix} a_s(k) \\ b_s(k) \end{pmatrix}, \quad (\text{A.8})$$

where we have defined

$$\phi_k = \left(e^{-i\vec{\delta}_1 \cdot \vec{k}} + e^{-i\vec{\delta}_2 \cdot \vec{k}} + e^{-i\vec{\delta}_3 \cdot \vec{k}} \right). \quad (\text{A.9})$$

Eq. (A.8) is exactly Eq. (2.8).

Appendix B

Graphene Green's Function

In this appendix we calculate the Green's function for graphene, i.e, Eq. (3.9) in the main text.

The definition of the Green's function can be written [70]

$$G(\varepsilon) = (\varepsilon \mathbf{1} - H)^{-1}, \quad (\text{B.1})$$

where $\mathbf{1}$ denotes a unit matrix of suitable size. By having knowledge of the eigenvalues and eigenvectors of the Hamiltonian, one may construct the Green's function satisfying Eq. (B.1) by writing the Green's function [70]:

$$G(\varepsilon) = \sum_{\lambda} \frac{|\psi_{\lambda}\rangle\langle\psi_{\lambda}|}{\varepsilon - E_{\lambda}} \quad (\text{B.2})$$

where $|\psi_{\lambda}\rangle$ are the eigenvectors, E_{λ} are the eigenvalues and the sum on λ runs over all eigenvalues.

We retype now the one-valley graphene Hamiltonian from Eq. (2.13) for practical purposes;

$$\hat{H}_{\vec{K}}(\vec{k}) = v_F \begin{pmatrix} 0 & k_x - ik_y \\ k_x + ik_y & 0 \end{pmatrix}. \quad (\text{B.3})$$

By performing a simple rewrite of this Hamiltonian we get

$$\hat{H}_{\vec{K}}(\vec{k}) = v_F \begin{pmatrix} 0 & ke^{-i\phi_k} \\ ke^{i\phi_k} & 0 \end{pmatrix}, \quad (\text{B.4})$$

where $k = \sqrt{k_x^2 + k_y^2}$ and $\phi_k = \arg(k_x + ik_y)$. The eigenvalues and eigenvectors of the one-valley Hamiltonian are

$$E_{\lambda} = \lambda v_F k \quad (\text{B.5})$$

$$|\psi_{\lambda}\rangle = \frac{1}{\sqrt{2}} \begin{pmatrix} \lambda e^{i\phi_k} \\ 1 \end{pmatrix}, \quad (\text{B.6})$$

where $\lambda = \pm$ denotes the valence band ($-$) and conduction band ($+$) respectively. Inserting the eigenvalues and eigenvectors in Eq. (B.2) we obtain

$$G(\vec{k}, \varepsilon) = \frac{1}{2} \sum_{\lambda=\pm} \frac{1}{\varepsilon - \lambda v_F k} \begin{pmatrix} 1 & \lambda e^{-i\phi_k} \\ \lambda e^{i\phi_k} & 1 \end{pmatrix} \quad (\text{B.7})$$

which is exactly the Green's function in Eq. (3.9) of the main text.

Appendix C

S-matrix Method Calculation

Here, we perform the most technical parts of the S-matrix calculation as well as write down the S-matrices for the grating region and the graphene sheet. The notation is introduced in section 4.3.1.

To write the waves in the grating region as propagating waves, we first find the eigenmodes that give us the propagating modes and decaying modes inside this region. After some matrix algebra involving Maxwell's equations, we arrive at the eigenproblem for the field inside the grating region:

$$\partial_z^2 \vec{E}_l = P^{l,m} \vec{E}_m, \quad (\text{C.1})$$

where the vector arrow denotes a vector of field amplitudes and

$$P^{l,m} = T_1^{l,n} T_2^{n,m}, \quad (\text{C.2})$$

$$T_1^{l,n} = i\omega\delta_{n,l} - \frac{i}{\omega}\varepsilon_{n-l}^{-1}k_n k_l, \quad (\text{C.3})$$

$$T_2^{l,n} = i\omega\varepsilon_{n-l}. \quad (\text{C.4})$$

The solution to (C.1) can be recast in terms of the eigenmodes \tilde{E}_m as

$$\partial_z^2 \tilde{E}_l = \underbrace{S_a^{-1} P S_a}_D \tilde{E}_m, \quad (\text{C.5})$$

where S_a is a matrix with the eigenvectors of $P^{l,m}$ as its columns and D is a matrix with the eigenvalues of $P^{l,m}$ on its diagonal. The relationship between the actual electric field and the eigenmodes is $\vec{E}_l = S_a \tilde{E}_m$ and the total eigenmode is written as

$$\tilde{E}_m(z) = \tilde{E}_m^+ e^{i\gamma_m z} + \tilde{E}_m^- e^{-i\gamma_m z} \quad (\text{C.6})$$

where we have defined γ_m as the diagonal elements of the matrix γ which satisfies

$$\gamma^2 = -D. \quad (\text{C.7})$$

By defining yet another matrix $T_a = iT_1^{-1}S_a\gamma$, we can write down the actual electric and magnetic fields inside the grating region as

$$\begin{pmatrix} \vec{E}_m(z) \\ \vec{H}_m(z) \end{pmatrix} = \begin{pmatrix} S_a & S_a \\ T_a & -T_a \end{pmatrix} \begin{pmatrix} \tilde{E}_m^+(z) \\ \tilde{E}_m^-(z) \end{pmatrix}, \quad (\text{C.8})$$

where $\vec{E}_m(z)$ and $\vec{H}_m(z)$ are vectors containing the field amplitudes for the total fields in the grating region.

We are now in a position to match the field amplitudes across the boundaries between the regions in Fig. 4.3. The graphene conductivity enters as a discontinuity of the parallel component of the magnetic field, see Eq. (4.30), and note that $j_s = \sigma E_x$. First, we consider the wave matching from region 1 to region 2, i.e., across the grating region, giving us a scattering matrix

$$\begin{aligned} S_{\text{grating}} &= \quad (\text{C.9}) \\ &= \begin{pmatrix} Qe^{i\gamma h}(p - mp^{-1}m) & Q(e^{i\gamma h}mp^{-1}e^{i\gamma h}p - m) \\ Q(e^{i\gamma h}mp^{-1}e^{i\gamma h}p - m) & Qe^{i\gamma h}(p - mp^{-1}m) \end{pmatrix}, \end{aligned}$$

with

$$Q = (p - e^{i\gamma h}mp^{-1}e^{i\gamma h}m)^{-1}, \quad (\text{C.10})$$

$$p = S_a^{-1} + T_a^{-1}T_0, \quad (\text{C.11})$$

$$m = S_a^{-1} - T_a^{-1}T_0. \quad (\text{C.12})$$

The h -dependence comes from the propagation of fields inside the grating region and the rather complicated matrix expressions arise from the non-trivial matching of wave amplitudes into and out of the grating region. Second, we consider the S-matrix across the graphene sheet, which gives us

$$S_{\text{graphene}} = \begin{pmatrix} 2M & -M T_0^{-1}\sigma \\ -M T_0^{-1}\sigma & 2M \end{pmatrix}, \quad (\text{C.13})$$

$$M = (2S_0 + T_0^{-1}\sigma)^{-1}. \quad (\text{C.14})$$

where σ is a diagonal matrix with $\sigma(k_j, \omega)$ on the diagonal. For more detail on how to find the expressions in Eqs. (C.9) and (C.13), we refer to appendix B of Paper I.

Appendix D

Rayleigh-Ritz Variational Method for the Poisson Equation

In this appendix, we discuss the Rayleigh-Ritz variational method for the Poisson equation given by Eq. (4.48). In this method, we must first construct a functional whose minimum corresponds to the differential equation in question, in our case Eq. (4.48). The functional for our problem is given by [108]

$$F(\tilde{V}) = \int_0^L dx \left[\left(\frac{1}{2} \frac{d\tilde{V}}{dx} \right)^2 - \rho \tilde{V} \right], \quad (\text{D.1})$$

which can be verified by performing a variation δV on the functional around the solution V . Such a variation needs to be zero for an arbitrary variation that goes to zero at the end points. In a first step, a variation of Eq. (D.1) leads to

$$\int_0^L dx \left(\frac{dV}{dx} \frac{d\delta V}{dx} - \rho \delta V \right) = 0, \quad (\text{D.2})$$

and integrating the first term by parts we obtain

$$\frac{dV}{dx} \delta V \Big|_{x=0}^{x=L} - \int_0^L dx \delta V \left(\frac{d^2 V}{dx^2} + \rho \right) = 0. \quad (\text{D.3})$$

The first term is zero since the variation δV is zero at the boundary and since the equality should hold for small and arbitrary variations, we conclude that the expression in the parenthesis must be zero. Comparing the expression in the parenthesis with Eq. (4.48), we see that they are identical and we thus conclude that V must satisfy this differential equation.

We can now use the functional in Eq. (D.1) to determine the unknown coefficients in the solution ansatz, Eq. (4.51). We substitute the ansatz

into Eq. (D.1) and obtain

$$F = \sum_{i=1}^3 \left[\frac{1}{2} \int_{x_i}^{x_{i+1}} dx \left(\frac{V_{i+1} - V_i}{x_{i+1} - x_i} \right)^2 \right. \quad (\text{D.4})$$

$$\left. - \int_{x_i}^{x_{i+1}} dx \left(V_i \frac{x_{i+1} - x}{x_{i+1} - x_i} + V_{i+1} \frac{x - x_i}{x_{i+1} - x_i} \right) \right]. \quad (\text{D.5})$$

Evaluating the integrals, performing the sum, and simplifying we obtain

$$F = 3 \left(V_2^2 + V_3^2 + \frac{1}{2} - V_2 V_3 - V_3 \right) - \frac{1}{3} \left(V_2 + V_3 + \frac{1}{2} \right). \quad (\text{D.6})$$

To minimize the functional, we now take the derivatives with respect to V_2 and V_3 and equate the expressions to zero. This gives the equations:

$$\frac{\partial F}{\partial V_2} = 6V_2 - 3V_3 - \frac{1}{3} = 0, \quad (\text{D.7})$$

$$\frac{\partial F}{\partial V_3} = -3V_2 + 6V_3 - \frac{10}{3} = 0, \quad (\text{D.8})$$

and solving these gives us the remaining coefficients.

The approximate FEM solution is now determined by the basis function, Eq. (4.51), together with the coefficients

$$V_1 = 0, \quad V_2 = \frac{4}{9}, \quad V_3 = \frac{7}{9}, \quad V_4 = 1. \quad (\text{D.9})$$

Fig. 4.5 shows this solution together with the exact solution and they can be seen to be in good agreement.

Appendix E

Longitudinal (TM) Plasmon Dispersion Equation for Conducting Sheets

In this appendix we derive the longitudinal (TM) plasmon dispersion equation around conducting sheets, i.e., Eq. (5.1) in the main text. The sheet can in general be any sheet that is thin enough (thin compared with the plasmon wavelength).

E.1 Longitudinal plasmon dispersion equation

We start by considering a conducting sheet in the $z = 0$ plane, i.e., the sheet spans the x and y direction and the z direction is perpendicular to the conducting sheet. We will refer to the half-plane $z > 0$ as I and the half-plane $z < 0$ as II , they are assumed to have dielectric constants ϵ_1 and ϵ_2 , respectively.

We are interested in electromagnetic field configurations that are confined around the sheet, i.e., the fields should have a $e^{iqx - \beta|z| - i\omega t}$ behaviour, where $\beta = \sqrt{q^2 - \omega^2\epsilon_{1,2}}$. We now need to make use of the boundary conditions for electromagnetic fields at a conducting boundary. The ones needed for our purposes are [78]

$$D_z^I - D_z^{II} = \rho \tag{E.1}$$

$$E_x^I - E_x^{II} = 0 \tag{E.2}$$

$$H_y^{II} - H_y^I = j = \sigma(q, \omega)E_x^{I/II}, \tag{E.3}$$

where ρ is the sheet charge density, j is the sheet current, and the superscripts I and II denote the fields just above and below the conducting

sheet. In the last equality in (E.3), we have used Ohm's law to express the current in terms of the electric field and the conductivity. The boundary conditions (E.1)-(E.3) tells us that the discontinuity in the perpendicular component of the displacement field is set by the charge density, the in-plane component of the electric field is continuous, and the in-plane component of the magnetic field has a discontinuity which is set by the current density.

Two of Maxwells equations from chapter 4 with no currents or charges (the current and charge mentioned previously exist only at the graphene interface) are

$$\nabla \times \vec{E} = i\omega \vec{H} \quad (\text{E.4})$$

$$\nabla \times \vec{H} = -i\omega \vec{E} \varepsilon_{1,2}. \quad (\text{E.5})$$

Writing these equations in their components for the field configuration for TM plasmons (E_x, E_z, H_y) we obtain

$$\partial_z E_x - \partial_x E_z = i\omega H_y \quad (\text{E.6})$$

$$\partial_x H_y = -\omega E_z \varepsilon_{1,2} \quad (\text{E.7})$$

$$\partial_z H_y = i\omega E_x \varepsilon_{1,2}. \quad (\text{E.8})$$

Using (E.7) we can express E_z as

$$E_z = \frac{-q H_y}{\omega \varepsilon_{1,2}}. \quad (\text{E.9})$$

Inserting this in (E.6), we get

$$\partial_z E_x = i \left(\omega - \frac{q^2}{\omega \varepsilon_{1,2}} \right) H_y. \quad (\text{E.10})$$

Remembering the $e^{-\beta|z|}$ -behavior of the confined modes we have to be careful evaluating the z -derivative, and we get

$$-\text{sign}(z)\beta E_x^{I/II} = \frac{i}{\omega \varepsilon_{1,2}} (\varepsilon_{1,2}\omega^2 - q^2) H_y^{I/II}, \quad (\text{E.11})$$

where $z > 0$ for region I and $z < 0$ for region II . From this we write H_y as

$$H_y^{I/II} = \text{sign}(z) \frac{i\sqrt{\varepsilon_{1,2}}}{\sqrt{\frac{q^2}{\omega^2 \varepsilon_{1,2}} - 1}} E_x^{I/II}, \quad (\text{E.12})$$

where we have used that $\beta = \sqrt{q^2 - \omega^2 \varepsilon_{1,2}}$. We now insert this expression

in the boundary condition, (E.3), and rearrange the terms to obtain

$$E_0 \left(\frac{\sqrt{\varepsilon_1}}{\sqrt{\frac{q^2}{\omega^2 \varepsilon_1} - 1}} + \frac{\sqrt{\varepsilon_2}}{\sqrt{\frac{q^2}{\omega^2 \varepsilon_2} - 1}} + i\sigma(q, \omega) \right) = 0, \quad (\text{E.13})$$

where we have relabeled $E_x^I = E_x^{II} = E_0$. To fulfill this equality, either the electric field E_0 is zero, or the terms within the parentheses is vanishing. By taking the terms inside the parentheses and setting them to zero, we obtain

$$\frac{\sqrt{\varepsilon_1}}{\sqrt{\frac{q^2}{\omega^2 \varepsilon_1} - 1}} + \frac{\sqrt{\varepsilon_2}}{\sqrt{\frac{q^2}{\omega^2 \varepsilon_2} - 1}} + i\sigma(q, \omega) = 0 \quad (\text{E.14})$$

which is the longitudinal (TM) plasmon dispersion equation for thin conducting sheets. By using the sheet conductivity for graphene for $\sigma(q, \omega)$, we obtain the plasmon dispersion equation for graphene. We call the mode transverse magnetic (TM) since the magnetic field ($\hat{y}H_y$) is transverse to the direction of propagation ($\hat{x}q$).

E.2 Non-retarded limit and expansion in small plasmon losses

The plasmon dispersion equation in Eq. (E.14) is in many cases unnecessarily cumbersome to work with, (partly) due to the presence of the square-root factors in the expression. Since graphene plasmons often fulfill the condition $q \gg \omega/c$, it is possible to expand the square roots and keep only the lowest order term. Using a Taylor expansion of the form

$$\frac{1}{\sqrt{x^2 - 1}} = \frac{1}{x} + \frac{1}{2x^3} + \dots \quad (\text{E.15})$$

and keeping only the first term, Eq. (E.14) can be written

$$1 + \frac{iq \sigma(q, \omega)}{\omega(\varepsilon_1 + \varepsilon_2)} = 0, \quad (\text{E.16})$$

which has a simpler form than the original equation and is often used in practice. Eq. (E.16) is often referred to as the non-retarded dispersion equation and one should remember that it is only valid in the regime $q \gg \omega/c$. However, this is usually the case for graphene plasmons and the limitation is in practice only important when considering the limiting behavior for $q \rightarrow 0$.

One thing to notice with Eq. (E.16) is that it is a complex equation, which for complex $\sigma(q, \omega)$ needs a complex wave vector to solve. The

complex wave vector, $q = q_1 + iq_2$, is introduced and the wavelength of the mode is given by $\lambda = \frac{2\pi}{q_1}$ and the plasmon losses are given by q_2 . Now, for small plasmon losses, $\frac{q_2}{q_1} \ll 1$, we can expand Eq. (E.16) to lowest order in q_2 and we get two equations

$$1 = \frac{q_1 \sigma_2(q_1, \omega)}{\omega(\varepsilon_1 + \varepsilon_2)} \quad (\text{E.17})$$

$$\frac{q_2}{q_1} = \frac{\sigma_1(q_1, \omega)}{\frac{\partial}{\partial q_1}(q_1 \sigma_2(q_1, \omega))}, \quad (\text{E.18})$$

where $\sigma(q_1, \omega) = \sigma(q_1, \omega) + i\sigma_2(q_1, \omega)$. Inspecting Eqs. (E.17) and (E.18), we observe that the first one is the same equation as Eq. (E.16) under the assumption of no losses and it does not contain q_2 . Solving this equation then lets us evaluate q_2 using the second equation; this provides information about the plasmon losses. Note that this allows us to also make a consistency check on the validity of the assumption of small losses, or $q_2/q_1 \ll 1$.

Having knowledge of both q_1 and q_2 , (wavelength and losses), it is possible to determine the propagation length of the plasmons. One ambiguity that arises is that since the mode is exponentially decaying, we need to make a decision about what when to say that the plasmon ‘‘has decayed’’ and is no longer propagating. Following Ref. [4], we take the definition that the plasmon has decayed when the intensity of the oscillation has dropped by a factor $e^{-1} \approx 0.37$. This gives us that the propagation length L_p in units of the plasmon wavelength λ_p is [4]

$$\frac{L_p}{\lambda_p} = \frac{q_1}{4\pi q_2}. \quad (\text{E.19})$$

Bibliography

- [1] S. Maier, *Plasmonics: Fundamentals and Applications*. New York: Springer, 2007.
- [2] X.-B. Wu, F. Wang, X. Fan, W. Yi, W. Zuo, F. Bian, L. Jiang, I. D. McGreer, R. Wang, J. Yang, Q. Yang, D. Thompson, and Y. Beletsky, “An ultraluminous quasar with a twelve-billion-solar-mass black hole at redshift 6.30,” *Nature*, vol. 518, pp. 512–515, 2015.
- [3] E. G. van Putten, D. Akbulut, J. Bertolotti, W. L. Vos, A. Lagendijk, and A. P. Mosk, “Scattering Lens Resolves Sub-100 nm Structures with Visible Light,” *Physical Review Letters*, vol. 106, p. 193905, 2011.
- [4] P. A. D. Goncalves and N. M. R. Peres, *An Introduction to Graphene Plasmonics*. Singapore: World Scientific, 2016.
- [5] R. Zia, J. A. Schuller, A. Chandran, and M. L. Brongersma, “Plasmonics: the next chip-scale technology,” *Materials Today*, vol. 9, pp. 20–27, 2006.
- [6] J. C. Maxwell, “A Dynamical Theory of the Electromagnetic Field,” *Philosophical Transactions of the Royal Society of London*, vol. 155, pp. 459–512, 1865.
- [7] R. W. Wood, “On a Remarkable Case of Uneven Distribution of Light in a Diffraction Grating Spectrum,” *Proceedings of the Physical Society of London*, vol. 18, pp. 269–275, 1902.
- [8] L. Tonks and I. Langmuir, “Oscillations in Ionized Gases,” *Physical Review*, vol. 33, pp. 195–210, 1929.
- [9] D. Pines, “Collective Energy Losses in Solids,” *Reviews of Modern Physics*, vol. 28, pp. 184–198, 1956.
- [10] R. Ritchie, E. Arakawa, J. Cowan, and R. Hamm, “Surface-Plasmon Resonance Effect in Grating Diffraction,” *Physical Review Letters*, vol. 21, pp. 1530–1533, 1968.

- [11] S. A. Maier and H. A. Atwater, “Plasmonics: Localization and guiding of electromagnetic energy in metal/dielectric structures,” *Journal of Applied Physics*, vol. 98, p. 011101, 2005.
- [12] M. I. Stockman, “Nanoplasmonics: The physics behind the applications,” *Physics Today*, vol. 64, pp. 39–44, 2011.
- [13] F. H. L. Koppens, D. E. Chang, and F. J. García de Abajo, “Graphene Plasmonics: A Platform for Strong Light-Matter Interactions,” *Nano Letters*, vol. 11, pp. 3370–3377, 2011.
- [14] R. Chikkaraddy, B. de Nijs, F. Benz, S. J. Barrow, O. A. Scherman, E. Rosta, A. Demetriadou, P. Fox, O. Hess, and J. J. Baumberg, “Single-molecule strong coupling at room temperature in plasmonic nanocavities,” *Nature*, vol. 535, pp. 127–130, 2016.
- [15] W. L. Barnes, A. Dereux, and T. W. Ebbesen, “Surface plasmon subwavelength optics,” *Nature*, vol. 424, pp. 824–830, 2003.
- [16] C. L. Wong and M. Olivo, “Surface Plasmon Resonance Imaging Sensors: A Review,” *Plasmonics*, vol. 9, pp. 809–824, 2014.
- [17] H. Nguyen, J. Park, S. Kang, and M. Kim, “Surface Plasmon Resonance: A Versatile Technique for Biosensor Applications,” *Sensors*, vol. 15, pp. 10481–10510, 2015.
- [18] D. K. Gramotnev and S. I. Bozhevolnyi, “Plasmonics beyond the diffraction limit,” *Nature Photonics*, vol. 4, pp. 83–91, 2010.
- [19] W. L. Barnes, “Surface plasmon-polariton length scales: a route to sub-wavelength optics,” *Journal of Optics A: Pure and Applied Optics*, vol. 8, pp. S87–S93, 2006.
- [20] E. H. Hwang and S. Das Sarma, “Dielectric function, screening, and plasmons in two-dimensional graphene,” *Physical Review B*, vol. 75, p. 205418, 2007.
- [21] B. Wunsch, T. Stauber, F. Sols, and F. Guinea, “Dynamical polarization of graphene at finite doping,” *New Journal of Physics*, vol. 8, pp. 318–318, 2006.
- [22] F. Stern, “Polarizability of a Two-Dimensional Electron Gas,” *Physical Review Letters*, vol. 18, pp. 546–548, 1967.
- [23] K. S. Novoselov, A. K. Geim, S. V. Morozov, D. Jiang, Y. Zhang, S. V. Dubonos, I. V. Grigorieva, and A. A. Firsov, “Electric Field Effect in Atomically Thin Carbon Films,” *Science*, vol. 306, pp. 666–669, 2004.

- [24] Z. Fei, A. S. Rodin, G. O. Andreev, W. Bao, A. S. McLeod, M. Wagner, L. M. Zhang, Z. Zhao, M. Thiemens, G. Dominguez, M. M. Fogler, A. H. C. Neto, C. N. Lau, F. Keilmann, and D. N. Basov, “Gate-tuning of graphene plasmons revealed by infrared nano-imaging,” *Nature*, vol. 487, pp. 82–5, 2012.
- [25] J. Chen, M. Badioli, P. Alonso-González, S. Thongrattanasiri, F. Huth, J. Osmond, M. Spasenović, A. Centeno, A. Pesquera, P. Godignon, A. Zurutuza Elorza, N. Camara, F. J. G. de Abajo, R. Hillenbrand, and F. H. L. Koppens, “Optical nano-imaging of gate-tunable graphene plasmons,” *Nature*, vol. 487, pp. 77–81, 2012.
- [26] M. Jablan, H. Buljan, and M. Soljačić, “Plasmonics in graphene at infrared frequencies,” *Physical Review B*, vol. 80, p. 245435, 2009.
- [27] M. R. Ramezanali, M. M. Vazifeh, R. Asgari, M. Polini, and A. H. MacDonald, “Finite-temperature screening and the specific heat of doped graphene sheets,” *Journal of Physics A: Mathematical and Theoretical*, vol. 42, p. 214015, 2009.
- [28] S. Das Sarma and Q. Li, “Intrinsic plasmons in two-dimensional Dirac materials,” *Physical Review B*, vol. 87, p. 235418, 2013.
- [29] N. Ashcroft and N. Mermin, *Solid State Physics*. Belmont: Brooks/Cole, 1976.
- [30] F. J. García de Abajo, “Nonlocal Effects in the Plasmons of Strongly Interacting Nanoparticles, Dimers, and Waveguides,” *The Journal of Physical Chemistry C*, vol. 112, pp. 17983–17987, 2008.
- [31] G. Toscano, S. Raza, S. Xiao, M. Wubs, A.-P. Jauho, S. I. Bozhevolnyi, and N. A. Mortensen, “Surface-enhanced Raman spectroscopy: nonlocal limitations,” *Optics Letters*, vol. 37, p. 2538, 2012.
- [32] R. Ruppin, “Effect of non-locality on nanofocusing of surface plasmon field intensity in a conical tip,” *Physics Letters A*, vol. 340, pp. 299–302, 2005.
- [33] R. Jurga, S. D’Agostino, F. Della Sala, and C. Ciraci, “Plasmonic Nonlocal Response Effects on Dipole Decay Dynamics in the Weak and Strong-Coupling Regimes,” *The Journal of Physical Chemistry C*, 2017.
- [34] T. Low and P. Avouris, “Graphene Plasmonics for Terahertz to Mid-Infrared Applications,” *ACS Nano*, vol. 8, pp. 1086–1101, 2014.

- [35] A. N. Grigorenko, M. Polini, and K. S. Novoselov, “Graphene plasmonics,” *Nature Photonics*, vol. 6, pp. 749–758, 2012.
- [36] F. H. L. Koppens, T. Mueller, P. Avouris, A. C. Ferrari, M. S. Vitiello, and M. Polini, “Photodetectors based on graphene, other two-dimensional materials and hybrid systems,” *Nature Nanotechnology*, vol. 9, pp. 780–793, 2014.
- [37] T. Echtermeyer, S. Milana, U. Sassi, A. Eiden, M. Wu, E. Lidorikis, and A. Ferrari, “Surface Plasmon Polariton Graphene Photodetectors,” *Nano Letters*, vol. 16, pp. 8–20, 2016.
- [38] D. Rodrigo, O. Limaj, D. Janner, D. Etezadi, F. J. García de Abajo, V. Pruneri, and H. Altug, “Mid-infrared plasmonic biosensing with graphene,” *Science*, vol. 349, pp. 165–168, 2015.
- [39] D. B. Farmer, P. Avouris, Y. Li, T. F. Heinz, and S.-J. Han, “Ultrasensitive Plasmonic Detection of Molecules with Graphene,” *ACS Photonics*, vol. 3, pp. 553–557, 2016.
- [40] S. Kim, M. S. Jang, V. W. Brar, Y. Tolstova, K. W. Mauser, and H. A. Atwater, “Electronically tunable extraordinary optical transmission in graphene plasmonic ribbons coupled to subwavelength metallic slit arrays,” *Nature Communications*, vol. 7, p. 12323, 2016.
- [41] G. E. P. Box and N. R. Draper, *Empirical model-building and response surfaces*. New York: John Wiley & Sons, 1987.
- [42] D. C. Elias, R. V. Gorbachev, A. S. Mayorov, S. V. Morozov, A. A. Zhukov, P. Blake, L. A. Ponomarenko, I. V. Grigorieva, K. S. Novoselov, F. Guinea, and A. K. Geim, “Dirac cones reshaped by interaction effects in suspended graphene,” *Nature Physics*, vol. 7, pp. 701–704, 2011.
- [43] A. H. Castro Neto, F. Guinea, N. M. R. Peres, K. S. Novoselov, and A. K. Geim, “The electronic properties of graphene,” *Reviews of Modern Physics*, vol. 81, pp. 109–162, 2009.
- [44] P. R. Wallace, “The Band Theory of Graphite,” *Physical Review*, vol. 71, pp. 622–634, 1947.
- [45] M. I. Katsnelson, *Graphene: Carbon in two dimensions*. Cambridge: Cambridge University Press, 2012.
- [46] S. Das Sarma, S. Adam, E. H. Hwang, and E. Rossi, “Electronic transport in two-dimensional graphene,” *Reviews of Modern Physics*, vol. 83, pp. 407–470, 2011.

- [47] H. Liu, Y. Liu, and D. Zhu, “Chemical doping of graphene,” *J. Mater. Chem.*, vol. 21, pp. 3335–3345, 2011.
- [48] K. J. Tielrooij, J. C. W. Song, S. A. Jensen, A. Centeno, A. Pesquera, A. Zurutuza Elorza, M. Bonn, L. S. Levitov, and F. H. L. Koppens, “Photoexcitation cascade and multiple hot-carrier generation in graphene,” *Nature Physics*, vol. 9, pp. 248–252, 2013.
- [49] V. Gantmakher and Y. Levinson, *Carrier scattering in metals and semiconductors*. Amsterdam: North Holland, 1987.
- [50] B. V. Duppen, A. Tomadin, A. N. Grigorenko, and M. Polini, “Current-induced birefringent absorption and non-reciprocal plasmons in graphene,” *2D Materials*, vol. 3, p. 015011, 2016.
- [51] F. Bonaccorso, A. Lombardo, T. Hasan, Z. Sun, L. Colombo, and A. C. Ferrari, “Production and processing of graphene and 2d crystals,” *Materials Today*, vol. 15, pp. 564–589, 2012.
- [52] A. Altland and B. Simons, *Condensed Matter Field Theory*. Cambridge: Cambridge University Press, 2nd ed., 2010.
- [53] L. Wang, I. Meric, P. Y. Huang, Q. Gao, Y. Gao, H. Tran, T. Taniguchi, K. Watanabe, L. M. Campos, D. A. Muller, J. Guo, P. Kim, J. Hone, K. L. Shepard, and C. R. Dean, “One-dimensional electrical contact to a two-dimensional material,” *Science*, vol. 342, pp. 614–7, 2013.
- [54] S. Bae, H. Kim, Y. Lee, X. Xu, J.-S. Park, Y. Zheng, J. Balakrishnan, T. Lei, H. Ri Kim, Y. I. Song, Y.-J. Kim, K. S. Kim, B. Özyilmaz, J.-H. Ahn, B. H. Hong, and S. Iijima, “Roll-to-roll production of 30-inch graphene films for transparent electrodes,” *Nature Nanotechnology*, vol. 5, pp. 574–578, 2010.
- [55] L. Banszerus, M. Schmitz, S. Engels, M. Goldsche, K. Watanabe, T. Taniguchi, B. Beschoten, and C. Stampfer, “Ballistic Transport Exceeding 28 μm in CVD Grown Graphene,” *Nano Letters*, vol. 16, pp. 1387–1391, 2016.
- [56] F. Torrisi, T. Hasan, W. Wu, Z. Sun, A. Lombardo, T. S. Kulmala, G.-W. Hsieh, S. Jung, F. Bonaccorso, P. J. Paul, D. Chu, and A. C. Ferrari, “Inkjet-Printed Graphene Electronics,” *ACS Nano*, vol. 6, pp. 2992–3006, 2012.
- [57] H. Yan, T. Low, W. Zhu, Y. Wu, M. Freitag, X. Li, F. Guinea, P. Avouris, and F. Xia, “Damping pathways of mid-infrared plasmons

- in graphene nanostructures,” *Nature Photonics*, vol. 7, pp. 394–399, 2013.
- [58] E. H. Hwang, S. Adam, and S. Das Sarma, “Carrier Transport in Two-Dimensional Graphene Layers,” *Physical Review Letters*, vol. 98, p. 186806, 2007.
- [59] T. Ando, “Screening Effect and Impurity Scattering in Monolayer Graphene,” *Journal of the Physical Society of Japan*, vol. 75, p. 074716, 2006.
- [60] T. Stauber, N. M. R. Peres, and F. Guinea, “Electronic transport in graphene: A semiclassical approach including midgap states,” *Physical Review B*, vol. 76, p. 205423, 2007.
- [61] A. Bergvall, J. M. Carlsson, and T. Löfwander, “Influence of [0001] tilt grain boundaries on the destruction of the quantum Hall effect in graphene,” *Physical Review B*, vol. 91, p. 245425, 2015.
- [62] T. Löfwander and M. Fogelström, “Impurity scattering and Mott’s formula in graphene,” *Physical Review B*, vol. 76, p. 193401, 2007.
- [63] K. I. Bolotin, K. J. Sikes, Z. Jiang, M. Klima, G. Fudenberg, J. Hone, P. Kim, and H. L. Stormer, “Ultrahigh electron mobility in suspended graphene,” *Solid State Communications*, vol. 146, pp. 351–355, 2008.
- [64] H. Yoon, C. Forsythe, L. Wang, N. Tombros, K. Watanabe, T. Taniguchi, J. Hone, P. Kim, and D. Ham, “Measurement of collective dynamical mass of Dirac fermions in graphene,” *Nature Nanotechnology*, vol. 9, pp. 594–599, 2014.
- [65] C. R. Dean, A. F. Young, I. Meric, C. Lee, L. Wang, S. Sorgenfrei, K. Watanabe, T. Taniguchi, P. Kim, K. L. Shepard, and J. Hone, “Boron nitride substrates for high-quality graphene electronics,” *Nature Nanotechnology*, vol. 5, pp. 722–726, 2010.
- [66] A. Woessner, M. B. Lundberg, Y. Gao, A. Principi, P. Alonso-González, M. Carrega, K. Watanabe, T. Taniguchi, G. Vignale, M. Polini, J. Hone, R. Hillenbrand, and F. H. L. Koppens, “Highly confined low-loss plasmons in graphene-boron nitride heterostructures,” *Nature Materials*, vol. 14, pp. 421–425, 2014.
- [67] E. H. Hwang and S. Das Sarma, “Acoustic phonon scattering limited carrier mobility in two-dimensional extrinsic graphene,” *Physical Review B*, vol. 77, p. 115449, 2008.

- [68] M. Sabbaghi, H.-W. Lee, T. Stauber, and K. S. Kim, “Drift-induced modifications to the dynamical polarization of graphene,” *Physical Review B*, vol. 92, p. 195429, 2015.
- [69] P. Tassin, T. Koschny, and C. M. Soukoulis, “Graphene for Terahertz Applications,” *Science*, vol. 341, pp. 620–621, 2013.
- [70] J. Cuevas and E. Scheer, *Molecular Electronics: An Introduction to Theory and Experiments*. Singapore: World Scientific Publishing, 2010.
- [71] L. Kadanoff and G. Baym, *Quantum statistical mechanics*. New York: W.A. Benjamin, Inc., 1962.
- [72] L. Keldysh, “Diagram technique for nonequilibrium processes,” *Sov. Phys. JETP*, vol. 47, pp. 1515–1527, 1964.
- [73] J. Rammer, *Quantum field theory of non-equilibrium states*. Cambridge: Cambridge university press, 2007.
- [74] H. Haug and A. Jauho, *Quantum Kinetics in Transport and Optics of Semiconductors*. Berlin: Springer Verlag, 2nd ed., 2008.
- [75] G. Mahan, *Many-Particle Physics*. New York: Plenum Press, 2nd ed., 1993.
- [76] A. Fetter and J. Walecka, *Quantum theory of many-particle systems*. New York: Dover publications, Inc., 7th (dover) ed., 2003.
- [77] G. F. Giuliani and G. Vignale, *Quantum theory of the electron liquid*. Cambridge: Cambridge University Press, 2005.
- [78] J. Jackson, *Classical Electrodynamics*. New York: John Wiley & Sons, Inc., 3rd ed., 1999.
- [79] M. Dressel and G. Grüner, *Electrodynamics of solids*. Cambridge: Cambridge University Press, 2002.
- [80] A. Principi, M. Polini, and G. Vignale, “Linear response of doped graphene sheets to vector potentials,” *Physical Review B*, vol. 80, p. 075418, 2009.
- [81] J. Sabio, J. Nilsson, and A. H. Castro Neto, “f -sum rule and unconventional spectral weight transfer in graphene,” *Physical Review B*, vol. 78, p. 075410, 2008.
- [82] L. A. Falkovsky and S. S. Pershoguba, “Optical far-infrared properties of a graphene monolayer and multilayer,” *Phys. Rev. B*, vol. 76, p. 153410, 2007.

- [83] L. A. Falkovsky, “Optical properties of graphene,” *Journal of Physics: Conference Series*, vol. 129, p. 012004, 2008.
- [84] Z. Q. Li, E. A. Henriksen, Z. Jiang, Z. Hao, M. C. Martin, P. Kim, H. L. Stormer, and D. N. Basov, “Dirac charge dynamics in graphene by infrared spectroscopy,” *Nature Physics*, vol. 4, pp. 532–535, 2008.
- [85] N. D. Mermin, “Lindhard Dielectric Function in the Relaxation-Time Approximation,” *Physical Review B*, vol. 1, pp. 2362–2363, 1970.
- [86] F. J. García de Abajo, “Graphene Plasmonics: Challenges and Opportunities,” *ACS Photonics*, vol. 1, pp. 135–152, 2014.
- [87] A. F. Page, F. Ballout, O. Hess, and J. M. Hamm, “Nonequilibrium plasmons with gain in graphene,” *Physical Review B*, vol. 91, p. 075404, 2015.
- [88] G. S. Atwal and N. W. Ashcroft, “Relaxation of an electron system: conserving approximation,” *Physical Review B*, vol. 65, p. 115109, 2002.
- [89] E. Economou, *Green’s functions in quantum physics*. Berlin: Springer Verlag, 3rd ed., 2006.
- [90] P. Drude, “Zur Elektronentheorie der Metalle,” *Annalen der Physik*, vol. 306, pp. 566–613, 1900.
- [91] C. Kittel, *Introduction to solid state physics*. New York: John Wiley & Sons, Inc., 8th ed., 2005.
- [92] J. Tiggesbäumker, L. Köller, K.-H. Meiwes-Broer, and A. Liebsch, “Blue shift of the Mie plasma frequency in Ag clusters and particles,” *Physical Review A*, vol. 48, pp. R1749–R1752, 1993.
- [93] K.-P. Charlé, L. König, S. Nepijko, I. Rabin, and W. Schulze, “The Surface Plasmon Resonance of Free and Embedded Ag-Clusters in the Size Range $1,5 \text{ nm} < D < 30 \text{ nm}$,” *Crystal Research and Technology*, vol. 33, pp. 1085–1096, 1998.
- [94] C. Ciraci, R. T. Hill, J. J. Mock, Y. Urzhumov, A. I. Fernández-Domínguez, S. A. Maier, J. B. Pendry, A. Chilkoti, and D. R. Smith, “Probing the Ultimate Limits of Plasmonic Enhancement,” *Science*, vol. 337, pp. 1072–1074, 2012.
- [95] S. Søren Raza, N. Stenger, S. Kadkhodazadeh, R. V. Fischer, N. Kostesha, A.-P. Jauho, A. Burrows, M. Wubs, and N. A. Mortensen, “Blueshift of the surface plasmon resonance in silver

- nanoparticles studied with EELS,” *Nanophotonics*, vol. 2, pp. 131–138, 2013.
- [96] P. Apell and D. R. Penn, “Optical Properties of Small Metal Spheres: Surface Effects,” *Physical Review Letters*, vol. 50, pp. 1316–1319, 1983.
- [97] U. Kreibig and L. Genzel, “Optical absorption of small metallic particles,” *Surface Science*, vol. 156, pp. 678–700, 1985.
- [98] R. Fuchs and F. Claro, “Multipolar response of small metallic spheres: Nonlocal theory,” *Physical Review B*, vol. 35, pp. 3722–3727, 1987.
- [99] C. David and F. J. García de Abajo, “Spatial Nonlocality in the Optical Response of Metal Nanoparticles,” *The Journal of Physical Chemistry C*, vol. 115, pp. 19470–19475, 2011.
- [100] N. Mortensen, S. Raza, M. Wubs, T. Søndergaard, and S. Bozhevolnyi, “A generalized non-local optical response theory for plasmonic nanostructures,” *Nature Comm.*, vol. 5, no. 3809, 2014.
- [101] K. J. Savage, M. M. Hawkeye, R. Esteban, A. G. Borisov, J. Aizpurua, and J. J. Baumberg, “Revealing the quantum regime in tunnelling plasmonics,” *Nature*, vol. 491, pp. 574–577, 2012.
- [102] M. B. Lundberg, Y. Gao, R. Asgari, C. Tan, B. Van Duppen, M. Aurore, P. Alonso-González, A. Woessner, K. Watanabe, T. Taniguchi, R. Hillenbrand, J. Hone, M. Polini, and F. H. L. Koppens, “Tuning quantum nonlocal effects in graphene plasmonics,” *Science*, vol. 357, pp. 187–191, 2017.
- [103] T. Stauber, N. M. R. Peres, and A. K. Geim, “Optical conductivity of graphene in the visible region of the spectrum,” *Physical Review B*, vol. 78, p. 085432, 2008.
- [104] R. R. Nair, P. Blake, A. N. Grigorenko, K. S. Novoselov, T. J. Booth, T. Stauber, N. M. R. Peres, and A. K. Geim, “Fine Structure Constant Defines Visual Transparency of Graphene,” *Science*, vol. 320, p. 1308, 2008.
- [105] Z.-Y. Li and L.-L. Lin, “Photonic band structures solved by a plane-wave-based transfer-matrix method,” *Physical Review E*, vol. 67, p. 046607, 2003.
- [106] R. Courant, “Variational methods for the solution of problems of equilibrium and vibrations,” *Bulletin of the American Mathematical Society*, vol. 49, pp. 1–24, 1943.

- [107] “www.comsol.com/.”
- [108] J. Jin, *The Finite Element Method in Electromagnetics*. New York: John Wiley & sons, Inc, 2014.
- [109] S. A. Mikhailov and K. Ziegler, “New Electromagnetic Mode in Graphene,” *Physical Review Letters*, vol. 99, p. 016803, 2007.
- [110] L. Holthuijsen, *Waves in oceanic and coastal waters*. Cambridge: Cambridge University Press, 2007.
- [111] A. Otto, “Excitation of nonradiative surface plasma waves in silver by the method of frustrated total reflection,” *Zeitschrift für Physik A Hadrons and nuclei*, vol. 216, pp. 398–410, 1968.
- [112] E. Kretschmann and H. Raether, “Radiative Decay of Non Radiative Surface Plasmons Excited by Light,” *Z. Naturforsch*, vol. 23, pp. 2135–2136, 1968.
- [113] B. Hecht, H. Bielefeldt, L. Novotny, Y. Inouye, and D. W. Pohl, “Local Excitation, Scattering, and Interference of Surface Plasmons,” *Physical Review Letters*, vol. 77, pp. 1889–1892, 1996.
- [114] R. H. Ritchie, “Plasma Losses by Fast Electrons in Thin Films,” *Physical Review*, vol. 106, pp. 874–881, 1957.
- [115] C. J. Powell and J. B. Swan, “Origin of the Characteristic Electron Energy Losses in Aluminum,” *Physical Review*, vol. 115, pp. 869–875, 1959.
- [116] L. Ju, B. Geng, J. Horng, C. Girit, M. Martin, Z. Hao, H. A. Bechtel, X. Liang, A. Zettl, Y. R. Shen, and F. Wang, “Graphene plasmonics for tunable terahertz metamaterials.,” *Nature nanotechnology*, vol. 6, pp. 630–4, 2011.
- [117] Z. Fei, G. O. Andreev, W. Bao, L. M. Zhang, A. S. McLeod, C. Wang, M. K. Stewart, Z. Zhao, G. Dominguez, M. Thiemens, M. M. Fogler, M. J. Tauber, A. H. Castro-Neto, C. N. Lau, F. Keilmann, and D. N. Basov, “Infrared Nanoscopy of Dirac Plasmons at the Graphene-SiO₂ Interface,” *Nano Letters*, vol. 11, pp. 4701–4705, 2011.
- [118] B. Jiang, G. X. Ni, C. Pan, Z. Fei, B. Cheng, C. N. Lau, M. Bockrath, D. N. Basov, and M. M. Fogler, “Tunable Plasmonic Reflection by Bound 1D Electron States in a 2D Dirac Metal,” *Physical Review Letters*, vol. 117, p. 086801, 2016.

- [119] Z. Fei, M. D. Goldflam, J.-S. Wu, S. Dai, M. Wagner, A. S. McLeod, M. K. Liu, K. W. Post, S. Zhu, G. C. A. M. Janssen, M. M. Fogler, and D. N. Basov, “Edge and Surface Plasmons in Graphene Nanoribbons,” *Nano Letters*, vol. 15, pp. 8271–8276, 2015.
- [120] A. Y. Nikitin, P. Alonso-González, S. Vélez, S. Mastel, A. Centeno, A. Pesquera, A. Zurutuza, F. Casanova, L. E. Hueso, F. H. L. Koppens, and R. Hillenbrand, “Real-space mapping of tailored sheet and edge plasmons in graphene nanoresonators,” *Nature Photonics*, vol. 10, pp. 239–243, 2016.
- [121] M. Lundeborg, Y. Gao, A. Woessner, C. Tan, P. Alonso-González, K. Watanabe, T. Taniguchi, J. Hone, R. Hillenbrand, and F. H. L. Koppens, “Thermoelectric detection and imaging of propagating graphene plasmons,” *Nature Materials*, vol. 16, pp. 204–207, 2016.
- [122] P. Alonso-González, A. Y. Nikitin, F. Golmar, A. Centeno, A. Pesquera, S. Vélez, J. Chen, G. Navickaite, F. Koppens, A. Zurutuza, F. Casanova, L. E. Hueso, and R. Hillenbrand, “Controlling graphene plasmons with resonant metal antennas and spatial conductivity patterns,” *Science*, vol. 344, pp. 1369–1373, 2014.
- [123] K. Tantiwanichapan, X. Wang, H. Durmaz, Y. Li, A. K. Swan, and R. Paiella, “Graphene Terahertz Plasmons: A Combined Transmission Spectroscopy and Raman Microscopy Study,” *ACS Photonics*, vol. 4, pp. 2011–2017, 2017.
- [124] X. Zhu, W. Yan, P. Uhd Jepsen, O. Hansen, N. Asger Mortensen, and S. Xiao, “Experimental observation of plasmons in a graphene monolayer resting on a two-dimensional subwavelength silicon grating,” *Applied Physics Letters*, vol. 102, p. 131101, 2013.
- [125] W. Gao, G. Shi, Z. Jin, J. Shu, Q. Zhang, R. Vajtai, P. M. Ajayan, J. Kono, and Q. Xu, “Excitation and Active Control of Propagating Surface Plasmon Polaritons in Graphene,” *Nano Letters*, vol. 13, pp. 3698–3702, 2013.
- [126] D. Rodrigo, A. Tittl, O. Limaj, F. J. G. de Abajo, V. Pruneri, and H. Altug, “Double-layer graphene for enhanced tunable infrared plasmonics,” *Light: Science & Applications*, vol. 6, p. e16277, 2017.
- [127] L. J. Sherry, S.-H. Chang, G. C. Schatz, R. P. Van Duyne, B. J. Wiley, and Y. Xia, “Localized Surface Plasmon Resonance Spectroscopy of Single Silver Nanocubes,” *Nano Letters*, pp. 2034–2038, 2005.

-
- [128] J. Li, J. Ye, C. Chen, L. Hermans, N. Verellen, J. Ryken, H. Jans, W. Van Roy, V. V. Moshchalkov, L. Lagae, and P. Van Dorpe, “Biosensing Using Diffractively Coupled Plasmonic Crystals: the Figure of Merit Revisited,” *Advanced Optical Materials*, vol. 3, pp. 176–181, 2015.
- [129] J. Li, J. Ye, C. Chen, Y. Li, N. Verellen, V. V. Moshchalkov, L. Lagae, and P. Van Dorpe, “Revisiting the Surface Sensitivity of Nanoplasmonic Biosensors,” *ACS Photonics*, vol. 2, pp. 425–431, 2015.
- [130] P. B. Johnson and R. W. Christy, “Optical Constants of the Noble Metals,” *Physical Review B*, vol. 6, pp. 4370–4379, 1972.
- [131] “<https://refractiveindex.info/>.”
- [132] G. Mie, “Beiträge zur Optik trüber Medien, speziell kolloidaler Metallösungen,” *Annalen der Physik*, vol. 330, pp. 377–445, 1908.
- [133] P. J. Schuck, D. P. Fromm, A. Sundaramurthy, G. S. Kino, and W. E. Moerner, “Improving the Mismatch between Light and Nanoscale Objects with Gold Bowtie Nanoantennas,” *Physical Review Letters*, vol. 94, p. 017402, 2005.